Designing Polymer Hydrogels for Extrusion-Based Additive Manufacturing

Ryan Thomas Shafranek

A dissertation

submitted in partial fulfillment of the

requirements for the degree of

Doctor of Philosophy

University of Washington

2021

Reading Committee:

Alshakim Nelson, Chair

Gojko Lalic

František Tureček

Program Authorized to Offer Degree:

Chemistry

University of Washington

Abstract

Designing Polymer Hydrogels for Extrusion-Based Additive Manufacturing

Ryan Thomas Shafranek

Chair of the Supervisory Committee:
Alshakim Nelson
Department of Chemistry

Additive manufacturing (AM) technologies are expanding the boundaries of materials science and providing an exciting forum for interdisciplinary research. The ability to fabricate arbitrarily complex objects has made AM technologies indispensable in personalized healthcare, soft electronics, and renewable energy. At the intersection of AM technologies and materials chemistry are stimuli-responsive polymers, which change their chemical and physical properties in response to specific environmental cues. Stimuli-responsive polymer hydrogels, in particular, are seeing significant interest in extrusion-based AM for the fabrication of bespoke medical implants and tissue engineering. The responsiveness of these “smart” hydrogels makes them suitable for AM and provides functionality to the additively manufactured objects. The type of stimulus response, mechanical properties, and functionality of these hydrogels can be regulated

through chemical transformations or incorporation of additives. This dissertation describes two fundamentally different approaches to formulating polymer hydrogels for extrusion-based AM. Chapter 1 provides a thorough introduction to AM and stimuli-responsive hydrogels, with emphasis on hydrogels that respond to changes in temperature and shear pressure. Chapter 2 and Chapter 3 describe chemical transformations to the end groups of synthetic block copolymers to afford changes in hydrogel temperature response, mechanical characteristics, and morphology. By contrast, Chapter 4 reports the collaborative development of a 3D-printable bioink based on cardiac decellularized extracellular matrix (cdECM). While Chapter 2 and Chapter 3 deal with molecular-level changes to wholly synthetic polymer systems, Chapter 4 deals with biopolymers derived from porcine cardiac cells that are combined with synthetic additives. The two approaches offer contrasting strategies for the design of polymer hydrogels for AM.

TABLE OF CONTENTS

LIST OF FIGURES

LIST OF TABLES

ACKNOWLEDGEMENTS

This thesis would not exist without the following important people. Most of this work was done by my hand, but in the end, it does not belong to me. First, I thank Al Nelson. Al always finds the time to support his students and collaborators, and it is clear that he prioritizes people over all else. I am perpetually amazed by his calm approach to running a research lab. His Zen-like attitude is something I aspire to.

Second, I thank my fellow lab members, especially Amrita Basu, Trevor Johnston, and Dylan Karis: the first-year crew. As friends and fellow scientists, you are without equal. Chris Fellin, Patrick Smith, Claudia Willis, and Jenn Wong – thank you for always being willing to share a laugh or honest advice.

Third, I thank current and past professors at the University of Washington, who both inspired and challenged me throughout the years. Special thanks to Dr. Andrew J. Boydston, Dr. Gojko Lalic, and Dr. Champak Chatterjee for keeping my interest during those first-year graduate classes.

Fourth, I thank my parents, Rick and Donna, for their unwavering and unconditional support. You laid the foundation for who I am today. I'm glad you had a good visit to Seattle!

Finally, I thank my partner, Holly Jacobs – without you, I would have lost my mind years ago. I love you, and I thank you for being the only person to know exactly what this thesis is about without ever reading it.

DEDICATION

This work is dedicated to my grandfather, Walter J. McGregor, and also to all victims of the COVID-19 pandemic.

"Where is the hand on the harpstring, and the red fire glowing?

Where is the spring and the harvest and the tall corn growing?

They have passed like rain on the mountain, like a wind in the meadow;

The days have gone down in the West behind the hills into shadow."

- J.R.R. Tolkien

Chapter 1. DEVELOPING NOVEL SOFT MATERIALS FOR EXTRUSION-BASED ADDITIVE MANUFACTURING

1.1 Introduction to Extrusion-Based Additive Manufacturing

Additive manufacturing (AM), or 3D printing (3DP), is a form of digital production that can transfer objects created by computer-aided design (CAD) from the virtual world into the physical world. While many different types of AM tools exist, most of these processes use layer-by-layer deposition of a material to fabricate 3D objects. For example, in fused deposition modeling (FDM), also called fused filament fabrication, filamentized material is extruded through a heated nozzle and then deposited onto a cooler build stage, while in vat photo-polymerization AM processes like stereolithography (SLA), a thin layer of liquid photo-resin is cured in a pattern-wise manner using light. All AM technologies are capable of producing arbitrarily complex shapes, although some techniques result in higher object resolution or faster production times. While the type of printer, printing parameters, and modeling software are important to enabling AM, materials specifically designed for AM have yet to reach maturity. The material properties are vital characteristics necessary for the evolution of AM as an industrial standard for manufacturing. Recently, "smart" materials that respond and change according to specific external stimuli have seen significant interest. Researchers have since responded to this demand, developing an array of synthetic and naturally-occurring materials with a multitude of stimuli responses. Stimuli-responsive polymers, also referred to as smart polymers, change their physical or chemical properties in response to specific triggers such as heat,[1,2] light,[2,3] electrical and magnetic fields,[4,5] pH,[1,6] redox potential,[7,8] and mechanical force.[9–12] The responsiveness of smart polymers can be

an inherent property, or it can be due to the presence of additives, as in composite materials. Due to their ability to convert small environmental changes into measurable responses, smart polymers have been used for controlled drug delivery,[13–16] tissue engineering,[14–22] soft robotics,[23–25] electronics,[24–28] and mechanically reinforced materials.[29] The advantage of using smart polymers in AM is the ability to produce complex, functional materials that respond to their environments in programmed ways, without the need for external intervention. The object geometries afforded by AM, combined with the stimuli-responsive character provided by smart polymers, makes the range of potential applications limitless.

The choice of AM type depends on both the intended application and the nature of the material used as the ink. As such, no type of AM is inherently superior to another. For example, vat photo-polymerization AM is excellent for producing high-resolution constructs and offers unprecedented control over spatial patterning. However, photo-polymerizations are irreversible, and so vat photo-polymerization AM has limited potential to produce 3D constructs that degrade over time. On the other hand, extrusion-based AM cannot yet replicate the resolution and precision of vat photo-polymerization but allows the use of materials that can degrade or be removed after printing.

FDM and direct-ink writing (DIW) are two of the most common extrusion-based AM processes (Figure 1.1). Both processes involve the extrusion of a material through a nozzle onto a build platform, although the material requirements for each kind of AM are different. For example, FDM requires materials that soften when heated during extrusion, then rapidly solidify upon cooling. Thermoplastic polymers, which are not covalently cross-linked, are ideal for FDM. For DIW, polymer inks should be either highly viscous or shear-thinning (wherein physical cross-links

between polymer chains are disrupted by shear force). These viscoelastic polymer inks flow under high-strain conditions but cease flowing or recover mechanical integrity after extrusion.

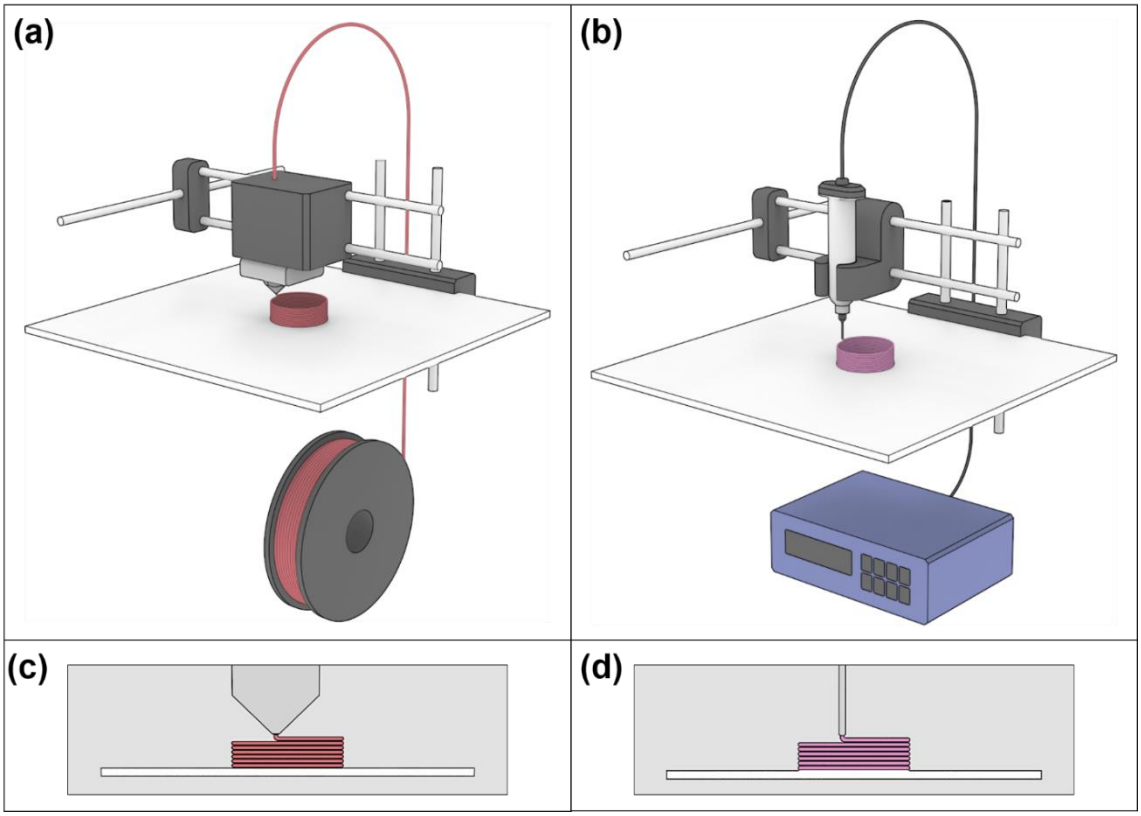

Figure 1.1. Cartoon representations of (a) fused deposition modeling (FDM) and (b) direct-ink writing (DIW)
In FDM, spooled thermoplastic filament is mechanically extruded through a heated nozzle onto a build stage. In DIW, viscoelastic material is pneumatically or mechanically extruded from a nozzle or syringe needle onto a build stage. (c,d) Side views of individual filaments stacking on the build stage as they flow from the nozzle.

During FDM, a continuous filament of thermoplastic material is mechanically fed into a nozzle and simultaneously heated so that it flows from the nozzle.[30,31] Thermoplastic polymers like acrylonitrile butadiene styrene copolymer (ABS) must be heated well above their characteristic glass transition temperature (T_g), and semi-crystalline polymers like poly(lactic acid)

(PLA) must also be heated above their melting temperature (T_m). Most FDM thermoplastics are shear-thinning in the molten state, reducing the pressure required to extrude molten materials through the nozzle. The filament is often spooled and retained on the printer, and it gradually unwinds as material is used. The molten material is deposited onto a build surface in a consecutive, layer-wise fashion to fabricate a digitally-modeled part. Commonly, the build surface is heated to prevent warping and improve interlayer adhesion; however, not all readily accessible FDM printers have heated build surfaces. Upon deposition, the material cools and holds its structure. In FDM systems, the nozzle is translated at a constant height over the build surface as it deposits material. The nozzle then moves upward a distance proportional to the layer height, and the next layer is fabricated in the same fashion. FDM is relatively user-friendly and commercially accessible. However, the range of materials suitable for FDM is mostly limited to existing thermoplastics. Moreover, FDM is unsuitable for biological applications that employ living cells within the ink. On the other hand, DIW AM processes offer a wider range of existing and novel materials for a broader scope of applications.

In DIW processes, a viscoelastic material is extruded through a nozzle or syringe needle. In most DIW systems, the material is stored in a syringe and is either pneumatically or mechanically expelled from the syringe. Various temperature-control or curing mechanisms are employed to facilitate the deposition and subsequent stabilization of the material. Like FDM, the nozzle is situated above the build surface, and for each layer, it is translated at a constant height over the build surface as it deposits material. The next layer is then fabricated in the same fashion. Many research groups have investigated the rheological properties required for inks in DIW. Broadly, DIW inks must be shear-thinning, meaning the viscosity of the ink decreases with increasing shear stress. This phenomenon ensures that DIW inks are extrudable without resorting

to excessively high pneumatic or mechanical pressure. More specifically, rheological parameters that have been shown to impact printability include yield stress (σ_y),[32–35] tan δ (the ratio of the loss modulus G'' to the storage modulus G'),[36] and viscosity (η).[37,38] Yield stress has been correlated with layer stacking, shape fidelity, and extrusion pressure. Inks that are below a threshold yield stress are unable to produce self-supporting layers and show poor shape fidelity after extrusion. On the other hand, materials with excessively high yield stress require high pressures to extrude, which can be detrimental for delicate applications, such as inks encapsulating live cells. Viscous materials that do not exhibit a yield stress must have a high zero-shear viscosity yet flow under pressure to be printable by DIW. Excessively high zero-shear viscosity will lead to difficulty during extrusion, whereas excessively low zero-shear viscosity results in poor shape fidelity after printing.

There is ample opportunity to develop novel polymer inks for DIW AM. Alternatively, existing materials can be modified to enable or enhance printability, with reference to the aforementioned parameters. Soft materials, such as hydrogels, are inherently suitable for DIW processes. Hydrogels in particular are well-suited to biological AM applications such as bespoke medical implants or *in vitro* tissue engineering. Because such applications often require precise control over material properties, the development and engineering of hydrogel inks for DIW remains a significant challenge. Section 1.2 outlines recent and emerging strategies to address this challenge.

1.2 Designing Stimuli-Responsive Hydrogels For DIW AM

Hydrogels are networks of chemically or physically cross-linked molecules that are swollen with water. These soft materials are composed of synthetic polymers such as poly(2-

hydroxyethyl methacrylate) (PHEMA), poly(*N*-isopropylacrylamide) (PNIPAm), and poloxamers, or biological polymers such as alginate, hyaluronic acid, and collagen. In order to maintain structural integrity, polymer hydrogels must be cross-linked. Cross-links are covalent (like in PNIPAm hydrogels), physical (like electrostatic interactions and van der Waals forces) or both. Stimuli-responsive hydrogels, which respond to temperature, pH, shear stress, and light, have been used for tissue engineering,[39–44] targeted drug delivery,[45–47] and microfluidic devices.[48] Increasingly, researchers are using cell-laden hydrogels in DIW printers to fabricate complex 3D forms for *in vitro* studies of tissue growth and cell behavior. One challenge for DIW printing of hydrogels is their soft nature, which limits stacking of printed filaments in the *z*-direction. The mechanical robustness of hydrogels can be improved *via* curing printed forms to further cross-linking interactions, or by the addition of fillers. The type of stimulus response is important to enabling or enhancing DIW. Polymers with a temperature or shear response are especially suited for DIW, and many polymer hydrogels are multi-stimuli-responsive.

Polymers that exhibit upper or lower critical solution temperature (UCST/LCST) behavior in solution show a soluble-insoluble phase transition at a certain temperature boundary. This temperature boundary varies as a function of the solute-solvent system composition. Put simply, polymers dissolve in a solvent if the Gibbs free energy of mixing is negative, per equation (1.1):

$$\Delta G_{mix} = \Delta H_{mix} - T\Delta S_{mix} \qquad (1.1)$$

where T = temperature and G_{mix}, H_{mix}, and S_{mix} represent the Gibbs energy, enthalpy, and entropy of mixing, respectively. Below the UCST and above the LCST, ΔG_{mix} is positive, and mixing is energetically unfavorable, resulting in phase separation. These phenomena are partially modeled

by Flory-Huggins solution theory, which accounts for the temperature and concentration-dependent solvent-solvent, polymer-solvent, and polymer-polymer interactions.[49,50] Equation (1.2) , based on the Flory-Huggins lattice model, provides a more nuanced approximation of Gibbs free energy of mixing for polymers in solution:

$$\Delta G_{mix} = NRT\left[\frac{\varphi_1}{r_1}\ln(\varphi_1) + \frac{\varphi_2}{r_2}\ln(\varphi_2) + \chi\varphi_1\varphi_2\right] \quad (1.2)$$

Where R is the ideal gas constant, N is the total number of lattice points, φ_1 and φ_2 are the volume fractions of the polymer and solvent, respectively, r_1 and r_2 are the number of segments or lattice points occupied by each polymer or solvent molecule, respectively (r_2 = 1 for solvent molecules), and χ is the Flory-Huggins interaction parameter, which is a function of both temperature and polymer concentration.

For polymers showing LCST behavior in water, the driving force for phase separation is widely accepted to be the "hydrophobic effect." For purely hydrophobic compounds (such as alkanes) in water at room temperature, the enthalpy of solvation is less than or close to zero, but the process is endergonic overall.[51,52] Therefore, entropic effects are invoked to explain hydrophobic aggregation. Hydrophobic molecules disrupt the three-dimensional network of transient, disordered hydrogen bonds between water molecules. This loss of rotational and translational freedom results in a decrease in entropy (*i.e.*, the ΔS term is negative). The aggregation of hydrophobic molecules reduces the extent of this disruption, and beyond a critical cluster size, the free energy of solvation starts to vary with aggregate surface area instead of aggregate volume.[51] For amphiphilic molecules showing LCST behavior, both enthalpic and entropic effects are important. At low temperatures, hydrogen-bonding interactions between water

molecules are stronger, and the entropic contribution to the free energy of solvation becomes less important. Below the LCST, solvation is favorable due to non-covalent solute-solvent interactions like van der Waals forces, and the enthalpic term determines the favorable Gibbs free energy. As temperature rises above the LCST, the increased average molecular energy weakens attractive interactions, molecules gain increased translational and rotational freedom, and entropic effects dominate. Both synthetic and naturally-occurring polymers exhibit UCST or LCST behavior in water. Many of these polymer hydrogels also respond to stimuli such as shear stress, pH, and light. Various synthetic and naturally-derived hydrogels used for DIW, including combinations of both types, are reviewed in the following paragraphs.

PNIPAm is perhaps the most well-studied temperature-responsive synthetic polymer, with an LCST of 32-35 °C. In aqueous solution, the polymer undergoes a coil-to-globule transition above its LCST, expelling water and decreasing in volume in the process.[53] Because this transition occurs just below human body temperature, PNIPAm is a relevant material for tissue engineering and controlled drug delivery.[54] While the temperature response is an inherent property, PNIPAm needs to be covalently cross-linked to form a 3D hydrogel, most often with *N,N'*-methylenebisacrylamide. By itself, PNIPAm does not demonstrate the viscoelastic properties required for extrusion-based printing.[55] As a result, it is often blended with other materials. Spinks and co-workers, for example, used PNIPAm with calcium alginate to make ionic-covalent entanglement (ICE) hydrogels.[56] They created a thermally-actuating valve, combining the temperature response of the PNIPAm with the mechanical reinforcement of the calcium alginate. Another demonstration of PNIPAm's temperature response comes from Lewis, Mahadevan, and colleagues in the form of shape-morphing, biomimetic structures.[57] With Laponite XLG ("nanoclay") acting as a viscosity modifier and cellulose nanofibrils for stiff mechanical

properties, PNIPAm served as a reversible thermal actuator in shape-morphing helices, flowers, and lattices. The cellulose nanofibrils showed shear-induced alignment in the printed direction. As a result, water-induced swelling was greater in the transverse direction (across the width of the fibrils) compared to the longitudinal direction (along the length of the fibrils). This anisotropic swelling was irreversible when poly(*N*,*N*-dimethylacrylamide) (PDMAm) was the polymer used for printing, but the replacement of PDMAm with PNIPAm made the swelling actuation temperature-reversible: above its LCST, the coil-to-globule transition of PNIPAm resulted in a return to a "flat" configuration (Figure 1.2). Following similar principles, PNIPAm served as the responsive component in 3D printed bilayer hinges with one layer composed of PNIPAm and the other layer composed of PHEMA.[58] In this case, a polyether-based polyurethane helped to facilitate extrusion and enhanced the stiffness of the hinges. These 3D printed hydrogel bilayers exhibited anisotropic swelling in water, causing the hinges to bend. Due to the hydrophobic collapse of PNIPAm above its LCST, the swelling and bending behavior was also temperature-dependent.

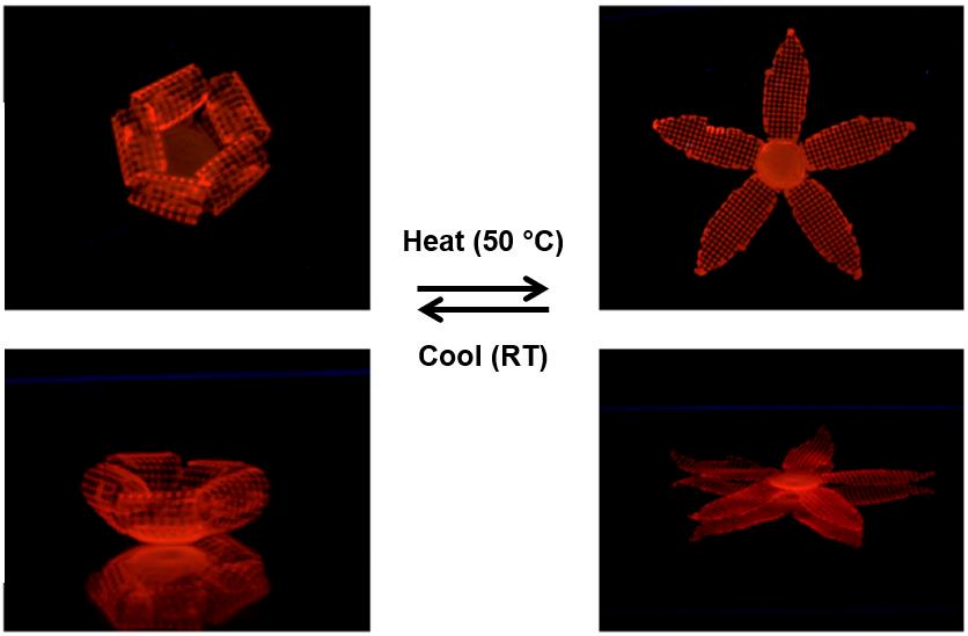

Figure 1.2. Thermoreversible actuation of a printed flower containing PNIPAm
Left: the structure exhibited swelling actuation in room-temperature water. Right: when heated to 50 °C, the structure returned to its flat configuration. The shape change could be cycled several times by changing water temperature. Copyright 2016 (Adapted with permission from Nature Publishing Group).[57]

Changes in temperature not only drive shape-morphing behavior, but also facilitate self-healing and mechanical strengthening of hydrogels. The two latter phenomena are often enabled by combinations of permanent (covalent) and reversible bonds. For example, Connal and others[59] prepared printable hydrogels cross-linked by both oxime linkages and hydrogen-bonds, which were both self-healing and mechanically robust. In this work, poly (*N*-hydroxyethyl acrylamide-*co*-methyl vinyl ketone) (PHEAm-*co*-PMVK) was synthesized *via* free radical polymerization initiated from AiBN, yielding a copolymer of molecular weight M_n = 284 kDa and Đ = 2.39 (determined by SEC). To prepare 3D printable hydrogels, the as-synthesized copolymers were cross-linked with tetraethylene glycol bishydroxylamine (TEG-BHA) in aqueous solution,

resulting in dynamic covalent oxime linkages between polymer chains through the ketone moieties of PMVK (Figure 1.3).

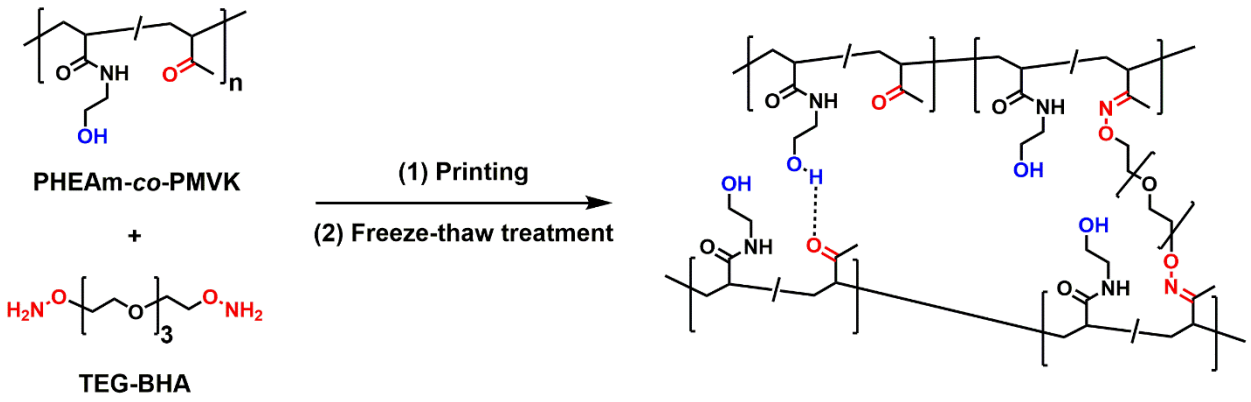

Figure 1.3. Doubly-dynamic cryogels composed of PHEAm-*co*-PMVK
The cryogels were cross-linked by both oxime bonds and hydrogen-bonds.

The low extent of cross-linking and the dynamic nature of the oxime bonds facilitated shear-thinning behavior. After printing, constructs were subjected to multiple freeze-thaw cycles, alternating between -10 or -20 °C and room temperature. This treatment, a type of thermally-induced phase separation (TIPS), resulted in localized pockets of higher polymer concentration surrounded by ice, with strong hydrogen-bonding interactions between the amide and hydroxyl groups of PHEAm (Figure 1.3). The final shear storage modulus (*G'*) and Young's modulus (*E*) of the cryogels was tunable according to the freezing temperature and the total number of freeze-thaw cycles. Importantly, the printed cryogel constructs retained the ability to autonomously self-heal cuts and cracks, due to the presence of both dynamic covalent oxime cross-links as well as hydrogen-bonding interactions.

Many synthetic hydrogels with a temperature response can be engineered to respond to shear pressure, pH, and light as well. For example, poloxamers, known by their BASF trade name

"Pluronics," are triblock copolymers composed of poly(propylene oxide) (PPO) and poly(ethylene oxide) (PEO). These polymers are amphiphilic, nonionic surfactants, with the PPO block exhibiting temperature-dependent solubility in aqueous media.[60–62] Pluronic F127, hereafter referred to simply as "F127," is a poloxamer with M_n = 12,500 g mol^{-1} and block lengths of DP = 98 (PEO) and DP = 67 (PPO).[63–65] Viscoelastic F127 hydrogels (typically 20-40 wt% in water) are shear-thinning and extrudable at room temperature. The gels melt and flow below their gelation temperature, allowing homogeneous incorporation of additives and use as a fugitive ink. Furthermore, F127 is generally biocompatible, although at higher concentrations it can destabilize cell membranes.[66] This combination of mechanical properties and biocompatibility make F127 a popular multi-stimuli-responsive polymer for 3D printed soft materials. Although it is clear that F127 is printable by DIW, the relationship between viscoelastic properties and "printability" has not been fully established. Working towards this end, Nelson and co-workers[33] found that the static and dynamic yield stresses of F127 hydrogels (defined as the pressure required to initiate flow from rest and the pressure required to sustain flow, respectively) correlated strongly to the dimensional fidelity of extruded filaments, and hence printability. In this work, the functionalization of F127 with methacrylate end groups and the inclusion of water-soluble acrylate monomers in the gels resulted in a library of UV-cross-linkable gels with various mechanical properties (Figure 1.4). Groll, Jungst, and co-workers[34] also developed a protocol for correlating the rheological properties of F127 to printability, and also characterized other biocompatible inks such as alginate, alginate-gelatin blends, and a commercial crème from Nivea. In order to be classified as printable, the hydrogels first needed to be shear-thinning, but also required sufficiently high static yield stresses and needed to quickly recover viscosity and modulus following periods of high shear rate. F127 gels displayed all of these prerequisites; however, concentrations of at

least 25 wt% were required to produce continuous, stackable filaments that retained their shape after extrusion. Furthermore, this study helped to determine printable “windows” as functions of extrusion pressure and print speed and tested the effects of ink shear rate on embedded cell viability.

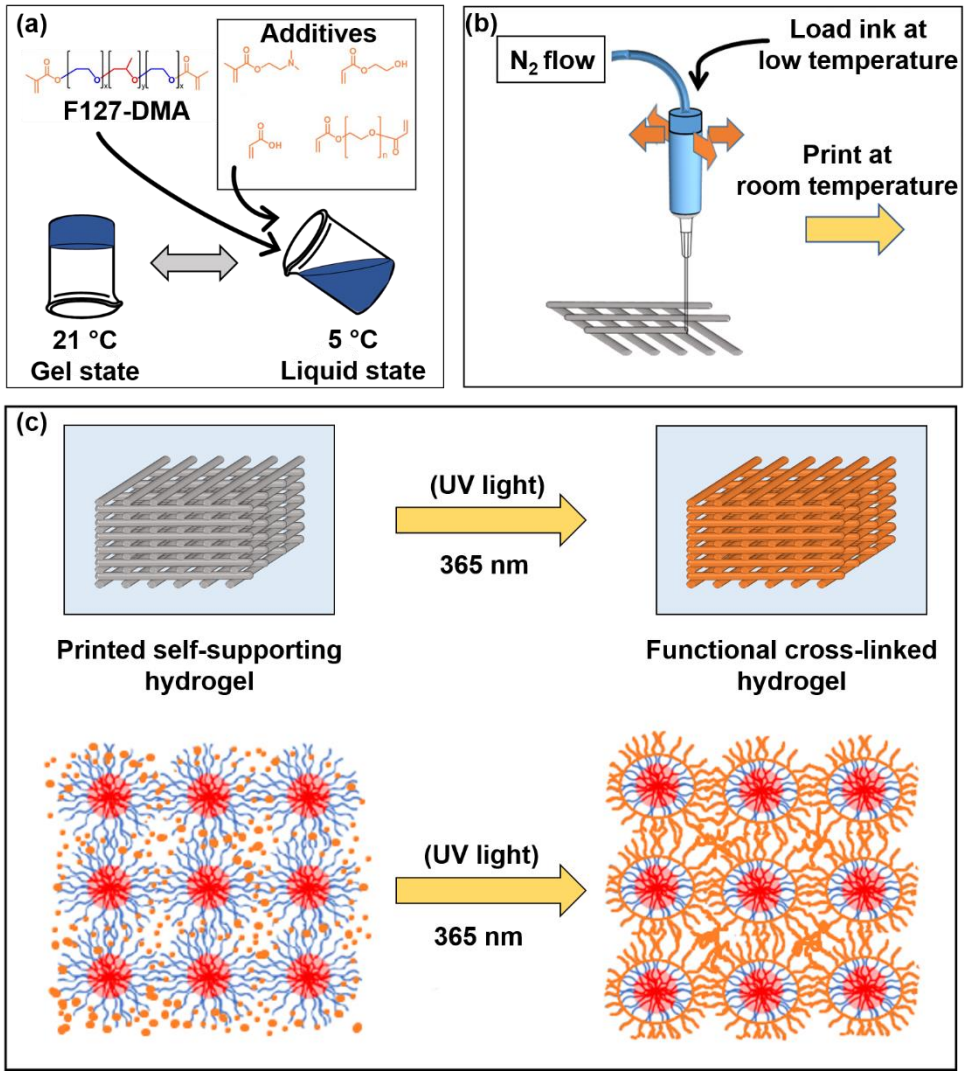

Figure 1.4. Stimuli-responsive F127 hydrogel inks

The incorporation of various water-soluble acrylate monomers (a, inset) produced a library of gels with different viscoelastic properties. (a) Acrylate monomer additives were blended with F127-DMA in the sol state at low temperature, then transferred to a syringe and warmed to room temperature. (b) Gels were pneumatically extruded at room temperature (21 °C). (c) Printed structures were irradiated with 365 nm UV light to induce *in situ* co-polymerization of F127-DMA and acrylate monomers. Copyright 2018 (Adapted with permission from Elsevier).[33]

Because of its extrudability and thermoreversibility, F127 has been frequently used as a fugitive ink. For example, F127 at 35 wt% in water was used as a sacrificial "shell" encapsulating

OrmoClear liquid for the fabrication of optical waveguides by DIW.[67] F127 fugitive inks have also been used by Lewis and co-workers[42,68] to create microvascular networks. Unmodified F127 was printed in a branching pattern into a support bath composed of F127 with diacrylate end-groups (F127-DA).[68] Following extrusion of the fugitive ink into a photo-polymerizable hydrogel resin, the entire structure was UV-irradiated, and the uncured F127 fugitive ink was removed under vacuum at low temperature. This process resulted in a well-defined, branched vascular network. In another, similar system, F127 was printed into a matrix of methacrylated gelatin (gel-MA), then removed under vacuum at low temperatures to yield patterned voids that were subsequently endothelialized with normal human dermal fibroblasts.[42] Following the strategy of printing into a supporting gel bath, Nelson and co-workers[69] utilized F127 in a technique referred to as gel-in-gel (GiG) printing. In this approach, methacrylated F127 (F127-DMA) containing ammonium persulfate (APS) was extruded into a support bath consisting of unmodified F127 and *N,N,N',N'*-tetramethylethylenediamine (TEMED). Upon contact, APS and TEMED initiated a radical polymerization of the F127-DMA, curing the printed structure quickly. Removal of the uncured support gel resulted in robust 3D objects that normally could not be printed with soft materials in air, such as inverted cones. In a creative use of F127 as a fugitive ink, Xe and co-workers[70] used inks consisting of F127 and partially hydrolyzed tetraethyl orthosilicate (TEOS). F127 and hydrolyzed TEOS form a hydrogen-bonded network that manifests as an extrudable hydrogel. The 3D printed structures were cured at high temperatures (200-1000 °C) following extrusion, resulting in removal of the F127 and polymerization of the TEOS to afford shrunken, high-resolution objects. The interaction between F127 and TEOS was shown to prevent structural defects. Furthermore, this strategy was successfully extended to monomers other than TEOS, which

formed hydrogels with F127 and subsequently polymerized after printing to afford well-defined, high resolution structures.

While F127 is benign to most cell types at lower concentrations, it can adversely affect cell viability at high concentrations and over extended periods of time. To circumvent this issue, Zenobi-Wong and co-workers[71] printed blends of F127, F127-DA, and methacrylated hyaluronic acid (HA-MA). The composition of the printable gel was 17 wt% F127, 3 wt% F127-DA, and 0.1 or 0.5 wt% HA-MA. This formulation allowed homogeneous incorporation of bovine chondrocytes at 4 °C, followed by printing at 37 °C. Importantly, the large proportion of uncured F127 was removed after printing and UV curing. This lower concentration of F127, along with the presence of the biologically active HA-MA, resulted in excellent cell viability over 14 days. While mammalian cells are sensitive to F127, robust single-celled organisms such as yeast and bacteria have little difficulty flourishing in F127 gels. Capitalizing on this fact, baker's yeast (*S. cerevisiae*) was embedded in 3D printed cubes consisting of F127-dimethacrylate (F127-DMA) (Figure 1.5).[72] With periodic refreshing of culture media, the yeast cells were able to ferment glucose into ethanol (~90% conversion) with no significant loss of biocatalytic activity for weeks. This coupling of a triple-stimuli-responsive material (temperature, shear pressure, UV light) with active, living cells was termed additive manufacturing of catalytically active living materials (AMCALM).

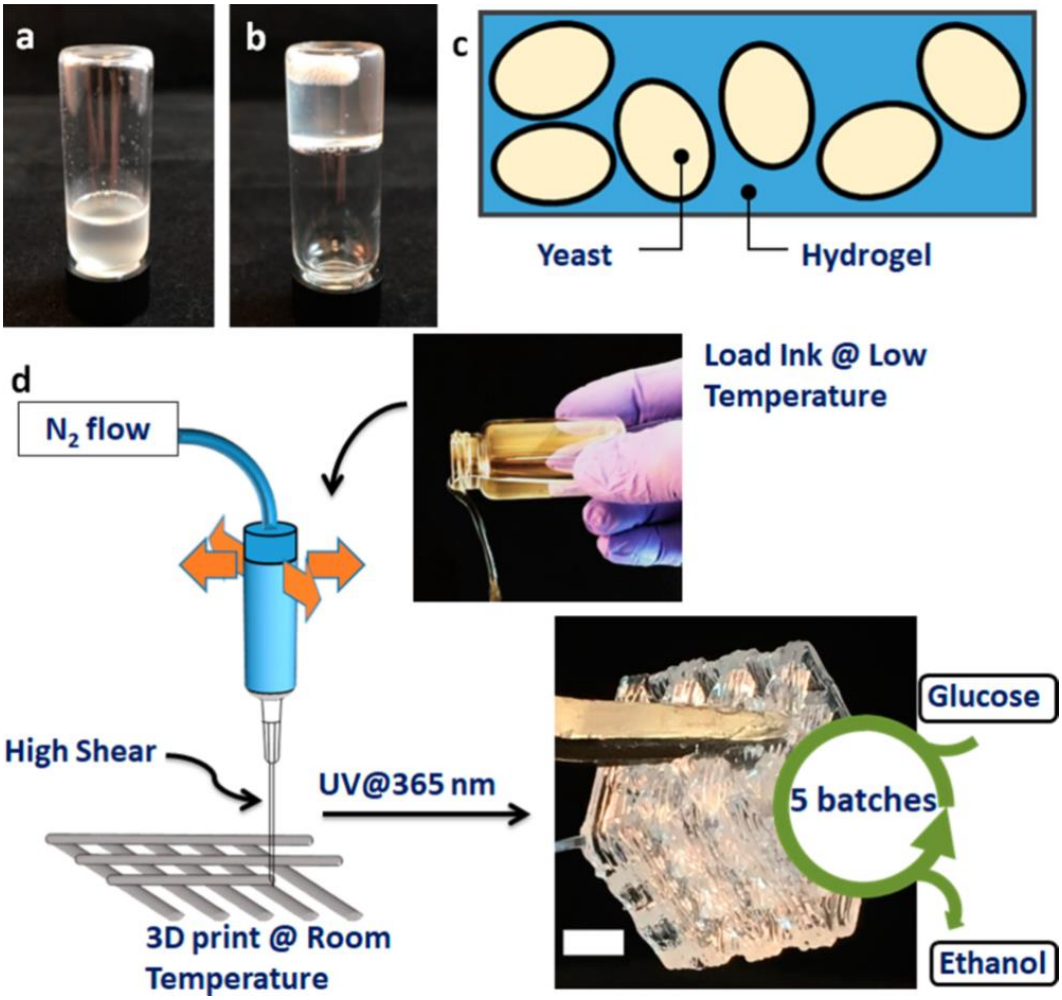

Figure 1.5. Overview of the AMCALM process

F127-DMA 25 wt% hydrogels occupied a sol state (a) at 4 °C and a gel state (b) at 23 °C. (c) Cartoon representation of the yeast cell-laden hydrogel ink. (d) Cell-laden inks were loaded in the sol state, then pneumatically extruded as gels at room temperature and cross-linked with 365 nm light to afford catalytically-active lattice cubes. Copyright 2018 (Reprinted with permission from the American Chemical Society).[72]

Poly(ether)s structurally related to F127, such as poly(alkyl glycidyl ether)s and functionalized poly(glycidol)s, have been explored for their stimuli responses. For example, poly(isopropyl glycidyl ether)-*b*-poly(ethylene oxide)-*b*-poly(isopropyl glycidyl ether) (PiPGE-*b*-PEO-*b*-PiPGE) triblock copolymer solutions underwent a reversible sol-gel transition above a

critical temperature, which was tailorable according to the length of the PiPGE blocks.[73] These gels exhibited the necessary viscoelastic properties for DIW, and outperformed F127 gels in terms of yield stress, mechanical strength of printed objects, and polymer concentration required for gelation. Later, other glycidyl ethers such as poly(allyl glycidyl ether) (PAGE) and poly(ethyl glycidyl ether) (PEGE) were used to create triple-stimuli-responsive hydrogels.[74] The composition of these copolymers was ([PxGE-*stat*-PAGE]-*b*-PEO-*b*-[PxGE-*stat*-PAGE]), where *x* = ethyl or isopropyl. Not only were the gels thermoresponsive and 3D printable, but they were also UV curable through the allyl side groups, in a mechanism that has not yet been characterized. The advantage of these materials lay in the tunability of the sol-gel transition temperature, mechanical properties of the bulk gels, and response to UV light, all of which were synthetically controlled through polymer composition and block length. In a similar use of the allyl functional unit, Lindén, Groll, and co-workers[75,76] synthesized polyglycidol-*stat*-PAGE and then coupled it to thiol-functionalized hyaluronic acid (HA) using the UV-mediated "thiol-ene" reaction. While HA served as the bioactive component of these gels, the polyglycidol polymers were amenable to chemical functionalization through a free primary hydroxyl group. This hydrogel was responsive to shear pressure as a non-cross-linked precursor solution and was responsive to UV light to initiate thiol-ene cross-linking.

Some naturally-occurring biopolymers are inherently responsive to temperature, pH, or shear pressure. Gelatin and collagen are excellent examples. Gelatin is partially hydrolyzed collagen, which itself is a structural protein found in connective tissues, skin, and bone marrow.[77–79] Physically cross-linked gelatin hydrogels dissolve in water around 30-35 °C. Consequently, gelatin must be covalently cross-linked for biological use both *in vitro* and *in vivo* so that the gels do not melt at 37 °C. Importantly, gelatin contains the cell-binding peptide motif arginine-glycine-

aspartic acid (RGD), as well as degradation motifs responsive to matrix metalloproteinases.[80,81] For this reason, gelatin is a popular material for promoting cell growth and attachment in 3D printed soft materials. The temperature-responsive behavior of gel-MA has been utilized by Dubruel and co-workers[82] during DIW printing by using a temperature-controlled jacket around the syringe to heat the ink above the melting temperature of the gel. This process allowed the ink to flow out of the nozzle onto a temperature-controlled build platform to rapidly cool the ink back into a gel. The printed gel-MA construct was then UV-cured to cross-link the protein network.

Many synthetic and biological hydrogels are reversibly cross-linked *via* electrostatic interactions. These gels are responsive to changes in pH or ion concentration, wherein these changes disrupt polymer cross-linking and alter the bulk properties of the gels. Polymers that are pH- and ion-responsive have been used in DIW to produce materials with tunable mechanical strength, controlled drug release capability, and catalytic activity. The electrostatic cross-linking interactions are important for maintaining structural integrity after extrusion printing. Some ionically cross-linked polymers function as the energy-dissipating component of dual-network hydrogels.

Alginate is a polysaccharide produced primarily by brown algae but also in *P. aeruginosa* biofilms, where it plays a key role in conferring antibiotic resistance.[83] Alginate, typically available as the sodium salt, cross-links in the presence of divalent metal cations such as Ca^{2+}. Unless these ions are replenished, they will diffuse away or exchange with monovalent ions over time, making alginate hydrogels good candidates for slow release of drugs and other small molecules. However, the mechanical properties of calcium alginate gels depend strongly on the rate and temperature at which ionic cross-linking occurs.[83] Additionally, calcium alginate gels tend to be brittle, and their suitability for DIW is highly dependent upon calcium ion concentration.[84] Nevertheless, their

biocompatibility and biodegradability make alginate gels common components of composite bioinks. Butcher and co-workers,[85] for example, used poly(ethylene glycol)-diacrylate (PEG-DA) and sodium alginate to 3D print aortic valves. At 10-15 wt%, the alginate enhanced the viscosity of the PEG-DA solutions, making them printable prior to UV curing. In tandem with gelatin, the alginate also served as a temporary, removable filler for the printed valves. Algae-laden blends of alginate and methylcellulose were used to print lattice scaffolds, wherein the algae remained photosynthetically active for at least 12 days.[86] The authors used multichannel plotting to print human osteosarcoma SaOS-2 cells in a co-culture system with the algae, which demonstrated the potential for therapeutic transmission of metabolites from the algae to the human cell line. Feinberg and co-workers[87] 3D printed alginate filaments in a support bath consisting of gelatin microparticles and calcium chloride (Figure 1.6). The key advantage of this technique, termed freeform reversible embedding of soft hydrogels (FRESH), was that soft, non-self-supporting structures, such as helices, could be printed with soft materials like alginate, collagen, and fibrin. Calcium alginate is also commonly the ionic component of ICE networks.[56,88,89] In such networks, the two types of cross-linking mechanisms help to dissipate energy under different types of mechanical load, enhancing the overall strength of the material. [90,91] In another approach, negatively-charged alginate was mixed with 2-hydroxypropyltrimethyl ammonium chloride chitosan (HACC, a positively-charged polysaccharide) to produce a hydrogel that was shear-thinning, self-healing, biocompatible, and adhesive.[92]

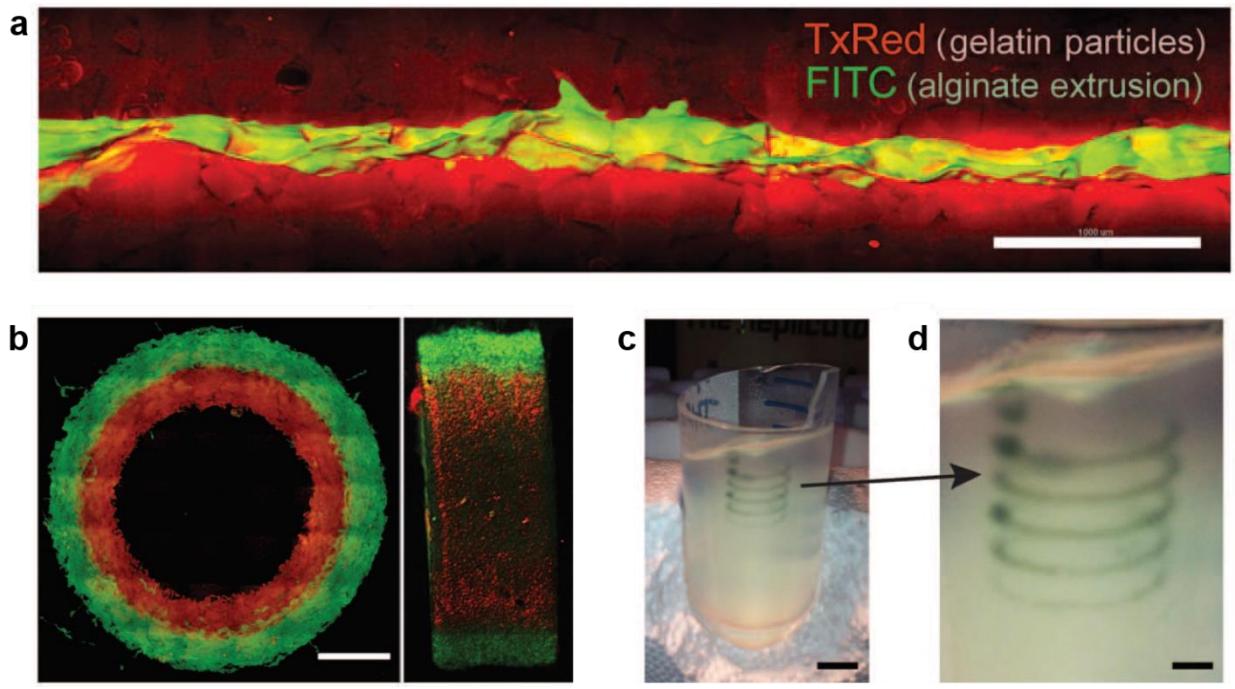

Figure 1.6. Freeform reversible embedding of soft hydrogels (FRESH)
(a) Fluorescently-labeled alginate (green) printed in a gelatin-slurry support bath (red) containing Ca^{2+} ions. Scale bar = 1 mm. (b) Coaxial, multi-material printed cylinder with top view (left) and lateral view (right). Scale bar = 2 mm. (c,d) Nonplanar structures such as helices were fabricated using the FRESH process. Scale bars = 10 mm (c), 2.5 mm (d). Copyright 2015 (Adapted with permission from the American Association for the Advancement of Science).[87]

Hyaluronic acid (HA, also referred to as hyaluronan) is a ubiquitous, high molecular weight glycosaminoglycan found in the connective and epithelial tissues of vertebrates.[93] Notably, hyaluronic acid is a component of the extracellular matrix, and has a high rate of synthetic turnover in the body. As its name suggests, HA is anionic at physiological pH due to the partial ionization of its carboxylic acid groups. Lindén, Groll, and colleagues[75] used HA as part of a shear-thinning, printable hydrogel in a study of the release kinetics of nanoparticles from 3D printed scaffolds. In this system, mesoporous silica nanoparticles (MSNs), which have been investigated as potential drug delivery vehicles, were functionalized with surface carboxy (COOH) or amino (NH_2) groups.

The derivatized MSNs were mixed with hydrogels composed of HA and thiol-ene cross-linked poly(glycidol)s, and the composite hydrogels were used to print multilayer lattices. These lattices were submerged in media containing C2C12 mouse myoblast cells, and the release of MSNs from the gel scaffold, followed by uptake by the C2C12 cells, was monitored *via* fluorescent staining and confocal microscopy. The authors found that COOH-functionalized MSNs were released from the hydrogel quickly due to charge-charge repulsion between the nanoparticles and HA, while NH_2-functionalized MSNs were released more slowly due to favorable ionic attraction to the HA.

Lewis and co-workers[94] produced a 3D printable hydrogel ink from high-molecular weight poly(acrylamide) (PAm), acrylamide monomers, cross-linker, glycerol, and water. This ink demonstrated the shear-thinning properties required for extrusion and solidified upon post-print UV curing. Importantly, the 3D scaffolds printed with this formulation influenced 3T3 fibroblast morphology. PAm has also served as the covalently cross-linked polymer in ICE systems, particularly those coupled with alginate[88,89] or carrageenan.[95] In the former case,[89] the PAm/alginate gel ink was combined with a UV-curable polyurethane ink (Emax 904) to produce 3D printed objects with graduated mechanical properties based on the relative ratios of the two inks. In the latter case,[95] the reversible temperature response of κ-carrageenan, which cross-links in the presence of potassium ions, enabled the printing of stretchable, self-healing materials. Above approximately 45 °C, the PAm/carrageenan gels underwent a gel-sol transition, sealing any cuts and cracks and recovering mechanical integrity.

Light-induced reactions can be used to switch materials between a solidlike, hydrogel state and a soluble state. For example, Sumerlin and co-workers[96] utilized poly(*N*,*N*-dimethylacrylamide) (PDMAm) containing coumarin-functionalized comonomers. Upon exposure to long-wave UV (365 nm), the coumarin motifs underwent a [2+2] cycloaddition,

resulting in covalently cross-linked hydrogels. Following irradiation with short-wave UV (254 nm), the coumarin adducts underwent cycloreversion, and a soluble polymer solution was recovered. This strategy enabled the creation of photopatterned gels as well as hollow 3D printed objects.

Butcher and co-workers[97] used composite, photo-cross-linkable gels composed of HA-MA and gel-MA to fabricate trileaflet valves laden with human aortic valvular interstitial cells (HAVICs). Higher proportions of gel-MA resulted in gels with lower compressive moduli, *i.e.* gels that were less stiff and more viscous. These gels were dual stimuli-responsive, showing shear-thinning behavior to enable DIW, along with UV-mediated cross-linking to increase gel modulus. The different mechanical properties induced by changing composition resulted in differential cellular proliferation and secretory activity. Another excellent example of 3D bioprinting with multi-stimuli-responsive hydrogels is the use of kappa-carrageenan (κCA), a sulfated polysaccharide, in the presence of nanosilicates (such as Laponite XLS) and K^+ ions.[98] Heating κCA in water results in random polysaccharide coils, but upon cooling, double helices form due to hydrogen-bonding interactions. Monovalent ions like K^+ interact with the negatively-charged sulfate groups, providing a second means of cross-linking and enhancing the mechanical properties of κCA hydrogels. Gaharwar and colleagues took advantage of this dual-cross-linking; while κCA by itself was not extrudable, the addition of nanosilicates lowered the gelation temperature by disrupting polymer-polymer interactions, thereby facilitating extrusion at the biologically relevant temperature of 37 °C. Addition of KCl to the printed constructs resulted in ionic cross-links, increasing the gel modulus. This work demonstrates the potential to print cell-laden constructs at biological temperatures, while maintaining mechanical stiffness after printing.

Some extrudable hydrogels are cross-linked *via* non-covalent, non-ionic interactions. These include hydrogen-bonding, guest-host interactions, and protein-protein interactions. As an example, Heilshorn and co-workers[84] modified alginate with proline-rich peptides and then combined it with a recombinant protein containing the complementary peptide binding domain (Figure 1.7). The resulting system, referred to as a mixing-induced two-component hydrogel (MITCH), allowed homogeneous incorporation of NIH 3T3 fibroblasts and human adipose-derived stem cells due to the weak interaction of the peptide domains. Following extrusion, the system was cross-linked with calcium ions, resulting in a more rigid gel.

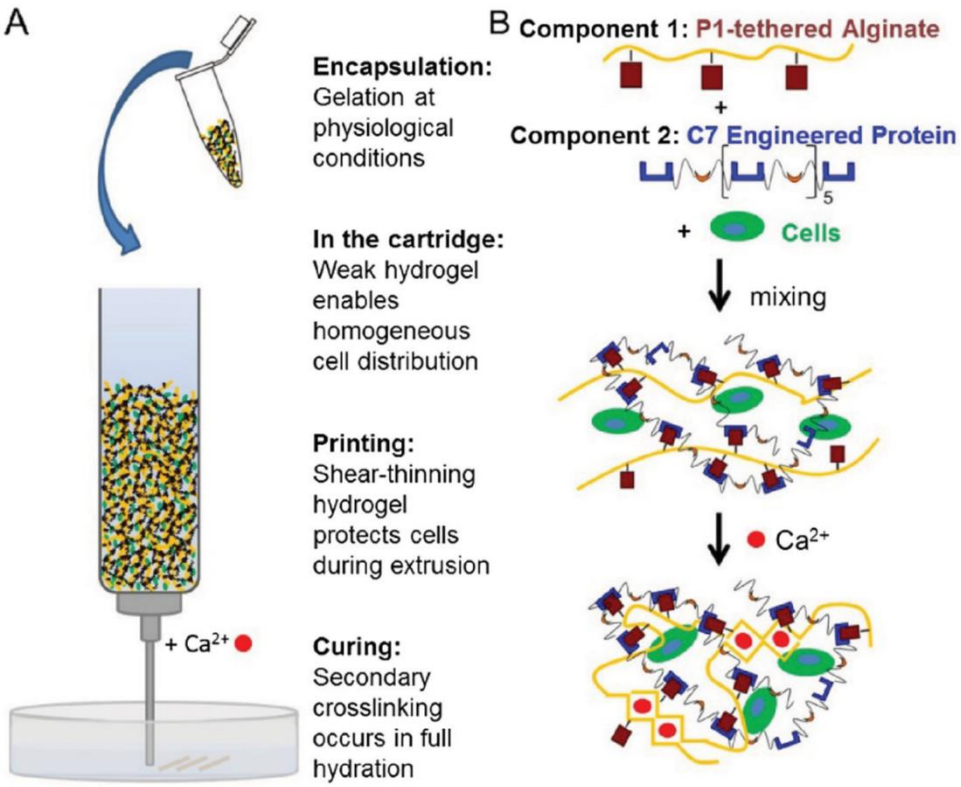

Figure 1.7. Mixing-induced two-component hydrogel printing (MITCH)
(a) Graphical representation of MITCH printing. (b) MITCH inks were composed of alginate tethered to a proline-rich peptide (P1) and a recombinant protein (C7) containing the complementary peptide-binding domain. Non-covalent interactions between P1 and C7 resulted in a weak, extrudable hydrogel. Ionic cross-linking of the alginate by Ca^{2+} ions after extrusion strengthened the printed structures. Copyright 2016 (Adapted with permission from Wiley-VCH).[84]

HA functionalized with adamantane (Ad-HA) and β-cyclodextrin (CD-HA) was used as both a self-healing support bath and an extrudable ink, in a process termed direct writing of guest-host hydrogels (or "GHost writing") (Figure 1.8).[99] In this strategy, the known guest-host interaction of adamantane and β-cyclodextrin imparted shear-thinning and self-healing characteristics to the HA gels. The authors could therefore print freeform, biocompatible structures

at high resolutions. The supramolecular guest-host interaction between Ad-HA and CD-HA afforded shear-thinning hydrogel inks with the viscoelastic properties necessary for DIW. For the support baths, Ad-HA and CD-HA with higher degrees of functionalization (40% of HA repeat units modified) than the extrudable ink were used. These support baths yielded to the moving print nozzle during DIW, but self-healed and resisted permanent deformation. Additional derivatization of HA with methacrylate groups (Me-HA) also made the support bath gels cross-linkable by UV irradiation. To demonstrate the utility of GHost writing, an ink gel composed of Ad-HA and CD-HA was printed into a support bath composed of Ad-HA, CD-HA, and Me-HA. Following extrusion, the support gel was cross-linked by UV irradiation, and the extruded ink gel was removed by pressure-induced flow, resulting in a channel network. The reverse strategy was also demonstrated, wherein a methacrylated ink gel was extruded into a non-methacrylated support gel. Following UV cross-linking of the ink gel, the support gel was washed away using a solution of excess β-cyclodextrin, removing any gel that was not covalently cross-linked.

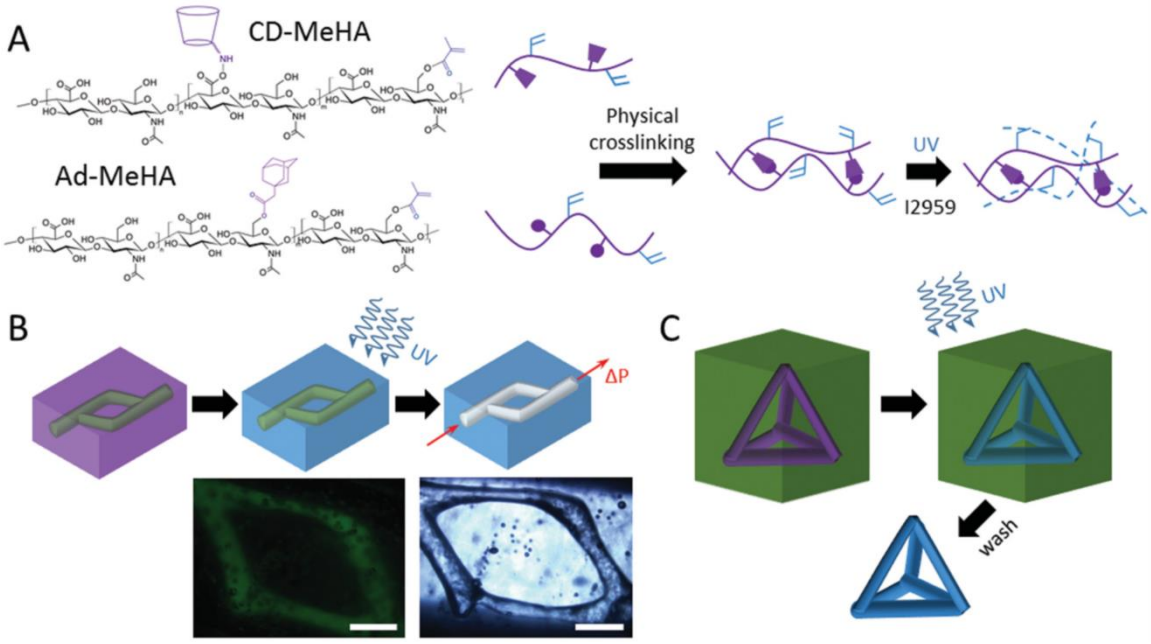

Figure 1.8. Direct writing of guest-host hydrogels ("GHost Writing")
(a) Hyaluronic acid was functionalized with methacrylate groups (blue) or adamantane and β-cyclodextrin (purple). Inks were cross-linked by non-covalent host-guest interactions between adamantane and β-cyclodextrin, as well as by free-radical polymerization of methacrylate groups. (b) Channels were made by curing a photo-cross-linkable support gel around a removable ink. (c) Self-supporting structures were printed with a UV-curable ink into a removable support gel, which was washed away with excess β-cyclodextrin. Scale bars = 500 μm. Copyright 2015 (Adapted with permission from Wiley-VCH).[99]

The applications and formulations of DIW polymer hydrogels are virtually limitless. However, strategies to enable or enhance printability are sometimes complex, requiring multiple synthetic transformations or processing steps. There are many molecular and nanoscale factors that affect the macroscale characteristics of a DIW ink. When formulating polymeric materials, for example, one may change the monomer composition itself, the degree of polymerization, the architecture, the side-group, or the end-group composition. Additionally, 3D constructs may be cross-linked or chemically functionalized after printing. By changing the identity of the monomer,

the new polymer takes on different physical properties, such as T_g and T_m, texture, hardness, and so on. The change in monomer may appear subtle at a superficial level, such as changing ethylene to ethylene oxide. Of course, poly(ethylene) is a waxy thermoplastic used in plastic bags, bottles, and films, while poly(ethylene oxide) is a water-soluble material used in laxatives, pharmaceuticals, and personal care products. Changes to monomer structure often have dramatic effects on the chemical and physical properties of the resulting polymers. However, this strategy faces severe limitations if alterations to the monomer make polymerization difficult. Unless the target polymer is well-studied, different monomers may require costly and time-consuming optimization of novel or existing polymerization techniques.

There is clearly a need to simplify the formulation and modification of hydrogels for DIW AM. In the following chapters, several different strategies for enhancing stimuli-responsive DIW hydrogels are discussed. Chapter 2 and Chapter 3 cover the development of a triblock copolymer platform with polymer chain-ends designed to alter temperature and shear response. Chapter 4, by contrast, details the formulation of a naturally-derived bioink based on decellularized extracellular matrix (dECM).

1.3 ACKNOWLEDGEMENTS

Partially adapted with permission from Shafranek, R.T.; Millik, S.C.; Smith, P.T.; Lee, C.-U.; Boydston, A.J.; Nelson, A. Stimuli-Responsive Materials in Additive Manufacturing. *Prog. Polym. Sci.* **2019**, *93*, 36-67. Copyright 2019 Elsevier.

1.4 REFERENCES

(1) Schmaljohann, D. Thermo- and PH-Responsive Polymers in Drug Delivery. *Adv. Drug*

Deliv. Rev. **2006**, *58* (15), 1655–1670.
(2) Jochum, F. D.; Theato, P. Temperature- and Light-Responsive Smart Polymer Materials. *Chem. Soc. Rev.* **2013**, *42* (17), 7468–7483.
(3) Zhao, Y. Light-Responsive Block Copolymer Micelles. *Macromolecules* **2012**, *45* (9), 3647–3657.
(4) Liang, X.; Guo, S.; Chen, M.; Li, C.; Wang, Q.; Zou, C.; Zhang, C.; Zhang, L.; Guo, S.; Yang, H. A Temperature and Electric Field-Responsive Flexible Smart Film with Full Broadband Optical Modulation. *Mater. Horizons* **2017**, *4* (5), 878–884.
(5) Ponomarenko, A. T.; Shevchenko, V. G.; Klason, C.; Pristupa, A. I. Magnetic-Field-Sensitive Polymer Composite Materials. *Smart Mater. Struct.* **1994**, *3*, 409–415.
(6) Du, J.-Z.; Du, X.-J.; Mao, C.-Q.; Wang, J. Tailor-Made Dual PH-Sensitive Polymer-Doxorubicin Nanoparticles for Efficient Anticancer Drug Delivery. *J. Am. Chem. Soc.* **2011**, *133* (44), 17560–17563.
(7) Cho, H.; Bae, J.; Garripelli, V. K.; Anderson, J. M.; Jun, H.-W.; Jo, S. Redox-Sensitive Polymeric Nanoparticles for Drug Delivery. *Chem. Commun.* **2012**, *48*, 6043–6045.
(8) Wen, Y.; Zhang, Z.; Li, J. Highly Efficient Multifunctional Supramolecular Gene Carrier System Self-Assembled from Redox-Sensitive and Zwitterionic Polymer Blocks. *Adv. Funct. Mater.* **2014**, *24* (25), 3874–3884.
(9) Li, J.; Nagamani, C.; Moore, J. S. Polymer Mechanochemistry: From Destructive to Productive. *Acc. Chem. Res.* **2015**, *48* (8), 2181–2190.
(10) Peterson, G. I.; Larsen, M. B.; Ganter, M. A.; Storti, D. W.; Boydston, A. J. 3D-Printed Mechanochromic Materials. *ACS Appl. Mater. Interfaces* **2015**, *7* (1), 577–583.
(11) Cao, B.; Boechler, N.; Boydston, A. J. Additive Manufacturing with a Flex Activated Mechanophore for Nondestructive Assessment of Mechanochemical Reactivitiy in Complex Object Geometries. *Polym. (United Kingdom)* **2018**, *152*, 1–5.
(12) Larsen, M. B.; Boydston, A. J. Investigations in Fundamental and Applied Polymer Mechanochemistry. *Macromol. Chem. Phys.* **2016**, *217* (3), 354–364.
(13) Priya James, H.; John, R.; Alex, A.; Anoop, K. R. Smart Polymers for the Controlled Delivery of Drugs – a Concise Overview. *Acta Pharm. Sin. B* **2014**, *4* (2), 120–127.
(14) Woodruff, M. A.; Hutmacher, D. W. The Return of a Forgotten Polymer - Polycaprolactone in the 21st Century. *Prog. Polym. Sci.* **2010**, *35* (10), 1217–1256.
(15) Pereira, R. F.; Bártolo, P. J. 3D Photo-Fabrication for Tissue Engineering and Drug Delivery. *Engineering* **2015**, *1* (1), 90–112.
(16) Hospodiuk, M.; Dey, M.; Sosnoski, D.; Ozbolat, I. T. The Bioink: A Comprehensive Review on Bioprintable Materials. *Biotechnol. Adv.* **2017**, *35* (2), 217–239.
(17) Jose, R. R.; Rodriguez, M. J.; Dixon, T. A.; Omenetto, F.; Kaplan, D. L. Evolution of Bioinks and Additive Manufacturing Technologies for 3D Bioprinting. *ACS Biomater. Sci. Eng.* **2016**, *2* (10), 1662–1678.
(18) Hutmacher, D. W. Scaffolds in Tissue Engineering Bone and Cartilage. *Biomaterials* **2000**, *21* (24), 2529–2543.
(19) Chang, C. C.; Boland, E. D.; Williams, S. K.; Hoying, J. B. Direct-Write Bioprinting Three-Dimensional Biohybrid Systems for Future Regenerative Therapies. *J. Biomed. Mater. Res. - Part B Appl. Biomater.* **2011**, *98B* (1), 160–170.
(20) Li, Y. C.; Zhang, Y. S.; Akpek, A.; Shin, S. R.; Khademhosseini, A. 4D Bioprinting: The next-Generation Technology for Biofabrication Enabled by Stimuli-Responsive Materials. *Biofabrication* **2017**, *9* (1), 012001(1-16).

(21) Placone, J. K.; Engler, A. J. Recent Advances in Extrusion-Based 3D Printing for Biomedical Applications. *Adv. Healthc. Mater.* **2018**, *7* (8), 1701161(1-11).
(22) Pereira, R. F.; Bártolo, P. J. 3D Bioprinting of Photocrosslinkable Hydrogel Constructs. *J. Appl. Polym. Sci.* **2015**, *132* (48), 42458(1-15).
(23) Truby, R. L.; Lewis, J. A. Printing Soft Matter in Three Dimensions. *Nature* **2016**, *540* (7633), 371–378.
(24) Kalsoom, U.; Nesterenko, P. N.; Paull, B. Recent Developments in 3D Printable Composite Materials. *RSC Adv.* **2016**, *6* (65), 60355–60371.
(25) Ligon, S. C.; Liska, R.; Stampfl, J.; Gurr, M.; Mülhaupt, R. Polymers for 3D Printing and Customized Additive Manufacturing. *Chem. Rev.* **2017**, *117* (15), 10212–10290.
(26) Bekas, D. G.; Tsirka, K.; Baltzis, D.; Paipetis, A. S. Self-Healing Materials: A Review of Advances in Materials, Evaluation, Characterization and Monitoring Techniques. *Compos. Part B Eng.* **2016**, *87*, 92–119.
(27) Lin, D.; Nian, Q.; Deng, B.; Jin, S.; Hu, Y.; Wang, W.; Cheng, G. J. Three-Dimensional Printing of Complex Structures: Man Made or toward Nature? *ACS Nano* **2014**, *8* (10), 9710–9715.
(28) De Leon, A. C.; Chen, Q.; Palaganas, N. B.; Palaganas, J. O.; Manapat, J.; Advincula, R. C. High Performance Polymer Nanocomposites for Additive Manufacturing Applications. *React. Funct. Polym.* **2016**, *103*, 141–155.
(29) Studart, A. R. Additive Manufacturing of Biologically-Inspired Materials. *Chem. Soc. Rev.* **2016**, *45* (2), 359–376.
(30) Zein, I.; Hutmacher, D. W.; Tan, K. C.; Teoh, S. H. Fused Deposition Modeling of Novel Scaffold Architectures for Tissue Engineering Applications. *Biomaterials* **2002**, *23* (4), 1169–1185.
(31) Crump, S. S. Apparatus and Method for Creating Three-Dimensional Objects. 5,121,329, 1992.
(32) Ribeiro, A.; Blokzijl, M. M.; Levato, R.; Visser, C. W.; Castilho, M.; Hennink, W. E.; Vermonden, T.; Malda, J. Assessing Bioink Shape Fidelity to Aid Material Development in 3D Bioprinting. *Biofabrication* **2018**, *10* (1), 014102(1-9).
(33) Smith, P. T.; Basu, A.; Saha, A.; Nelson, A. Chemical Modification and Printability of Shear-Thinning Hydrogel Inks for Direct-Write 3D Printing. *Polym. (United Kingdom)* **2018**, *152*, 42–50.
(34) Paxton, N.; Smolan, W.; Böck, T.; Melchels, F.; Groll, J.; Jungst, T. Proposal to Assess Printability of Bioinks for Extrusion-Based Bioprinting and Evaluation of Rheological Properties Governing Bioprintability. *Biofabrication* **2017**, *9* (4), 044107(1-18).
(35) Mouser, V. H. M.; Melchels, F. P. W.; Visser, J.; Dhert, W. J. A.; Gawlitta, D.; Malda, J. Yield Stress Determines Bioprintability of Hydrogels Based on Gelatin-Methacryloyl and Gellan Gum for Cartilage Bioprinting. *Biofabrication* **2016**, *8* (3), 035003(1-13).
(36) Gao, T.; Gillispie, G. J.; Copus, J. S.; PR, A. K.; Seol, Y.-J.; Atala, A.; Yoo, J. J.; Lee, S. J. Optimization of Gelatin–Alginate Composite Bioink Printability Using Rheological Parameters: A Systematic Approach. *Biofabrication* **2018**, *10* (3), 034106(1-9).
(37) Faes, M.; Valkenaers, H.; Vogeler, F.; Vleugels, J.; Ferraris, E. Extrusion-Based 3D Printing of Ceramic Components. *Procedia CIRP* **2015**, *28*, 76–81.
(38) He, Y.; Yang, F.; Zhao, H.; Gao, Q.; Xia, B.; Fu, J. Research on the Printability of Hydrogels in 3D Bioprinting. *Sci. Rep.* **2016**, *6*, 29977(1-13).
(39) Engler, A. J.; Sen, S.; Sweeney, H. L.; Discher, D. E. Matrix Elasticity Directs Stem Cell

Lineage Specification. *Cell* **2006**, *126* (4), 677–689.
(40) Burdick, J. A.; Prestwich, G. D. Hyaluronic Acid Hydrogels for Biomedical Applications. *Adv. Mater.* **2011**, *23* (12), H41–H56.
(41) Khetan, S.; Burdick, J. A. Patterning Hydrogels in Three Dimensions towards Controlling Cellular Interactions. *Soft Matter* **2011**, *7* (3), 830–838.
(42) Kolesky, D. B.; Truby, R. L.; Gladman, A. S.; Busbee, T. A.; Homan, K. A.; Lewis, J. A. 3D Bioprinting of Vascularized, Heterogeneous Cell-Laden Tissue Constructs. *Adv. Mater.* **2014**, *26* (19), 3124–3130.
(43) Wang, H.; Heilshorn, S. C. Adaptable Hydrogel Networks with Reversible Linkages for Tissue Engineering. *Adv. Mater.* **2015**, *27* (25), 3717–3736.
(44) Rosales, A. M.; Anseth, K. S. The Design of Reversible Hydrogels to Capture Extracellular Matrix Dynamics. *Nat. Rev. Mater.* **2016**, *1* (2), 15012/1-15.
(45) Sershen, S. R.; Westcott, S. L.; Halas, N. J.; West, J. L. Temperature-Sensitive Polymer-Nanoshell Composites for Photothermally Modulated Drug Delivery. *J. Biomed. Mater. Res.* **2000**, *51* (3), 293–298.
(46) Yamagata, T.; Morishita, M.; Kavimandan, N. J.; Nakamura, K.; Fukuoka, Y.; Takayama, K.; Peppas, N. A. Characterization of Insulin Protection Properties of Complexation Hydrogels in Gastric and Intestinal Enzyme Fluids. *J. Control. Release* **2006**, *112* (3), 343–349.
(47) Webber, M. J.; Matson, J. B.; Tamboli, V. K.; Stupp, S. I. Controlled Release of Dexamethasone from Peptide Nanofiber Gels to Modulate Inflammatory Response. *Biomaterials* **2012**, *33* (28), 6823–6832.
(48) Sugiura, S.; Szilágyi, A.; Sumaru, K.; Hattori, K.; Takagi, T.; Filipcsei, G.; Zrínyi, M.; Kanamori, T. On-Demand Microfluidic Control by Micropatterned Light Irradiation of a Photoresponsive Hydrogel Sheet. *Lab Chip* **2009**, *9* (2), 196–198.
(49) Seuring, J.; Agarwal, S. Polymers with Upper Critical Solution Temperature in Aqueous Solution. *Macromol. Rapid Commun.* **2012**, *33*, 1898–1920.
(50) van Dijk, M. A.; Wakker, A. *Concepts of Polymer Thermodynamics, Volume 2*; Technomic Publishing Company, Inc.: Lancaster, PA, 1997.
(51) Chandler, D. Interfaces and the Driving Force of Hydrophobic Assembly. *Nature* **2005**, *437* (29), 640–647.
(52) Southall, N. T.; Dill, K. A.; Haymet, A. D. J. A View of the Hydrophobic Effect. *J. Phys. Chem. B* **2002**, *106* (3), 521–533.
(53) Wu, C.; Wang, X. Globule-to-Coil Transition of a Single Homopolymer Chain in Solution. *Phys. Rev. Lett.* **1998**, *80* (18), 4092–4094.
(54) Schild, H. G. Poly (N-Isopropylacrylamide): Experiment , Theory and Application. *Prog. Polym. Sci.* **1992**, *17*, 163–249.
(55) Shibayama, M.; Suda, J.; Karino, T.; Okabe, S.; Takehisa, T.; Haraguchi, K. Structure and Dynamics of Poly(N-Isopropylacrylamide)-Clay Nanocomposite Gels. *Macromolecules* **2004**, *37* (25), 9606–9612.
(56) Bakarich, S. E.; Gorkin, R.; Panhuis, M. In Het; Spinks, G. M. 4D Printing with Mechanically Robust, Thermally Actuating Hydrogels. *Macromol. Rapid Commun.* **2015**, *36* (12), 1211–1217.
(57) Sydney Gladman, A.; Matsumoto, E. A.; Nuzzo, R. G.; Mahadevan, L.; Lewis, J. A. Biomimetic 4D Printing. *Nat. Mater.* **2016**, *15* (4), 413–418.
(58) Naficy, S.; Gately, R.; Gorkin, R.; Xin, H.; Spinks, G. M. 4D Printing of Reversible Shape

Morphing Hydrogel Structures. *Macromol. Mater. Eng.* **2017**, *302* (1), 1600212/1-9.
(59) Nadgorny, M.; Collins, J.; Xiao, Z.; Scales, J.; Connal, L. A. 3D-Printing of Dynamic Self-Healing Cryogels with Tuneable Properties. *Polym. Chem.* **2018**, *9*, 1684–1692.
(60) Prud'homme, R. K.; Wu, G.; Schneider, D. K. Structure and Rheology Studies of Poly(Oxyethylene−oxypropylene−oxyethylene) Aqueous Solution. *Langmuir* **1996**, *12* (20), 4651–4659.
(61) Mortensen, K. Structural Studies of Aqueous Solutions of PEO - PPO - PEO Triblock Copolymers, Their Micellar Aggregates and Mesophases; a Small-Angle Neutron Scattering Study. *J. Phys. Condens. Matter* **1996**, *8* (25A), A103–A124.
(62) Alexandridis, P.; Holzwarth, J. F.; Hatton, T. A. Micellization of Poly(Ethylene Oxide)-Poly(Propylene Oxide)-Poly(Ethylene Oxide) Triblock Copolymers in Aqueous Solutions: Thermodynamics of Copolymer Association. *Macromolecules* **1994**, *27* (9), 2414–2425.
(63) Pragatheeswaran, A. M.; Chen, S. B. Effect of Chain Length of PEO on the Gelation and Micellization of the Pluronic F127 Copolymer Aqueous System. *Langmuir* **2013**, *29* (31), 9694–9701.
(64) Chandaroy, P.; Sen, A.; Alexandridis, P.; Hui, S. W. Utilizing Temperature-Sensitive Association of Pluronic F-127 with Lipid Bilayers to Control Liposome-Cell Adhesion. *Biochim. Biophys. Acta - Biomembr.* **2002**, *1559* (1), 32–42.
(65) Alexandridis, P.; Alan Hatton, T. Poly(Ethylene Oxide)Poly(Propylene Oxide)Poly(Ethylene Oxide) Block Copolymer Surfactants in Aqueous Solutions and at Interfaces: Thermodynamics, Structure, Dynamics, and Modeling. *Colloids Surfaces A Physicochem. Eng. Asp.* **1995**, *96* (1–2), 1–46.
(66) Khattak, S. F.; Bhatia, S. R.; Roberts, S. C. Pluronic F127 as a Cell Encapsulation Material: Utilization of Membrane-Stabilizing Agents. *Tissue Eng.* **2005**, *11* (5–6), 974–983.
(67) Lorang, D. J.; Tanaka, D.; Spadaccini, C. M.; Rose, K. A.; Cherepy, N. J.; Lewis, J. A. Photocurable Liquid Core-Fugitive Shell Printing of Optical Waveguides. *Adv. Mater.* **2011**, *23* (43), 5055–5058.
(68) Wu, W.; Deconinck, A.; Lewis, J. A. Omnidirectional Printing of 3D Microvascular Networks. *Adv. Mater.* **2011**, *23* (24), 178–183.
(69) Basu, A.; Saha, A.; Goodman, C.; Shafranek, R. T.; Nelson, A. Catalytically Initiated Gel-in-Gel Printing of Composite Hydrogels. *ACS Appl. Mater. Interfaces* **2017**, *9* (46), 40898–40904.
(70) Li, L.; Zhang, P.; Zhang, Z.; Lin, Q.; Wu, Y.; Cheng, A.; Lin, Y.; Thompson, C. M.; Smaldone, R. A.; Ke, C. Hierarchical Co-Assembly Enhanced Direct Ink Writing. *Angew. Chemie - Int. Ed.* **2018**, *57* (18), 5105–5109.
(71) Müller, M.; Becher, J.; Schnabelrauch, M.; Zenobi-Wong, M. Nanostructured Pluronic Hydrogels as Bioinks for 3D Bioprinting. *Biofabrication* **2015**, *7* (3), 035006(1-17).
(72) Saha, A.; Johnston, T. G.; Shafranek, R. T.; Goodman, C. J.; Zalatan, J. G.; Storti, D. W.; Ganter, M. A.; Nelson, A. Additive Manufacturing of Catalytically Active Living Materials. *ACS Appl. Mater. Interfaces* **2018**, *10* (16), 13373–13380.
(73) Zhang, M.; Vora, A.; Han, W.; Wojtecki, R. J.; Maune, H.; Le, A. B. A.; Thompson, L. E.; McClelland, G. M.; Ribet, F.; Engler, A. C.; et al. Dual-Responsive Hydrogels for Direct-Write 3D Printing. *Macromolecules* **2015**, *48* (18), 6482–6488.
(74) Karis, D. G.; Ono, R. J.; Zhang, M.; Vora, A.; Storti, D.; Ganter, M. A.; Nelson, A. Cross-Linkable Multi-Stimuli Responsive Hydrogel Inks for Direct-Write 3D Printing. *Polym.*

Chem. **2017**, *8* (29), 4199–4206.
(75) Baumann, B.; Jungst, T.; Stichler, S.; Feineis, S.; Wiltschka, O.; Kuhlmann, M.; Lindén, M.; Groll, J. Control of Nanoparticle Release Kinetics from 3D Printed Hydrogel Scaffolds. *Angew. Chemie - Int. Ed.* **2017**, *56* (16), 4623–4628.
(76) Stichler, S.; Bock, T.; Paxton, N. C.; Bertlein, S.; Levato, R.; Schill, V.; Smolan, W.; Malda, J.; Tessmar, J.; Blunk, T.; et al. Double Printing of Hyaluronic Acid / Poly(Glycidol) Hybrid Hydrogels with Poly(Epsilon-Caprolactone) for MSC Chondrogenesis. *Biofabrication* **2017**, *9*, 044108/1-12.
(77) Xing, Q.; Yates, K.; Vogt, C.; Qian, Z.; Frost, M. C.; Zhao, F. Increasing Mechanical Strength of Gelatin Hydrogels by Divalent Metal Ion Removal. *Sci. Rep.* **2014**, *4*, 4706/1-10.
(78) Van Den Bulcke, A. I.; Bogdanov, B.; De Rooze, N.; Schacht, E. H.; Cornelissen, M.; Berghmans, H. Structural and Rheological Properties of Methacrylamide Modified Gelatin Hydrogels. *Biomacromolecules* **2000**, *1* (1), 31–38.
(79) GIMA. Gelatin Handbook. *GIMA, Gelatin Manuf. Inst. Am.* **2012**, 25.
(80) Aubin, H.; Nichol, J. W.; Hutson, C. B.; Bae, H.; Sieminski, A. L.; Cropek, D. M.; Akhyari, P.; Khademhosseini, A. Directed 3D Cell Alignment and Elongation in Microengineered Hydrogels. *Biomaterials* **2010**, *31* (27), 6941–6951.
(81) Nichol, J. W.; Koshy, S. T.; Bae, H.; Hwang, C. M.; Yamanlar, S.; Khademhosseini, A. Cell-Laden Microengineered Gelatin Methacrylate Hydrogels. *Biomaterials* **2010**, *31* (21), 5536–5544.
(82) Billiet, T.; Gevaert, E.; De Schryver, T.; Cornelissen, M.; Dubruel, P. The 3D Printing of Gelatin Methacrylamide Cell-Laden Tissue-Engineered Constructs with High Cell Viability. *Biomaterials* **2014**, *35* (1), 49–62.
(83) K. Y. Lee, D. J. M. Alginate: Properties and Biomedical Applications. *Prog. Polym. Sci.* **2012**, *37* (1), 106–126.
(84) Dubbin, K.; Hori, Y.; Lewis, K. K.; Heilshorn, S. C. Dual-Stage Crosslinking of a Gel-Phase Bioink Improves Cell Viability and Homogeneity for 3D Bioprinting. *Adv. Healthc. Mater.* **2016**, *5* (19), 2488–2492.
(85) Hockaday, L. A.; Kang, K. H.; Colangelo, N. W.; Cheung, P. Y. C.; Duan, B.; Malone, E.; Wu, J.; Girardi, L. N.; Bonassar, L. J.; Lipson, H.; et al. Rapid 3D Printing of Anatomically Accurate and Mechanically Heterogeneous Aortic Valve Hydrogel Scaffolds. *Biofabrication* **2012**, *4* (3), 035005/1-12.
(86) Lode, A.; Krujatz, F.; Brüggemeier, S.; Quade, M.; Schütz, K.; Knaack, S.; Weber, J.; Bley, T.; Gelinsky, M. Green Bioprinting: Fabrication of Photosynthetic Algae-Laden Hydrogel Scaffolds for Biotechnological and Medical Applications. *Eng. Life Sci.* **2015**, *15* (2), 177–183.
(87) Hinton, T. J.; Jallerat, Q.; Palchesko, R. N.; Park, J. H.; Grodzicki, M. S.; Shue, H.-J.; Ramadan, M. H.; Hudson, A. R.; Feinberg, A. W. Three-Dimensional Printing of Complex Biological Structures by Freeform Reversible Embedding of Suspended Hydrogels. *Sci Adv.* **2015**, *1* (9), e1500758/1-10.
(88) Bakarich, S. E.; III, R. G.; Naficy, S.; Gately, R.; Panhuis, M. in het; Spinks, G. M. 3D/4D Printing Hydrogel Composites: A Pathway to Functional Devices. *MRS Adv.* **2016**, *1* (8), 521–526.
(89) Bakarich, S. E.; Gorkin, R.; Gately, R.; Naficy, S.; in het Panhuis, M.; Spinks, G. M. 3D Printing of Tough Hydrogel Composites with Spatially Varying Materials Properties.

Addit. Manuf. **2017**, *14*, 24–30.
(90) Shull, K. R. Materials Science: A Hard Concept in Soft Matter. *Nature* **2012**, *489* (7414), 36–37.
(91) Bakarich, S. E.; Pidcock, G. C.; Balding, P.; Stevens, L.; Calvert, P.; In Het Panhuis, M. Recovery from Applied Strain in Interpenetrating Polymer Network Hydrogels with Ionic and Covalent Cross-Links. *Soft Matter* **2012**, *8* (39), 9985–9988.
(92) Ren, Y.; Lou, R.; Liu, X.; Gao, M.; Zheng, H.; Yang, T.; Xie, H.; Yu, W.; Ma, X. A Self-Healing Hydrogel Formation Strategy: Via Exploiting Endothermic Interactions between Polyelectrolytes. *Chem. Commun.* **2016**, *52* (37), 6273–6276.
(93) Fraser, J. R. E.; Laurent, T. C.; Laurent, U. B. G. Hyaluronan: Its Nature, Distribution, Functions and Turnover. *J. Intern. Med.* **1997**, *242* (1), 27–33.
(94) Barry, R. A.; Shepherd, R. F.; Hanson, J. N.; Nuzzo, R. G.; Wiltzius, P.; Lewis, J. A. Direct-Write Assembly of 3D Hydrogel Scaffolds for Guided Cell Growth. *Adv. Mater.* **2009**, *21* (23), 2407–2410.
(95) Liu, S.; Li, L. Ultrastretchable and Self-Healing Double-Network Hydrogel for 3D Printing and Strain Sensor. *ACS Appl. Mater. Interfaces* **2017**, *9* (31), 26429–26437.
(96) Kabb, C. P.; O'Bryan, C. S.; Deng, C. C.; Angelini, T. E.; Sumerlin, B. S. Photoreversible Covalent Hydrogels for Soft-Matter Additive Manufacturing. *ACS Appl. Mater. Interfaces* **2018**, *10* (19), 16793–16801.
(97) Duan, B.; Kapetanovic, E.; Hockaday, L. A.; Butcher, J. T. Three-Dimensional Printed Trileaflet Valve Conduits Using Biological Hydrogels and Human Valve Interstitial Cells. *Acta Biomater.* **2014**, *10* (5), 1836–1846.
(98) Wilson, S. A.; Cross, L. M.; Peak, C. W.; Gaharwar, A. K. Shear-Thinning and Thermo-Reversible Nanoengineered Inks for 3D Bioprinting. *ACS Appl. Mater. Interfaces* **2017**, *9* (50), 43449–43458.
(99) Highley, C. B.; Rodell, C. B.; Burdick, J. A. Direct 3D Printing of Shear-Thinning Hydrogels into Self-Healing Hydrogels. *Adv. Mater.* **2015**, *27* (34), 5075–5079.

Chapter 2. STICKY ENDS IN A SELF-ASSEMBLING ABA TRIBLOCK COPOLYMER: THE ROLE OF UREAS IN STIMULI-RESPONSIVE HYDROGELS

2.1 ABSTRACT

Directing polymer self-assembly through noncovalent interactions is a powerful way to control the structure and function of nanoengineered materials. Dynamic hydrogen bonds are particularly useful for materials with structures that change over time or in response to specific stimuli. In the present work, we use the supramolecular association of urea moieties to manipulate the morphology, thermal response, and mechanical properties of soft polymeric hydrogels. Urea-terminated poly(isopropyl glycidyl ether)-*b*-poly(ethylene oxide)-*b*-poly(isopropyl glycidyl ether) ABA triblock copolymers were synthesized using controlled, anionic ring-opening polymerization and subsequent chain-end functionalization. Triblock copolymers with hydroxy end-groups were incapable of hydrogelation, while polymers terminated with meta-bisurea motifs formed robust gels at room temperature. Rheometric analysis of the bulk gels, variable-temperature infrared spectroscopy (VT-IR), differential scanning calorimetry (DSC), and small-angle X-ray scattering (SAXS) confirmed the formation of structured hydrogels via association of the meta-bis-urea end-groups. Monourea end-groups did not result in the same regular structure as the meta-bis-urea. In future, the reported hydrogels could be useful for elastomeric, shape-morphing 3D-printed constructs, or as biomimetic scaffolds with precisely tailored porosity and mechanical properties.

2.2 INTRODUCTION

Hydrogel-forming biopolymers, like collagen and gelatin, are exquisite examples of biopolymers that possess a defined composition, length, and sequence. These linear polymers fold or self-assemble into well-defined higher-order structures that can bind molecules and create three-dimensional scaffolds for cells. In the case of collagen, linear protein strands hierarchically assemble to form fibrous bundles that not only provide mechanical structure, but also present recognition sites that promote cellular adhesion.[1] Non-covalent interactions, including hydrogen bonding, ionic interactions, and van der Waals forces—introduced at precise locations along the polymer chain—drive the self-assembly of biopolymers.[2,3] Wholly synthetic polymers that show the same level of compositional precision are not possible yet, even using controlled polymerization techniques. Block copolymers that microphase separate have received significant attention in the polymer sciences based on their ability to organize into nano- and microscale morphologies.[4–7] However, these polymers do not self-assemble with the same level of complexity observed in proteins or DNA. While the sequence of polymer blocks can be controlled in a segmented block copolymer, the individual monomer sequence cannot. The design rules that govern the self-assembly of synthetic polymers with precisely defined monomer sequences is likely to be incredibly complex.[8] Accordingly, there is a need to develop a strategy to afford hierarchically self-assembled synthetic polymers that does not rely on precise monomer sequences. These alternative strategies could complement existing efforts to create sequence-controlled polymers.[9] The precision molecular engineering of polymers to control nanoscale architecture remains non-trivial.[10–14] However, the molecular-level design of nanostructured polymers and macromolecular materials (also referred to as nanoarchitectonics)[15–17] has led to the emergence of precisely self-assembled materials with catalytic behavior,[18,19] dynamic mechanical properties,[20]

and electromechanical actuation.[21] Nanoarchitectonic-based approaches to polymer design have recently been applied toward the fabrication of stimuli-responsive hydrogels.[22–25] Stimuli-responsive hydrogels[26] adapt to changes in their environments such as temperature,[27–30] pH and ion concentration,[31–35] and shear stress.[29,36–39] These 'smart' hydrogels are ideal for biomimetic tissues and tissue culture,[40–45] as well as drug-delivery systems.[46–48] In particular, shear-thinning hydrogels have potential as injectable therapeutics[36,37] and are excellent inks for direct-write 3D printing.[29,38,43,49] The manner by which polymeric hydrogels self-assemble and react to stimuli can be tuned with small molecular modifications to the main-chain, side-chain or end-group functionality. Despite the small fraction of the polymer chain that the end-groups represent, supramolecular functionalities at the chain termini can have dramatic effects on the characteristics of the resulting self-assembled networks.[50–52] Supramolecular hydrogen-bonding molecules can form ordered assemblies in solution and bulk polymer and can be incorporated into the design of a polymer.[53–58] For example, Sijbesma and Meijer demonstrated that the incorporation of the ureidopyrimidinone (UPy) motif can have a profound, measurable effect on polymer morphology in both solution and the bulk phase.[36,59–61] For hydrogels, the use of hydrogen-bonding groups influences not only morphology, but also moduli, shear-thinning characteristics, and thermoresponsive behavior.[36,37,62,63]

Herein, we report temperature and shear-responsive hydrogels composed of poly(isopropyl glycidyl ether)-*b*-poly(ethylene oxide)-*b*-poly(isopropyl glycidyl ether) (PiPGE-*b*-PEO-*b*-PiPGE). Our group has developed ABA triblock copolymers based on poly(alkyl glycidyl ether)s as platforms for stimuli-responsive hydrogels wherein 'A' is a poly(alkyl glycidyl ether) and 'B' is poly(ethylene oxide).[29,64] These block copolymers self-assemble into flower-like micelles (Figure 2.1) in aqueous media and form physically entangled micelle networks as the polymer

concentration increases.[29,65] Micellization is driven by the hydrophobic aggregation of the poly(alkyl glycidyl ether) blocks. Some poly(alkyl glycidyl ether)s, such as poly(ethyl glycidyl ether) have lower critical solution temperatures (LCSTs) as homopolymers.[66–68] Others, such as poly(isopropyl glycidyl ether), are insoluble at all temperatures and concentrations. However, when either of these alkyl glycidyl ethers is the 'A' component in a PEO-based ABA triblock copolymer, the copolymer has an LCST due to entropically-driven hydrophobic aggregation of the 'A' blocks. This phase transition results in self-supporting hydrogels only when the 'A' blocks constitute a volume fraction ≥ 20 wt%.

Ureas were chosen as the hydrogen-bonding group of choice for the present study due to their strong self-association and ability to form extended supramolecular arrays both as small molecules[69–76] as well as in segmented and block copolymers.[56,58,62,77–81] The introduction of urea motifs into block copolymers results in crystalline or semi-crystalline domains due to the regular pattern of intermolecular hydrogen bonds. The geometric structure of the array, as well as the strength of the hydrogen-bonding association, varies depending on the placement of the ureas within the block copolymer, as well as the nature of the substituents adjacent to the urea groups.[62,72,73,76,82–84]

In the case of stimuli-responsive hydrogels, ureas play an influential role in polymer self-assembly. In most cases, ureas are placed in a hydrophobic domain to minimize competing hydrogen-bonding interactions with water.[10,31,32] This placement allows the formation of supramolecular hydrogen-bonding arrays. Ideally, these hydrogen bonds act as physical cross-links between polymer chains, enhancing the mechanical strength of the resulting hydrogels while retaining shear-thinning, self-healing, and temperature-responsive characteristics.

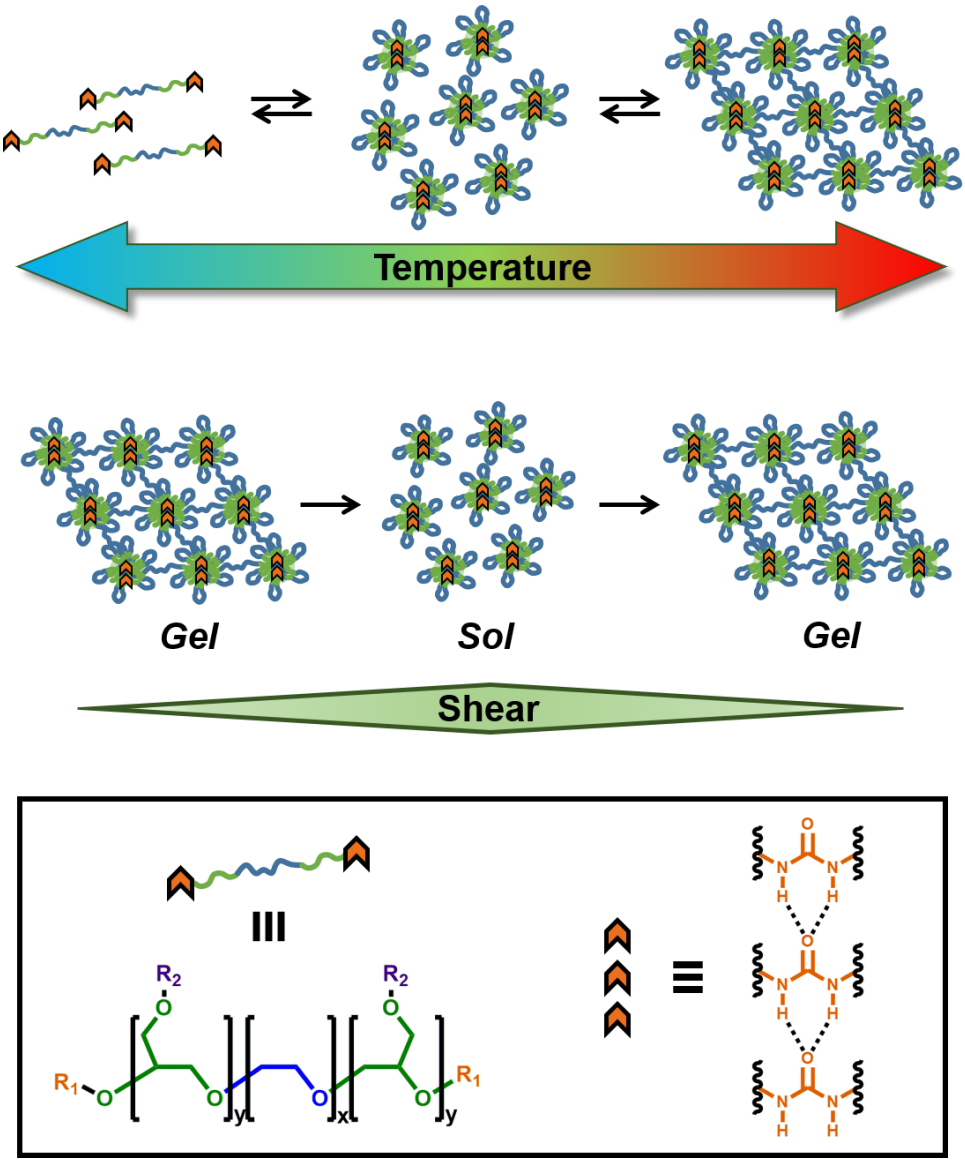

Figure 2.1. Dynamic, reversible self-assembly of amphiphilic triblock co-polymers in aqueous media

The equilibrium distribution of solvated unimers, flowerlike micelles, and physically entangled micelle networks changes with temperature (top). The hydrogel network can also be temporarily disrupted with shear stress (middle). Hydrogen-bonding end groups (orange chevrons) self-assemble in the hydrophobic domains, enhancing mechanical strength.

The polymers in the present study demonstrate that the inclusion of urea-containing hydrogen bonding groups at the chain ends can significantly alter the viscoelastic behavior of

multi-stimuli responsive hydrogels. Changes in morphology, mechanical properties, and thermal response demonstrate the enormous impact of relatively minor synthetic modifications and imply that hydrogen-bonding groups could be used to precisely tune the thermo- and mechano-responsive behavior of polymeric hydrogels.

2.3 Results and Discussion

We developed a modular route (Figure 2.2) to the syntheses of the polymers in this study. 8k-iPr-OH was synthesized via anionic ring-opening polymerization of iPGE initiated from PEO. Molecular weight was controlled by changing the ratio of iPGE monomer to PEO initiator, and dispersity indices were consistently low ($Đ < 1.2$). 8k-iPr-OH was derivatized with *boc*-glycine, and the protecting groups were removed under acidic conditions to afford an amine-functionalized polymer, 8k-iPr-NH_2. Further reactions with aryl isocyanates afforded the urea-terminated polymers 8k-iPr-U and 8k-iPr-bisU. GPC traces of the urea-terminated polymers indicated lower apparent molecular weights than the hydroxy-terminated polymer (Figure 2.13). This effect may have been due to the formation of compact aggregates by the urea-derivatized polymers in $CHCl_3$, which would have decreased the hydrodynamic radius of the polymer chains. Alternatively, the lower detected molecular weights could have been due to secondary retention, or noncovalent interactions between the polymers and the column material. 8k-iPr-bisU, in addition to having a smaller apparent molecular weight, showed a broader GPC trace and higher dispersity ($Đ = 1.68$) than 8k-iPr-OH ($Đ = 1.10$) and 8k-iPr-U ($Đ = 1.09$). The presence of a small, high molecular weight shoulder in the 8k-iPr-bisU trace suggested that a small degree of step-growth polymerization may have occurred, and accounts for the increased dispersity. No such shoulders were present for 8k-iPr-U, which was incapable of step-growth polymerization.

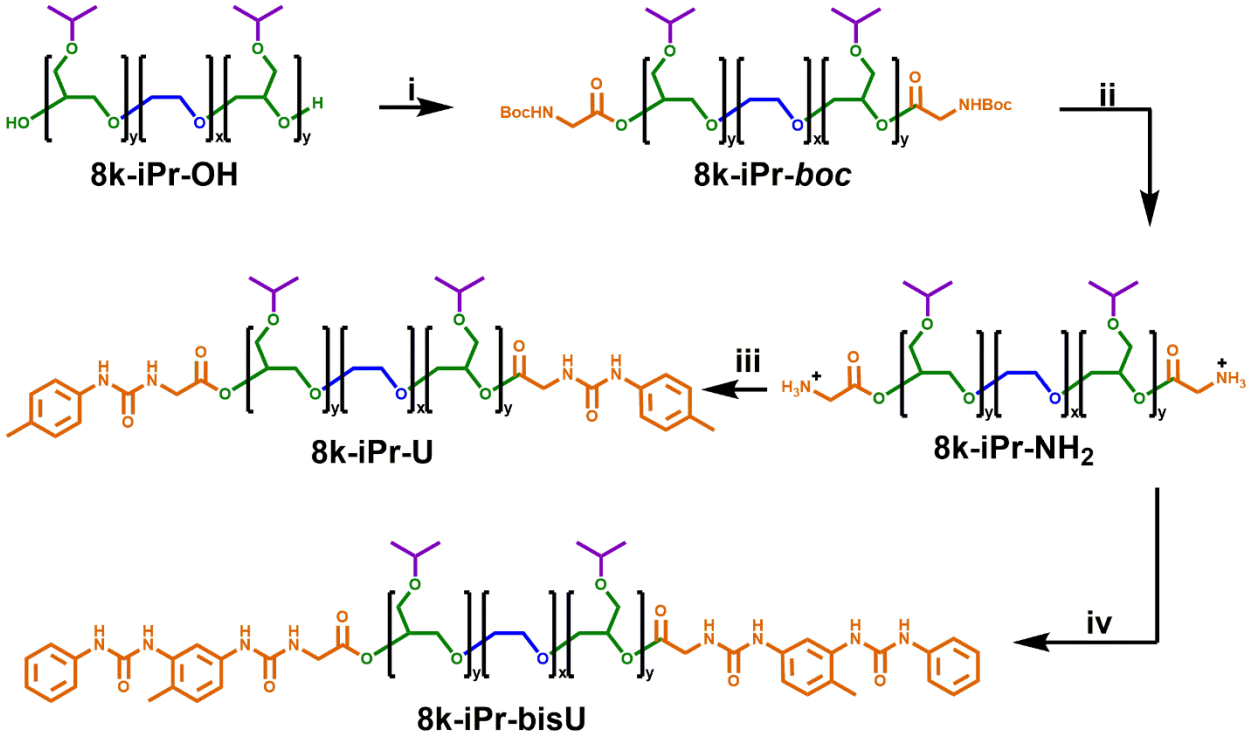

Figure 2.2. Chain-end functionalization of the 8k-iPr-OH triblock co-polymer
For each of the polymers, x ~ 182 and y ~ 8 (M_n ~ 9,900 g mol^{-1}). (i) DCC/*Boc*-gly (excess); DMAP (cat.); CH_2Cl_2, reflux, 24 h. (ii) 1:1 v/v TFA:CH_2Cl_2; RT, 18 h. (iii) *p*-Tolyl isocyanate/NEt_3; CH_2Cl_2, RT, 18 h. (iv) (1) Tolylene-2,4-diisocyanate (excess)/NEt_3; CH_2Cl_2, RT, 16 h. (2) Aniline (excess); CH_2Cl_2, RT, 21 h.

2.3.1 *Phase Diagrams and Rheometric Experiments*

The incorporation of the single- and bis-urea motifs to the chain ends of 8k-iPr-OH (to afford 8k-iPr-U and 8k-iPr-bisU, respectively) altered the viscoelastic behaviors of the corresponding aqueous solutions or gels. Phase diagrams were constructed by preparing a series of polymer solutions as described in the experimental section at different concentrations (2–30 wt% in DI water) and performing rheometric temperature-ramp experiments for each concentration. Relevant data from the temperature-ramp experiments are summarized in Table 2.1.

At the end of the temperature-ramp tests, the urea-functionalized polymer hydrogels were stiffer than the unfunctionalized gels, as indicated by greater *G′* values.

Table 2.1. Rheometric temperature-ramp data for 25 wt% 8k-iPr-OH, 8k-iPr-U, and 8k-iPr-bisU

Polymer	T_{gel} **(°C)**	**Crossover modulus (Pa)**	***G'* at 50 °C (Pa)**
8k-iPr-OH	39.6	6.25	2,460
8k-iPr-U	37.2	62.2	2,480
8k-iPr-bisU	14.9	765	10,100

As expected, the introduction of chain-end ureas lowered both the gelation temperature (T_{gel}) for a particular concentration, as well as the minimum polymer concentration (C_{min}) required for gelation at a particular temperature (Figure 2.3). The reduction of T_{gel} in 8k-iPr-bisU gels was due to both hydrophobic and hydrogen-bonding interactions. The aryl bis-urea chain ends were hydrophobic, as evidenced by qualitative solubility tests of small-molecule aryl urea analogs (Table 2.3). The introduction of aryl bis-urea chain ends therefore increased the overall hydrophobicity of the PiPGE 'A' blocks in 8k-iPr-bisU, driving micellization at lower temperatures. Strong hydrogen-bonding interactions between the bis-urea chain-ends resulted in microphase separation of crystalline domains, as supported by DSC and SAXS, to be discussed in a later section. The presence of these "hard" domains likely were responsible for imparting gel-like mechanical properties to the 8k-iPr-bisU gel. Therefore, the increased hydrophobicity of 8k-iPr-bisU shifted the equilibrium distribution of solvated polymer chains and bridged/unbridged flowerlike micelles, while the strong hydrogen-bonding interactions slowed exchange dynamics between micellized and water-solvated polymer chains. As a result, the T_{gel} decreased with the introduction of hydrogen-bonding domains. Surprisingly, the monourea end-group in 8k-iPr-U had

a subtle, almost imperceptible effect on the thermal response of the hydrogels, as depicted in the phase diagrams (Figure 2.3 (b)).

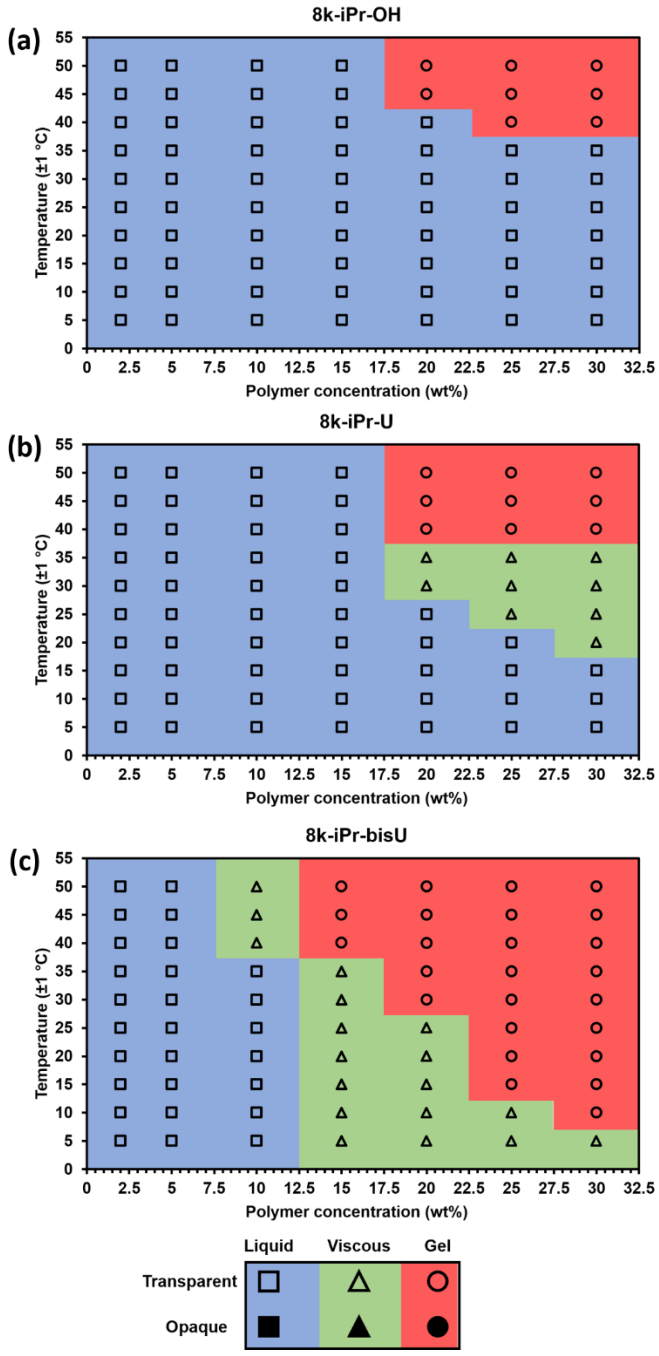

Figure 2.3. Temperature-concentration phase diagrams for 8k-iPr polymers

Phase diagrams for (a) 8k-iPr-OH, (b) 8k-iPr-U, and (c) 8k-iPr-bisU. These phase diagrams were prepared using data from temperature-ramp experiments (Figure 2.4 (a)).

While a single urea lowered the T_{gel} for each solution slightly, the most noticeable effect of monourea chain ends was the appearance of a viscous regime at higher concentrations and temperatures (≥ 20 wt% and ≥ 20 °C). While 8k-iPr-OH underwent a transition directly from free-flowing solution to self-supporting gel, 8k-iPr-U first became thick and viscous before becoming a free-standing gel. The increased viscosity and slightly lowered gelation temperature of 8k-iPr-U solutions was likely the result of hydrophobic aggregation of the terminal ureas. 8k-iPr-bisU exhibited a much broader "viscous" range and gelled at a much lower temperature and concentration than 8k-iPr-OH and 8k-iPr-U. It is likely that the bis-urea domains never became fully solvated, except perhaps at polymer concentrations < 10 wt%. This hypothesis was supported by VT-IR experiments (discussed later) and by the extreme hydrophobicity of a small-molecule bis-urea analog (Table 2.3), which would not dissolve in water at any temperature, even at concentrations < 0.5 mg mL^{-1}.

Based on comparisons of the phase diagrams for each polymer, 25 wt% was chosen as the concentration at which to compare rheological properties. All tests were conducted at 25 °C. As the phase diagrams suggest, 8k-iPr-bisU was a gel at this temperature, 8k-iPr-U was a viscous solution, and 8k-iPr-OH was a free-flowing solution. Indeed, 8k-iPr-bisU showed the self-healing and shear-thinning properties expected of these stimuli-responsive hydrogels. The dynamic oscillatory strain test, in which the material was subjected to alternating periods of high (100%) and low (1%) strain amplitude, indicated that at 25 wt% and 25 °C, 8k-iPr-bisU behaved as a solid gel at low strain and as a viscous fluid at high strain (Figure 2.4 (b)). Importantly, the material yielded and recovered almost instantaneously, with minimal mechanical hysteresis between strain cycles. With increasing shear rate, the viscosity of the 8k-iPr-bisU gel decreased over four orders of magnitude (Figure 2.4 (f)). This shear-thinning behavior confirmed the gelled nature of 8k-iPr-

bisU and demonstrated its suitability as an injectable or extrudable gel. By contrast, the viscosities of 8k-iPr-OH and 8k-iPr-U solutions were largely independent of shear rate, suggesting that they were more like viscous liquids than elastic solids. Note that the viscosity of the 8k-iPr-U solution was consistently greater than that of 8k-iPr-OH at most shear rates, reflecting the thicker nature of the 8k-iPr-U solution.

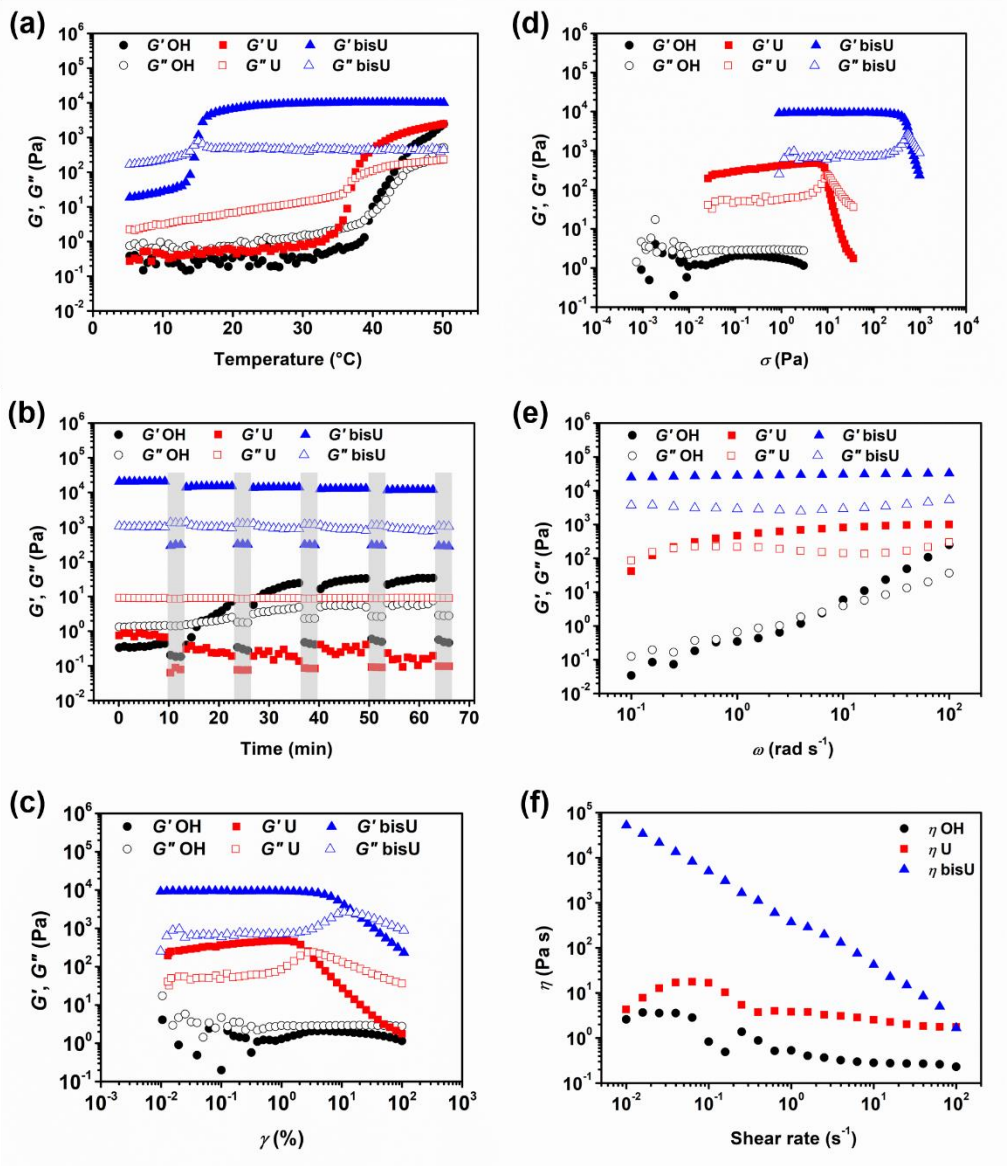

Figure 2.4. Rheometric experiments for 8k-iPr 25 wt% polymer hydrogels at 25 °C

(a) Temperature-ramp experiments conducted between 5-50 °C at a heating rate of 2 °C min^{-1}, with γ = 1% and ω = 1 Hz (6 rad s^{-1}). (b) Cyclic step-strain experiments (ω = 1 Hz). Strain amplitude alternated between 1% (white regions) and 100% (shaded regions). (c) Strain amplitude sweeps conducted at ω = 1 Hz. Yield strain was reported as the onset of *G'* decrease. (d) Stress amplitude sweeps derived from the strain-sweep experiments, conducted at ω = 1 Hz. Static yield stress (σ_y) was reported as the onset of *G'* decrease. For 8k-iPr-U, σ_y = 7.58 Pa, while for 8k-iPr-bisU, σ_y = 447 Pa. (e) Frequency amplitude sweeps performed at γ = 1%. (f) Shear rate sweep experiments to assess shear-thinning behavior, performed at 25 °C.

The dynamic oscillatory strain test for a 25 wt% 8k-iPr-OH solution showed an interesting phenomenon: the material was initially a fluid with $G'' > G'$, but following each cycle of 100% strain amplitude, the storage modulus increased and eventually crossed over the loss modulus (Figure 2.4 (b)). This strange measurement was attributed to the frequency dependence of the moduli for 8k-iPr-OH (Figure 2.4 (e)). Frequency-sweep measurements for each of the polymers allowed the estimation of average terminal relaxation time, τ, defined as the inverse of the radial frequency ω at the point of modulus crossover.[85,86] For 8k-iPr-OH, τ = 0.147 s, while for 8k-iPr-U τ = 4.51 s, and for 8k-iPr-bisU there was no modulus crossover in the tested frequency range. If the mechanism of stress relaxation is assumed to be disruption of bridging interactions between micelles or disruption of individual micelle structure, then this trend is logical. Because 8k-iPr-OH was not hydrophobic enough to form self-supporting hydrogels at 25 wt% and 25 °C, the exchange dynamics between chain-ends in micelle cores and water-solvated chain-ends was fast. The introduction of hydrophobic, hydrogen-bonding groups slowed the exchange dynamics for 8k-iPr-U, resulting in a longer relaxation time, while for 8k-iPr-bisU the exchange dynamics were too slow to be measured. The frequency-sweep measurements reflected the physical nature of each solution or gel: 8k-iPr-OH was a free-flowing liquid, 8k-iPr-U was a viscous solution, and 8k-iPr-bisU was a free-standing hydrogel. The angular frequency for the cyclic strain measurements was 6 rad s^{-1} (1 Hz), which was near the fluidlike-solidlike transition observed in the frequency-sweep test for 8k-iPr-OH. Oscillatory strain sweep tests were conducted for 25 wt% solutions/gels of all polymers, in which solutions/gels were subjected to increasing oscillatory strain amplitudes (0.01 to 100%) at a fixed angular frequency of 6 rad s^{-1} or 1 Hz (Figure 2.4 (c)). From this data, plots of G' and G'' against oscillatory stress (σ) were made (Figure 2.4 (d)). These plots were used to determine the static yield stress (σ_y) for each gel, or the minimum amount of pressure needed for

the gel to yield and to begin flowing, a crucial factor for extrusion-based applications. The 8k-iPr-OH solution was an unstructured fluid, and therefore did not possess a measurable yield stress. Under the conditions of the test, 8k-iPr-U was a weak gel, with a yield stress of σ_y = 7.58 Pa. As expected, the 8k-iPr-bisU gel had the highest yield stress of σ_y = 447 Pa. This yield stress was more than 5 times the value for a 20 wt% gel based on Pluronic F127,[29] but several orders of magnitude less than a similar bis-urea-containing, PEO-based gel.[37] While the F127 gel exhibited poor mechanical stability, the PEO-based gel was both mechanically robust and extrudable from a 29-gauge syringe needle. 8k-iPr-bisU gels therefore had a high enough yield stress to maintain structural integrity in the absence of applied pressure, but a low enough yield stress that they could be easily extruded from a nozzle.

2.3.2 *Differential Scanning Calorimetry*

While rheology and phase diagrams clearly demonstrated that the presence of the urea and bis-urea end-groups affected the viscoelastic behavior of the hydrogels, we turned to other techniques to further probe the assembly of the hydrogen-bonding assemblies. Urea-based assemblies are known to form anisotropic crystalline domains which can be represented by a melting transition in a DSC thermogram at temperatures above 170 °C.[37,80] As shown in Figure 2.5 (b), 8k-iPr-bisU exhibited a melting exotherm that suggested that the bis-ureas formed hard domains within the hydrogel assemblies.

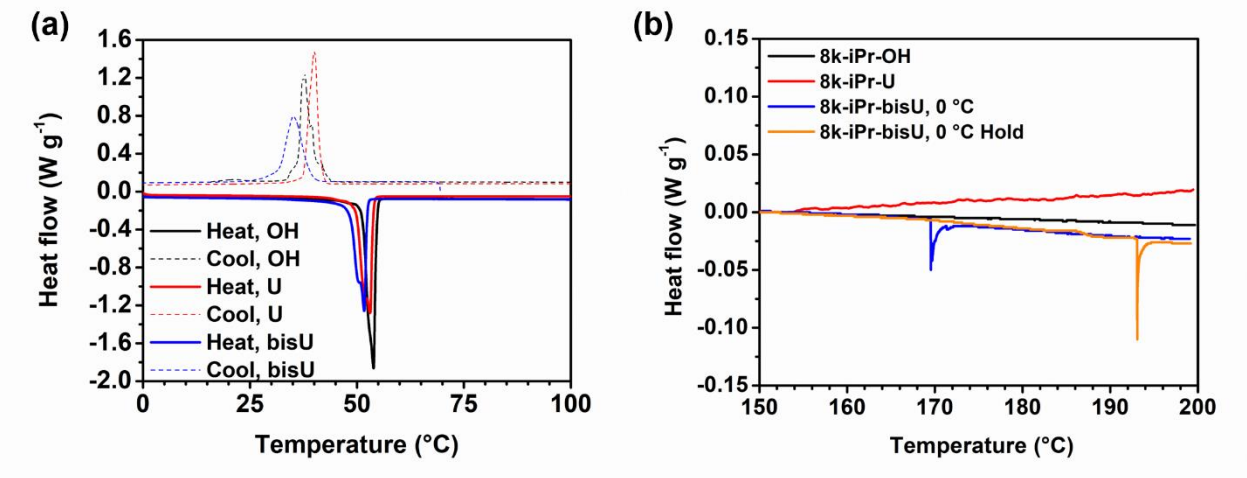

Figure 2.5. DSC thermograms for 8k-iPr polymers in the solid state
(a) Heating and cooling traces between 0-100 °C, showing slight differences in the peak position and width of the PEO melting and crystallization endo- and exotherms. (b) Heating traces between 150-200 °C. The bis-urea crystalline domains melted at 170 or 193 °C, depending on processing conditions.

Replicate measurements demonstrated that the melting transition occurred closer to 170 °C when the sample was cooled to 0 °C with no additional equilibration time, and closer to 193 °C when the sample was equilibrated for 90 min at 0 °C (Table 2.2). This difference in melting transition may reflect differences in the crystalline packing of the asymmetric bis-urea.[76,84,87,88] The single urea chain-ends of 8k-iPr-U did not exhibit a melting transition, which suggested that the ureas were not strongly associating into crystalline domains. We, and others, have previously reported glass transition temperatures for poly(alkyl glycidyl ether)s that range from −70 to −60 °C.[89–92] However, we did not observe a measurable glass transition in this temperature range. 8k-iPr-OH, 8k-iPr-U, and 8k-iPr-bisU exhibited PEO melting and crystallization transitions at 50–54 °C and 35–40 °C, respectively. Overall, the DSC data demonstrated phase separation of the urea end-groups only in 8k-iPr-bisU, which was consistent with the SAXS data.

Table 2.2. Thermal transitions measured by DSC

Heating/cooling rate was 2 °C min^{-1} for all experiments. [a]No equilibration time at 0 °C. [b]Allowed to equilibrate at 0 °C for 90 min following initial heating/cooling cycle.

		Transition 1		**Transition 2**	
Polymer	**Range (°C)**	***T*** **(°C)**	**Δ*H*** **(J g^{-1})**	***T*** **(°C)**	**Δ*H*** **(J g^{-1})**
8k-iPr-OH	-90 ↔ 200	53.9	126	--	--
8k-iPr-U	0[a] ↔ 200	53.1	112	--	--
8k-iPr-bisU	0[a] ↔ 200	51.7	99.7	170	0.621
8k-iPr-bisU	0[b] ↔ 200	52.0	95.6	193	0.557

2.3.3 *Infrared Spectroscopy*

Thin-film and solution-phase IR spectroscopic experiments were performed to further probe the association of the hydrogen-bonding end-groups. Thin-film IR spectra of 8k-iPr-U and 8k-iPr-bisU exhibited peaks in the range of 1500–1800 cm^{-1} that corresponded to the carbonyl stretching frequencies (Figure 2.14). For both 8k-iPr-U and 8k-iPr-bisU, the chain-end ester carbonyl stretching mode was present at 1751 cm^{-1}. More complex amide I, amide II, and aromatic carbon–carbon stretching vibrations appeared between 1500–1700 cm^{-1}. The amide I mode (carbonyl stretch) appeared as a mixture of strongly hydrogen-bonded (1640 cm^{-1}) and weakly-hydrogen-bonded (1700 cm^{-1}) populations in the thin film. Unfortunately, these stretches were overlapped by the presence of a water bending mode at 1640–1650 cm^{-1}, which complicated the analysis. However, these peak assignments agree with previously reported IR spectra for similar urea motifs.[72,80,88,93,94]

To probe the association and dissociation of the urea groups, solution-phase variable-temperature IR (VT-IR) experiments were performed. In these experiments, 23 wt% gels of 8k-iPr-U and 8k-iPr-bisU were prepared in D_2O to observe the carbonyl stretching modes between 1600–1800 cm^{-1}. As previously noted, these ABA triblock copolymers exhibit a temperature response in which they undergo a reversible sol–gel transition in water above a critical temperature. In the "sol" state, the entire triblock copolymer is water soluble, whereas in the "gel" state, the PiPGE block is hydrophobic and drives the micellization of the polymers. Thus, we hypothesized that, as the PiPGE blocks transitioned from a solvated aqueous state to a hydrophobically collapsed micelle core, the chain-end ureas would transition from a partially-solvated state to a self-associated supramolecular array within the hydrophobic domain of the glycidyl ether blocks. The VT-IR spectra suggested that the association of the hydrogen-bonded ureas remained relatively constant with temperature, even as the polymer chains underwent nanoscale rearrangement. Baseline-corrected spectra of 8k-iPr-bisU in the range of 1615–1715 cm^{-1} (Figure 2.6 (b)) indicated a slight change to the peak-shape for the carbonyl stretching frequencies as temperature decreased from 50 to 5 °C. This subtle, if not minimal, change suggested that at low temperatures, when the PiPGE blocks were more water-soluble, the urea end-groups were still hydrogen-bonded. The VT-IR tests therefore implied that the effects of water solvation on urea hydrogen-bonding in this system were minimal, and that these interactions persisted despite the solubility changes in the polymer.

We also observed that IR spectroscopy could be used to track the assembly/disassembly of the PiPGE chains. The peak at approximately 1348 cm^{-1} underwent measurable changes in intensity with varying temperature, increasing in area continuously as temperature decreased from 50 to 5 °C (Figure 2.6 (a)). This peak likely corresponded to a C–H bending mode of the *gem*-

dimethyl moiety in the PiPGE blocks. As these glycidyl ether blocks underwent hydrophobic collapse at higher temperatures, their effective concentration in D_2O decreased and their rotational freedom was restricted. As a result, CH_3 bending modes decreased in intensity. Conversely, disassembly of micelles upon cooling and subsequent solvation of the glycidyl ether blocks resulted in an *increase* in intensity for the peak at 1348 cm^{-1}. While these changes in the IR spectra are not directly related to the urea hydrogen-bonding motifs, they nevertheless reveal a useful protocol to track the self-assembly and disassembly of polymer chains with respect to temperature. In future experiments, deuteration of the isopropyl groups might be an easier way to track these bending modes in IR spectra.

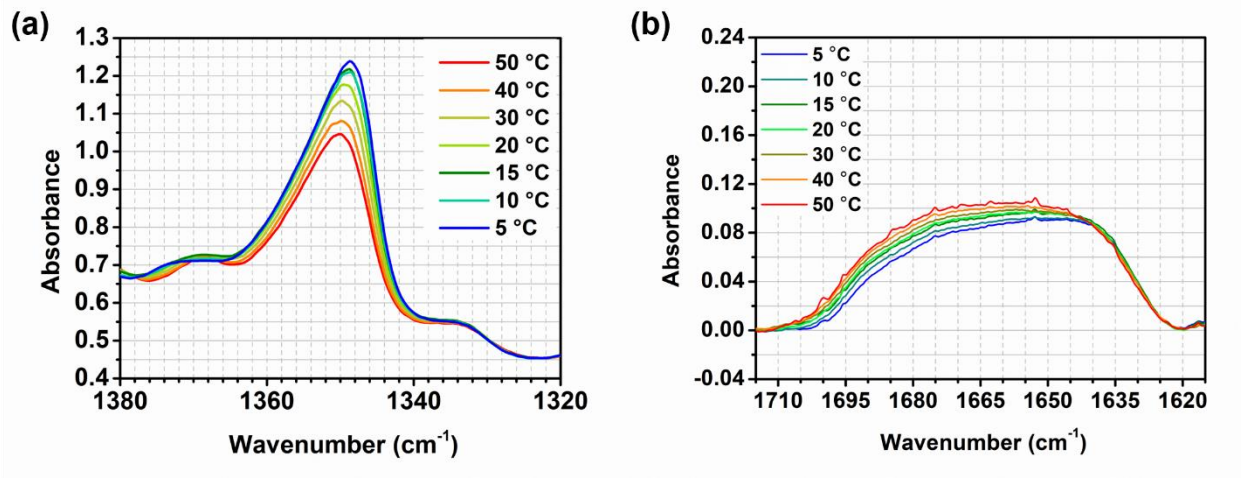

Figure 2.6. VT-IR spectra of 8k-iPr-bisU 23 wt% in D_2O

(a) Overlaid spectra of 8k-iPr-bisU between 1380-1320 cm^{-1}, showing continuous changes in the *gem*-dimethyl (1348 cm^{-1}) peak intensity with increasing/decreasing temperature. (b) Overlaid, baseline-shifted spectra of 8k-iPr-bisU between 1715-1615 cm^{-1}, showing minimal changes in the distribution of carbonyl stretching modes with changing temperature.

2.3.4 *Small-Angle X-ray Scattering (SAXS)*

Small-angle X-ray scattering (SAXS) was used to characterize the morphology of the assembled polymers (Figure 2.7). Previously, SAXS has been used to characterize the morphology of hydrogen-bonding polymers in hydrogels, organogels, and in the solid state.[25,37,53,61,80,95–98] Each polymer was examined in both the hydrated state (at 25 wt% polymer concentration) and the dry state.

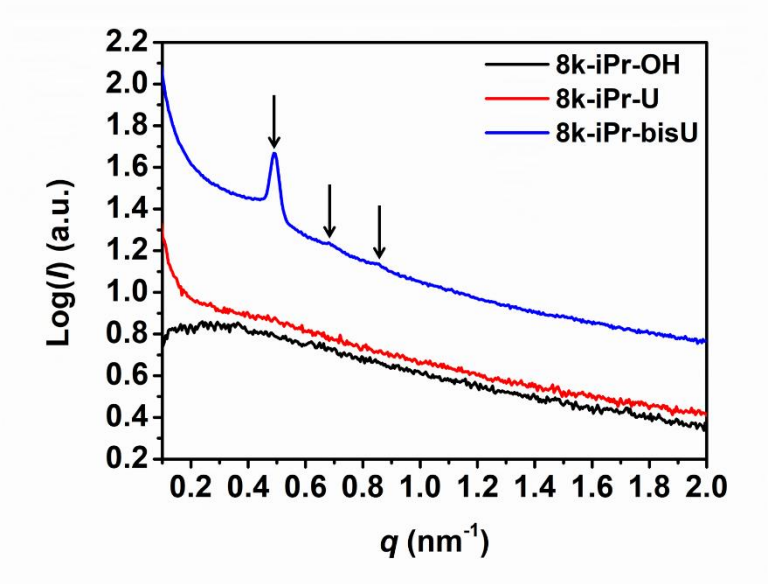

Figure 2.7. SAXS plots for 25 wt% 8k-iPr polymer hydrogels

Plots of intensity (*I*) *vs*. scattering vector (*q*) for each of the three polymer compositions in the hydrated state (25 wt%). The 8k-iPr-bisU formulation was the only polymer that showed correlation peaks (arrows), indicating a regular nanostructure.

For the base polymer 8k-iPr-OH, the volume fraction of the PiPGE blocks was insufficient to induce phase separation as demonstrated by the absence of any correlation peaks. The same was also true for 8k-iPr-U at this concentration, which is consistent with the data we have discussed thus far. On the other hand, 8k-iPr-bisU exhibited a well-defined, phase-separated morphology in

both the hydrated (25 wt%) and dry states. A sharp correlation peak at q = 0.494 nm^{-1} was observed, which corresponded to a characteristic spacing (periodicity, d) of 12.7 nm, according to the equation $d = 2\pi / q$. Smaller scattering peaks were also present at q = 0.694 and q = 0.856 nm^{-1}. These peaks corresponded to the peak-position ratio of 1, √2, and √3, which suggested a morphology of spherical micelles in a body-centered cubic (bcc) arrangement.[99,100] Indeed, for an ABA triblock copolymer with weight fractions A ~ 0.2 and B ~ 0.8, cubic morphology was expected.[101–103] This result suggested that 8k-iPr-bisU was the only polymer with a well-defined, structured morphology at 25 wt%.

2.4 CONCLUSIONS

In conclusion, end-groups capable of strong hydrogen bonding interactions can drastically influence both the nano- and macroscale properties of stimuli-responsive polymeric hydrogels. An ABA triblock copolymer of PEO ('B' block; DP = 182) and PiPGE ('A' blocks; DP = 8), which could not form hydrogels at room temperature, could be transformed into a gel when its end-groups were changed to aryl bis-ureas. As expected, bis-urea end-groups self-associated more strongly than monourea end-groups, resulting in more dramatic changes at the molecular and macroscopic levels. The changes in viscoelastic behavior induced by bis-urea motifs were the result of both the hydrophobicity of the two phenyl groups, as well as the strong hydrogen-bonding between ureas. The effects of hydrophobicity and hydrogen-bonding were complementary: additional hydrophobicity led to polymer chains that micellized more readily, which in turn allowed for higher local concentrations of ureas in the micelle core. The ureas localized within these hydrophobic domains formed hydrogen-bonding supramolecular assemblies.

The introduction of bis-urea motifs also altered the processing conditions required for the gels. 8k-iPr-OH solutions were free-flowing and easy to manipulate at low temperatures, while 8k-iPr-bisU gels were extremely viscous at low temperatures. DSC and SAXS experiments suggested that these changes in the bulk material were due to nanoscale organization and microphase separation of the urea groups. Overall, the data demonstrate that end-group composition is a profoundly important parameter in block copolymer self-assembly. In future work, changing the composition of the 'A' blocks – for example, to statistical copolymers of isopropyl glycidyl and ethyl glycidyl ether – could help to optimize the thermoresponsive properties of urea-containing polymers. We anticipate that alternative polymer compositions and hydrogen-bonding end-groups will result in materials with precisely tunable mechanical properties and stimuli-responsive behaviors. With further optimization, the soft gels could find applications in shape-morphing, 3D-printed materials and tissue engineering scaffolds.

2.5 EXPERIMENTAL

2.5.1 *Materials*

All solvents and reagents were purchased from Sigma-Aldrich, Fisher Scientific, or TCI America and used as received, unless noted otherwise. Dichloromethane (CH_2Cl_2; HPLC grade) and tetrahydrofuran (THF; Optima) were dried with neutral alumina using a Pure Process Technology Glass Contour solvent purification system and were dispensed under argon. Diethyl ether (Et_2O; Fisher, Certified ACS, Anhydrous, BHT stabilized, 99.9%) was dried over anhydrous magnesium sulfate (Fisher, Certified Powder) immediately prior to use. Acetonitrile (CH_3CN) was purchased from Fisher (HPLC Grade, 99.9%).

2.5.2 *Instrumentation*

All NMR spectra were collected using a Bruker AV 500 MHz spectrometer equipped with a double resonance broadband (BBI) probe and Oxford narrow bore cryomagnet, with 24 scans and 5 or 10 s pulse delay times (d1) at 298 K. Thin-film IR spectra were collected on a Bruker Vector 33 FT-IR spectrophotometer using KBr salt plates. Variable-temperature IR experiments were performed using a JASCO Model FT/IR-4100A spectrophotometer at 1 cm^{-1} resolution, with a sealed brass sample cell. The cell temperature was controlled using inlet/outlet tubing connected to an ethylene glycol-based heat exchanger. The sample chamber was purged with N_2 to remove CO_2 and traces of water vapor. Sol–gels were prepared at 23 wt% in D_2O to better observe urea stretching and bending modes between 1500–1800 cm^{-1}. Heating/cooling rates were maintained at approximately 0.5 °C min^{-1} to ensure complete equilibration and self-assembly. Gel permeation chromatography (GPC) was performed using a Waters chromatograph (Waters 1525 Binary HPLC Pump with in-line degasser) equipped with two 10 μm Malvern columns (300 mm × 7.8 mm) connected in series with increasing pore size (1,000–10,000 Å), using chloroform ($CHCl_3$; Optima, 0.1% v/v triethylamine, 1.0 mL min^{-1} flow rate) as the eluent, and calibrated with poly(ethylene oxide) standards (Fluka Analytical, 400 to 40,000 g mol^{-1}). The relative molecular weights were measured using a refractive index detector (Waters 2414). All rheological measurements were performed on a TA Instruments Discovery HR-2 hybrid rheometer equipped with Peltier temperature control accessory. Each rheological experiment was performed with a 20 mm flat-plate geometry, except for cyclic oscillatory strain experiments, which utilized a 40 mm cone-and-plate geometry and solvent trap. All tests were performed in duplicate to ensure reproducibility. Differential scanning calorimetry (DSC) was performed using a TA Instruments DSC 250

calorimeter equipped with a TA RCS90 cooling system, using Tzero standard aluminum pans (TA Instruments) and calibrated with an indium standard. The heating and cooling rate for all samples was 2 °C min^{-1}, except for the initial heating cycle, which was run at a rate of 10 °C min^{-1}. SAXS measurements were performed using a Xeuss 2.0 laboratory beamline (Xenocs Inc.) with an X-ray wavelength of 1.54 Å and a sample-to-detector distance of 2.5 m. Diffraction images were recorded on a Pilatus 1M Detector (Dectris Inc.) with an exposure time of 2 h, then analyzed using the Nika software package.[104] Measurements were collected in both the hydrated (25 wt%) and dry states for each polymer composition.

2.5.3 *Monomer Distillation*

Isopropyl glycidyl ether (iPGE; Aldrich 98%) was dried over CaH_2 (Fisher, Laboratory Grade) for 24 h under N_2 atmosphere. Next, iPGE was distilled under reduced pressure into a flask containing ~1 mL butyl magnesium chloride (dried 2.0 M THF solution, Aldrich). Finally, iPGE was distilled into a clean, dry flask containing activated 4 Å molecular sieves (Fisher, Grade 514, 8–12 mesh beads). Immediately prior to use, distilled iPGE was degassed using three full freeze–pump–thaw cycles.

2.5.4 *Potassium Naphthalenide Preparation*

Potassium naphthalenide was prepared as a 1.0 M solution in THF. Typical preparation proceeded as follows: naphthalene (2.57 g, Fisher Certified Crystalline) was added to an oven-dried 100 mL Schlenk flask, then dissolved in 20 mL anhydrous THF under N_2 atmosphere. Potassium (0.783 g, Aldrich 99.5%) was transferred from mineral oil to hexanes, then added

quickly to the dissolved naphthalene. The resulting dark green solution was stirred under N_2 atmosphere for 6 h.

2.5.5 *Synthesis of 8k-iPr-OH Polymer*

An oven-dried, 5-neck reactor flask was charged with PEO (1.0 eq / 20.2 g, Sigma BioUltra, M_n = 8,000 g mol^{-1}) and a glass-coated stir bar. The flask was evacuated and purged with argon three times, and PEO was then dried under reduced pressure at 40 °C for 24 h. Dried PEO was dissolved in 200 mL anhydrous THF (final concentration 10% w/v), then warmed to 50 °C under argon atmosphere. Potassium naphthalenide 1.0 M THF solution (7 mL) was slowly added *via* syringe to the dissolved PEO until a yellow-green color persisted. Degassed iPGE (21 eq / 6.29 g) was added quickly *via* syringe. After 48 h of polymerization at 50 °C under argon atmosphere, the reaction was quenched by addition of degassed 1% (v/v) acetic acid:MeOH (5 mL). The reaction mixture was concentrated *in vacuo,* then precipitated in large excess (800 mL) of anhydrous Et_2O. The slurry was centrifuged at 4400 rpm, the supernatant was decanted, and the precipitated polymer was rinsed three times with fresh Et_2O. Recovered white solid was dried in air at RT for 24 h, then dried under reduced pressure at 40 °C. To remove traces of potassium ion, dried polymer was reconstituted in 150 mL CH_2Cl_2, then stirred with 1 g Dowex 50WX8 cation exchange resin (Sigma-Aldrich, hydrogen form, 100-200 mesh) for 30 min. Following filtration, concentration, and a final precipitation from Et_2O, polymer was dried under reduced pressure at 50 °C, then stored in an amber bottle at 5 °C (21.6 g, 82% yield). Degree of polymerization (DP) for the poly(isopropyl glycidyl ether) blocks was estimated by ^{1}H NMR spectroscopy to be DP = 8 (16 total, approximately 1,900 g mol^{-1}) as described in

section 2.5.10. GPC indicated narrow dispersity, Đ = 1.10, suggesting little to no chain transfer or termination, in agreement with the living nature of the polymerization.

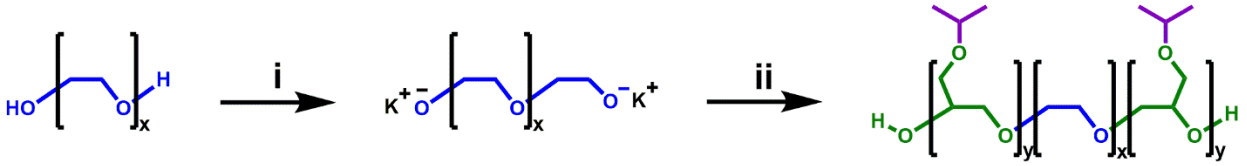

Figure 2.8. Anionic ring-opening polymerization of iPGE from PEO

(i) Potassium naphthalenide (1.0 M in THF), 50 °C, THF. (ii) (1) iPGE, 50 °C, 48 h. (2) 1% v/v AcOH:MeOH, 50 °C, 10 min.

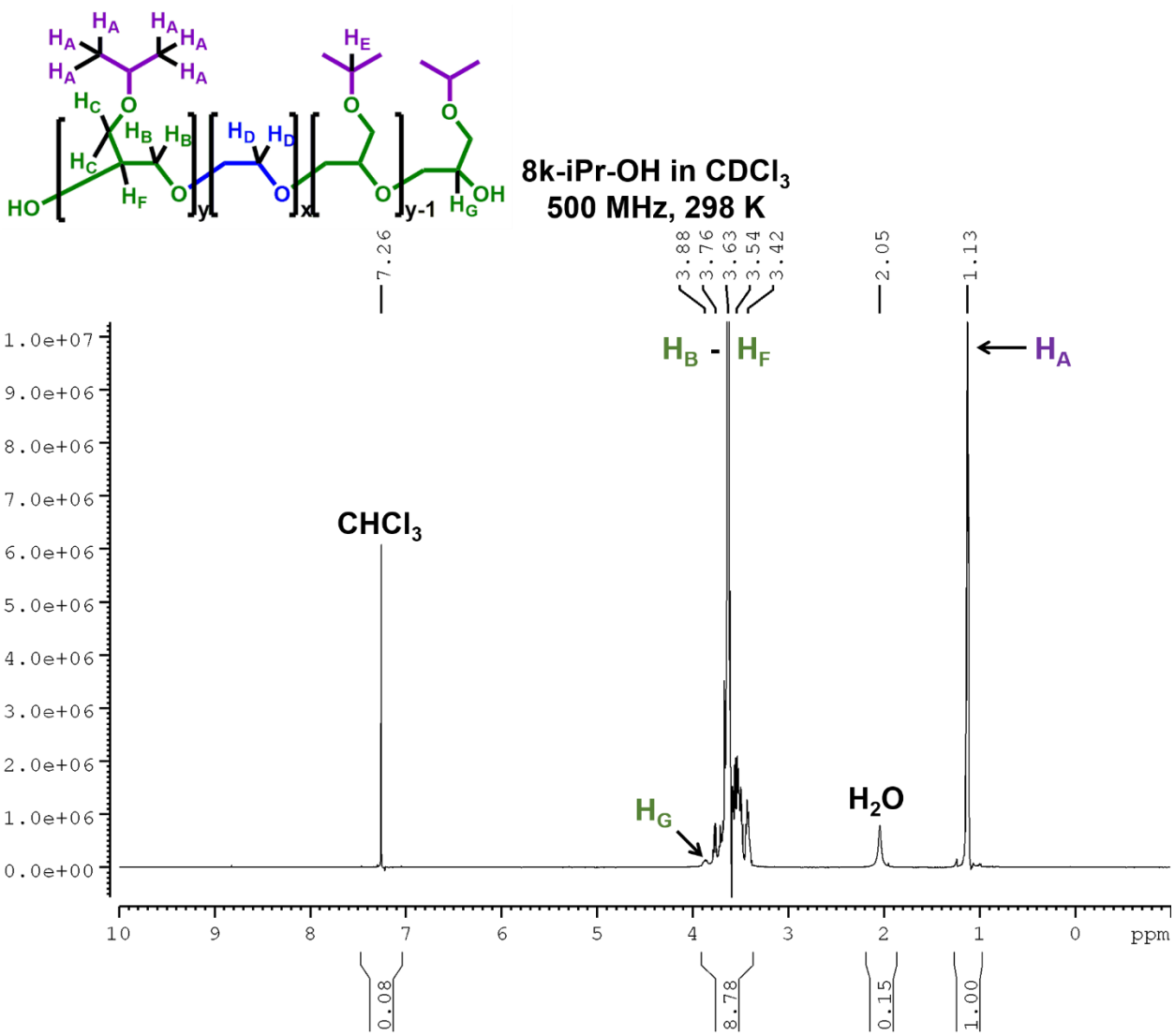

Figure 2.9. ^{1}H NMR spectrum of 8k-iPr-OH in $CDCl_3$
500 MHz frequency / T = 298 K.

2.5.6 *Steglich Esterification with Boc-Protected Glycine*

8k-iPr-OH and *boc*-protected glycine (*Boc*-gly; 25 eq, Aldrich, ≥99%) were dried under reduced pressure at 50 °C for 24 h. Dried *boc*-gly was dissolved in anhydrous CH_2Cl_2 under N_2 atmosphere, while dried 8k-iPr-OH was dissolved in CH_2Cl_2 in a separate flask. 4-Dimethylaminopyridine (DMAP; 0.25 eq, Aldrich ReagentPlus, ≥ 99%) was dissolved in a

minimal amount of CH_2Cl_2, then mixed with dissolved polymer. The 8k-iPr-OH / DMAP solution was added dropwise to dissolved *boc*-gly. Dicyclohexylcarbodiimide (DCC; 25 eq, Aldrich 99%) was melted for easy handling, then dissolved in anhydrous CH_2Cl_2 and added dropwise to the rest of the reaction mixture. The final reaction mixture (approximately 10% w/v polymer) was brought to reflux (55 °C hot plate setting) and stirred under N_2 for 24 h. The reaction mixture was cooled and vacuum-filtered. Solvent was removed *in vacuo*, then residue was reconstituted in CH_3CN (Fisher, HPLC Grade, 99.9%) and stirred for 15 min. The solution was centrifuged, resulting in a small amount of settled white solid. Supernatant was filtered through a fritted funnel (medium porosity), and transparent filtrate was concentrated *in vacuo*. The residue was stirred in excess Et_2O, centrifuged, and rinsed twice with fresh Et_2O. The *boc*-functionalized polymer, 8k-iPr-*boc*, was isolated as an off-white solid and dried in air at RT for 24 h.

2.5.7 *TFA-Mediated Boc Cleavage*

The 8k-iPr-*boc* polymer was stirred in a 1:1 (v/v) mixture of CH_2Cl_2 and trifluoroacetic acid (TFA; Sigma-Aldrich ReagentPlus, 99%) for 18 h at RT. Solvent was removed *in vacuo*, concentrate was reconstituted in fresh CH_2Cl_2, and this process was repeated 3 times. The resulting residue was precipitated in excess Et_2O, centrifuged, then rinsed once with fresh Et_2O. The recovered off-white solid was dried under reduced pressure at 40 °C to afford the amine-functionalized polymer, 8k-iPr-NH_2.

2.5.8 *Synthesis of 8k-iPr-U Polymer*

8k-iPr-NH_2 (1.0 eq) was dried under reduced pressure at 40 °C prior to synthesis. *Para*-tolyl isocyanate (10 eq, Aldrich, 99%) was removed from cold storage and brought to RT in a sealed bottle. The isocyanate was dissolved in anhydrous CH_2Cl_2 in a flask containing activated 4 Å molecular sieves. Dried 8k-iPr-NH_2 was dissolved in CH_2Cl_2 along with triethylamine (NEt_3; 2.5 eq, TCI America, > 99%, distilled from CaH_2). Dissolved 8k-iPr-NH_2 was added dropwise to the isocyanate, and the reaction mixture was stirred under N_2 atmosphere for 18 h. Next, the reaction mixture was vacuum-filtered. The slightly turbid, golden filtrate was centrifuged at 4400 rpm. The supernatant was syringe-filtered (0.7 μm glass microfiber, Whatman) and solvent was removed *in vacuo*. The concentrated residue was stirred in excess Et_2O, centrifuged, then rinsed twice with fresh Et_2O and dried in air at RT for 24 h to afford 8k-iPr-U. Degree of functionalization (f_n) was estimated by ^{1}H NMR spectroscopy as described in section 2.5.11. f_n = 82-91%.

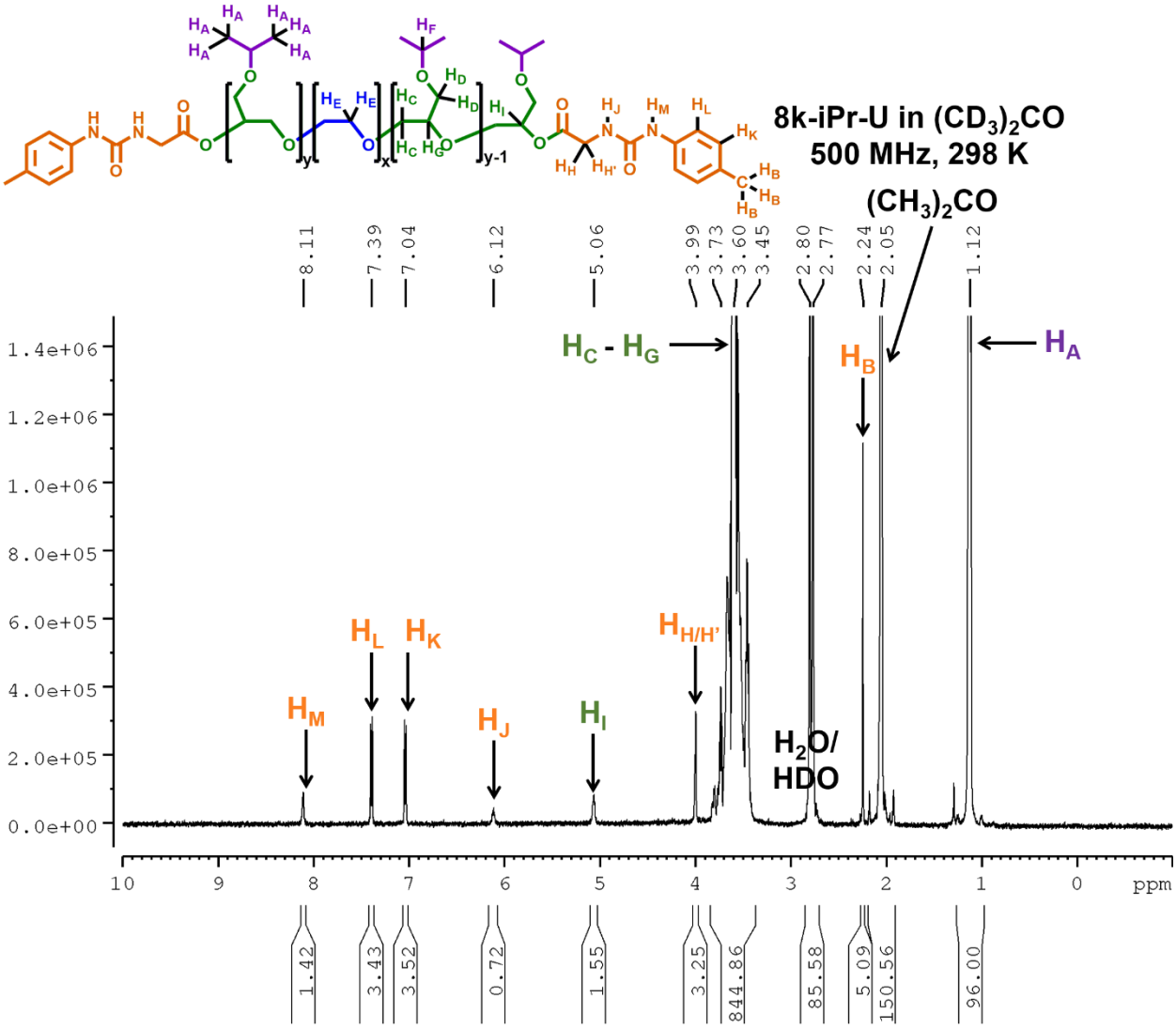

Figure 2.10. ^{1}H NMR spectrum of 8k-iPr-U in $(CD_3)_2CO$

500 MHz frequency / *T* = 298 K

2.5.9 *Synthesis of 8k-iPr-bisU Polymer*

8k-iPr-NH_2 (1.0 eq) was dried under reduced pressure at 40 °C prior to synthesis. Toluene-2,4-diisocyanate (100 eq, Aldrich 95%, 4% as 2,6-isomer) was dissolved in anhydrous CH_2Cl_2 in a flask containing activated 4 Å molecular sieves. Dried 8k-iPr-NH_2 was dissolved in CH_2Cl_2 along with NEt_3 (2.5 eq, TCI America, > 99%, distilled from CaH_2.) Dissolved 8k-iPr-NH_2 was added dropwise to the diisocyanate over 1 h. Reaction mixture was stirred under N_2 atmosphere for 16 h, then vacuum-filtered. The slightly turbid, golden filtrate was syringe-filtered (0.7 μm glass microfiber), then concentrated *in vacuo*. The residue was stirred in a large excess of anhydrous Et_2O, centrifuged, then rinsed three times with fresh Et_2O. Recovered polymer was dried under reduced pressure at RT for 3 h. Aniline (100 eq, Fisher, Certified ACS, 99.9%) was dried over activated 4 Å molecular sieves for 2 h, then dissolved in dry CH_2Cl_2 in a flask containing molecular sieves. The partially dried polymer was reconstituted in dry CH_2Cl_2, then added dropwise to the aniline over 1 h. The reaction mixture was stirred under N_2 atmosphere for 21 h, then vacuum-filtered and centrifuged. The supernatant was syringe-filtered, yielding a clear, golden solution which was subsequently concentrated. The residue was stirred in a large excess of Et_2O, centrifuged, and rinsed three times with fresh Et_2O. Recovered polymer was dried under reduced pressure at 30 °C to afford 8k-iPr-bisU. Degree of functionalization (f_n) was estimated by ^{1}H NMR spectroscopy as described in section 2.5.11. f_n = 90-93%.

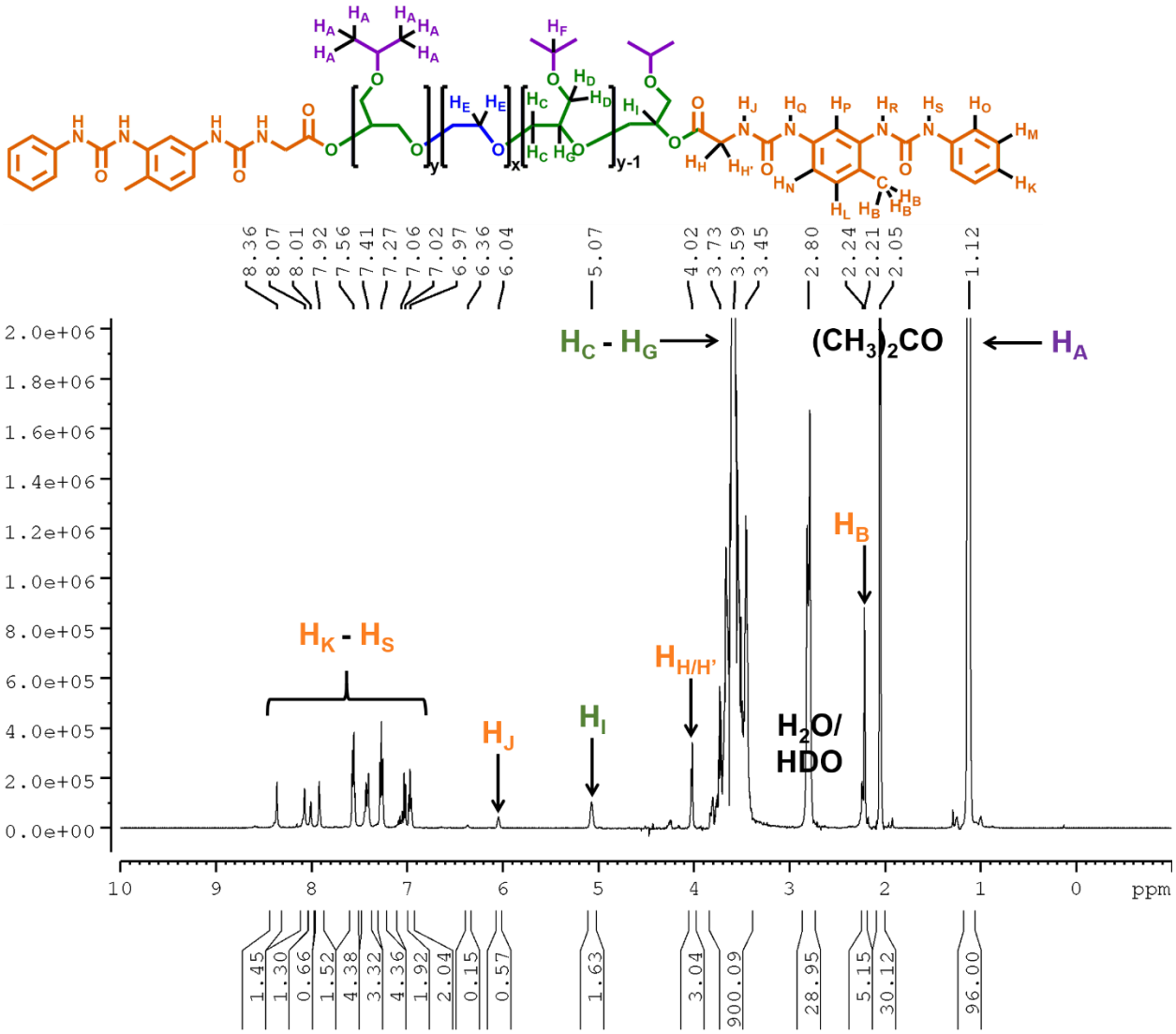

Figure 2.11. ^{1}H NMR spectrum of 8k-iPr-bisU in $(CD_3)_2CO$

500 MHz frequency / T = 298 K

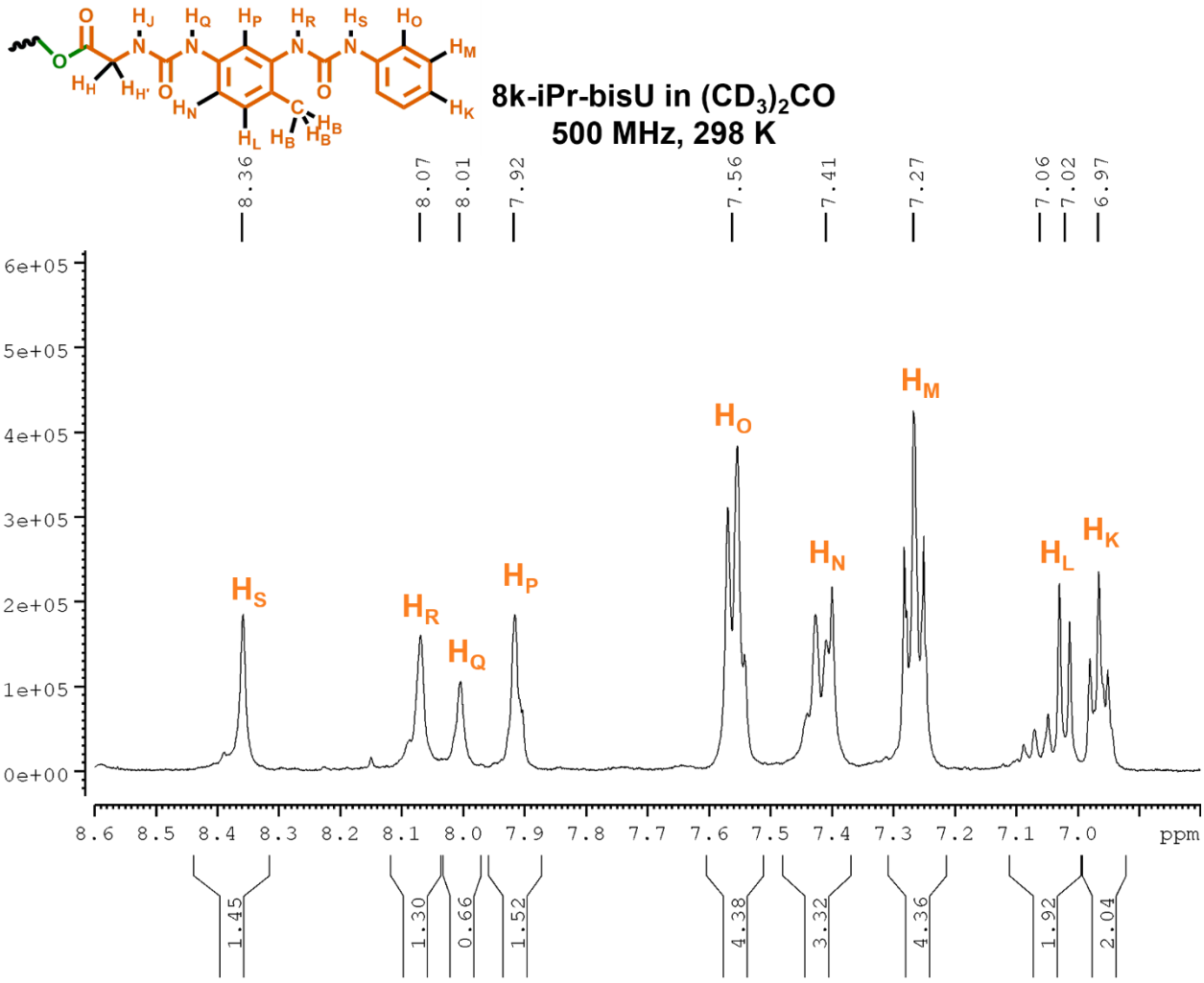

Figure 2.12. ^{1}H NMR spectrum of 8k-iPr-bisU in $(CD_3)_2CO$ between δ 6.8-8.6 ppm
500 MHz frequency / T = 298 K

2.5.10 *Estimation of Degree of Polymerization (DP) by ^{1}H NMR Spectroscopy*

To complement the estimates of M_n made *via* GPC, degree of polymerization (and hence, M_n) was calculated using ^{1}H NMR. A sample calculation is as follows: Let 'x' equal the integration per proton for iPGE. Let 'y' equal the integration per proton for PEO. Using Figure 2.9 as a sample spectrum, this gives the equations $6x = 1$ for the 6 protons that

contribute to the isopropyl resonance at 1.1 ppm, and *4y + 6x = 8.78* for the 4 PEO protons and 6 iPGE protons that contribute to the polyether backbone resonances between 3.3-3.9 ppm. Solving these equations yields:

$$x = \frac{1}{6} \quad y \sim 1.95$$

This gives the PEO:PiPGE molar ratio:

$$\frac{y}{x} \sim 11.7$$

With a known M_n for PEO of 8.0 kg mol^{-1} and the monomer mass of ethylene oxide (44.05 g mol^{-1}), the average number of PEO repeat units is:

$$\frac{8000}{44.05} \sim 182$$

Dividing this by the ratio of PEO to PiPGE, we obtain the total repeat units of iPGE:

$$\frac{182}{11.7} \sim 15.6$$

Or 7.8 repeat units per block, rounded up to 8.

2.5.11 *Estimation of Degree of Functionalization (f_n) for 8k-iPr-U and 8k-iPr-bisU*

The efficiency of DCC-mediated esterification was estimated by integrating the polymer chain-end methyne proton (δ 4.9 ppm, DMSO-d_6) and the *boc* methyl protons (δ 1.4 ppm, DMSO-d_6) against the iPGE methyl protons (δ 1.1 ppm, DMSO-d_6). Using the known DP (8) of the PiPGE blocks, the iPGE methyl resonance was calibrated to:

$$8 \times 2 \times 6 = 96$$

This resulted in integrations of 1.8 for the methyne proton and 16.7 for the *boc* methyl protons (spectra not shown). Division by the theoretical integrations of 2 and 18 gave estimates of f_n ~ 90% and 93%, respectively. TFA-catalyzed deprotection was quantitative as indicated by the complete disappearance of the *boc* methyl protons. To estimate degree of functionalization for subsequent coupling with *p*-tolyl isocyanate or tolylene-2,4-diisocyanate, the aromatic protons (δ 6.9-7.6 ppm, $(CD_3)_2CO$) were integrated against the chain-end methyne proton (δ 5.1 ppm, $(CD_3)_2CO$). Division by the theoretical values for the integrations, followed by multiplying the yield of the esterification and deprotection steps, gave f_n estimates of f_n ~ 82-91% for 8k-iPr-U and 90-93% for 8k-iPr-bisU. In the case of 8k-iPr-U and 8k-iPr-bisU, the aryl methyl protons (δ 2.2-2.3 ppm, $(CD_3)_2CO$) were also used to estimate f_n.

2.5.12 *Hydrogel Preparation for Rheometric Experiments*

All polymer sol-gels were prepared using a 'sandwich' technique: Approximately half of the desired mass of water was added to a small vial, followed by the desired mass of polymer and finally the remaining mass of water. All solutions were incubated at 0-5 °C for 72 h prior to temperature-ramp measurements, with daily stirring. Using the temperature-ramp data, a solution was defined as any region where the storage modulus (G') was less than the loss modulus (G''). Conversely, a gel was defined as any region where $G' > G''$. Based on qualitative observations, a viscous solution was defined as any region where $G' < G''$ and $G'' \geq 10$ Pa. The gelation temperature (T_{gel}) was defined as the point of modulus crossover, where G' becomes greater than G''.

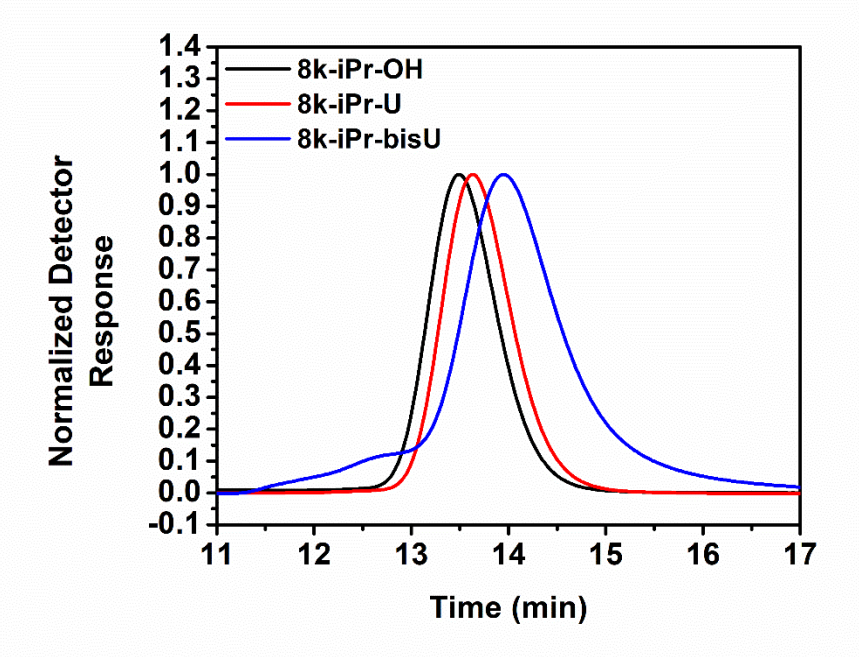

Figure 2.13. Normalized GPC traces for 8k-iPr polymers

Polymers were eluted in $CHCl_3$ (stabilized with 0.1% v/v triethylamine).

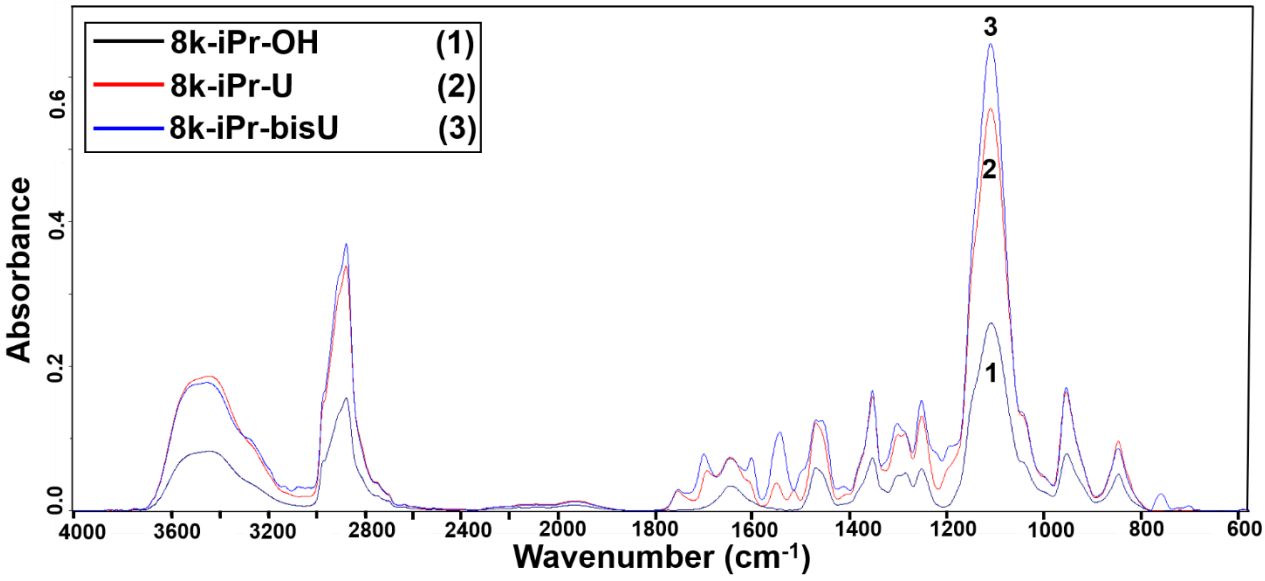

Figure 2.14. Thin-film IR spectra of 8k-iPr polymers

8k-iPr-OH (black), 8k-iPr-U (red), and 8k-iPr-bisU (blue) were dried from CH_2Cl_2 on KBr salt plates.

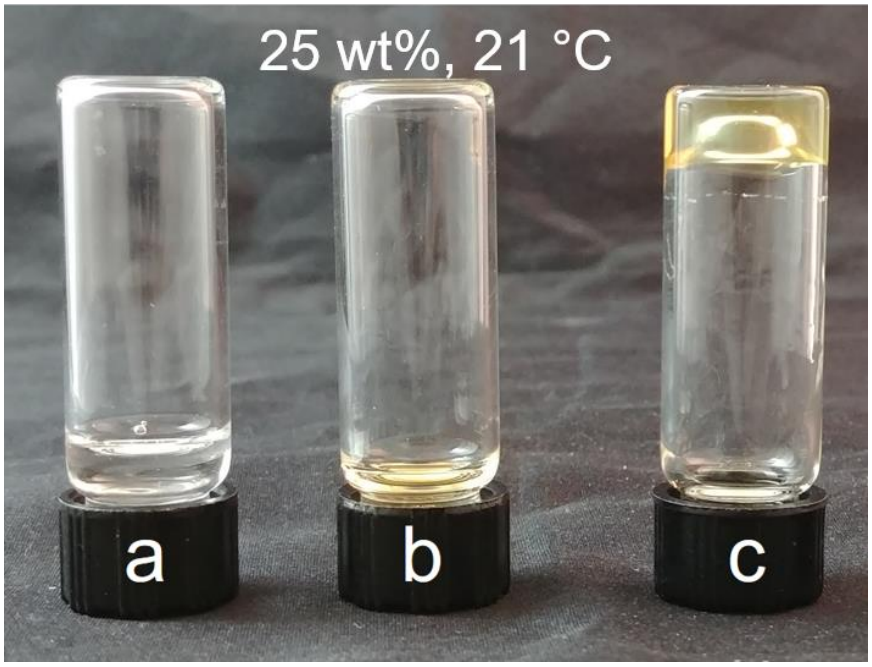

Figure 2.15. Photos of 25 wt% 8k-iPr polymer hydrogels
(a) 8k-iPr-OH. (b) 8k-iPr-U. (c) 8k-iPr-bisU. All gels were equilibrated at 21 °C.

Table 2.3. Melting points of synthesized small-molecule ureas

Molecule	**Melting Point (°C)**
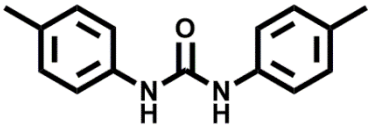	194-196
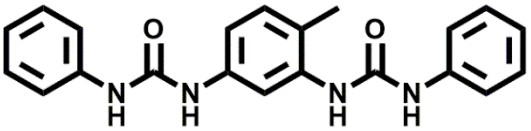	261-263
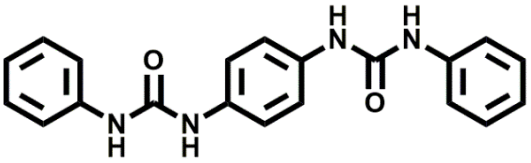	>400 (decomposes)

2.6 ACKNOWLEDGEMENTS

Reprinted (adapted) with permission from Shafranek, R.T.; Leger, J.D.; Zhang, S.; Khalil, M.; Gu, X.; Nelson, A. Sticky Ends in a Self-Assembling ABA Triblock Copolymer: The Role of Ureas in Stimuli-Responsive Hydrogels. *Mol. Syst. Des. Eng.* **2019**, *4*, 91-102.

We gratefully acknowledge support of this research by the NSF CAREER Grant 1752972. We also acknowledge Dylan G. Karis, Christopher R. Fellin, and Robert J. Ono for synthetic guidance.

2.7 REFERENCES

(1) Antoine, E. E.; Vlachos, P. P.; Rylander, M. N. Review of Collagen I Hydrogels for Bioengineered Tissue Microenvironments: Characterization of Mechanics, Structure, and Transport. *Tissue Eng. Part B Rev.* **2014**, *20* (6), 683–696.

(2) Voorhaar, L.; Hoogenboom, R. Supramolecular Polymer Networks: Hydrogels and Bulk Materials. *Chem. Soc. Rev.* **2016**, *45* (14), 4013–4031.

(3) Webber, M. J.; Appel, E. A.; Meijer, E. W.; Langer, R. Supramolecular Biomaterials. *Nat. Mater.* **2015**, *15* (1), 13–26.

(4) Park, M.; Harrison, C.; Chaikin, P. M.; Register, R. A.; Adamson, D. H. Block Copolymer Lithography: Periodic Arrays of ~10^11 Holes in 1 Square Centimeter. *Science (80-.).* **1997**, *276* (5317), 1401–1404.

(5) Förster, B. S.; Antonietti, M. Amphiphilic Block Copolymers in Structure-Controlled Nanomaterial Hybrids. *Adv. Mater.* **1998**, *10* (3), 195–217.

(6) Ruzette, A. V.; Leibler, L. Block Copolymers in Tomorrow's Plastics. *Nat. Mater.* **2005**, *4* (1), 19–31.

(7) Doerk, G. S.; Yager, K. G. Beyond Native Block Copolymer Morphologies. *Mol. Syst. Des. Eng.* **2017**, *2* (5), 518–538.

(8) Lutz, J.-F.; Ouchi, M.; Liu, D. R.; Mitsuo Sawamoto. Sequence-Controlled Polymers. *Science (80-.).* **2013**, *341* (6146), 1238149 (1-8).

(9) Lutz, J.-F.; Meyer, T.Y.; Ouchi, M.; Sawamoto, M. *Sequence-Controlled Polymers: Synthesis, Self-Assembly, and Properties.*; American Chemical Society: Washington, D.C., 2014.

(10) Ariga, K.; Aono, M. Nanoarchitectonics. *Jpn. J. Appl. Phys.* **2016**, *55* (1102A6), 1102A6

(1-7).

(11) Ariga, K.; Mori, T.; Li, J. Langmuir Nanoarchitectonics from Basic to Frontier. *Langmuir* **2018**.

(12) Wakayama, Y. On-Surface Molecular Nanoarchitectonics : From Self-Assembly to Directed Assembly. *Jpn. J. Appl. Phys.* **2016**, *55*, 1102AA (1-13).

(13) Kujawa, P.; Winnik, F. M. Materials Nanoarchitectonics: A Conspectus for Polymer Scientists. *Polym. Int.* **2014**, *63* (3), 377–380.

(14) Ariga, K.; Lee, M. V.; Mori, T.; Yu, X. Y.; Hill, J. P. Two-Dimensional Nanoarchitectonics Based on Self-Assembly. *Adv. Colloid Interface Sci.* **2010**, *154* (1–2), 20–29.

(15) Ariga, K.; Leong, D. T.; Mori, T. Nanoarchitectonics for Hybrid and Related Materials for Bio-Oriented Applications. *Adv. Funct. Mater.* **2018**, *28* (27), 1702905 (1-23).

(16) Ariga, K. Nanoarchitectonics: A Navigator from Materials to Life. *Mater. Chem. Front.* **2017**, *1* (2), 208–211.

(17) Stulz, E. Nanoarchitectonics with Porphyrin Functionalized DNA. *Acc. Chem. Res.* **2017**, *50* (4), 823–831.

(18) Cortez, M. L.; Lorenzo, A.; Marmisollé, W. A.; Von Bilderling, C.; Maza, E.; Pietrasanta, L.; Battaglini, F.; Ceolín, M.; Azzaroni, O. Highly-Organized Stacked Multilayers via Layer-by-Layer Assembly of Lipid-like Surfactants and Polyelectrolytes. Stratified Supramolecular Structures for (Bio)Electrochemical Nanoarchitectonics. *Soft Matter* **2018**, *14* (10), 1939–1952.

(19) Lorenzo, A.; Marmisollé, W. A.; Maza, E. M.; Ceolín, M.; Azzaroni, O. Electrochemical Nanoarchitectonics through Polyaminobenzylamine-Dodecyl Phosphate Complexes: Redox Activity and Mesoscopic Organization in Self-Assembled Nanofilms. *Phys. Chem. Chem. Phys.* **2018**, *20* (11), 7570–7578.

(20) Maza, E.; Von Bilderling, C.; Cortez, M. L.; Díaz, G.; Bianchi, M.; Pietrasanta, L. I.; Giussi, J. M.; Azzaroni, O. Layer-by-Layer Assembled Microgels Can Combine Conflicting Properties: Switchable Stiffness and Wettability without Affecting Permeability. *Langmuir* **2018**, *34* (12), 3711–3719.

(21) Kim, B.; Park, Y. D.; Min, K.; Lee, J. H.; Hwang, S. S.; Hong, S. M.; Kim, B. H.; Kim, S. O.; Koo, C. M. Electric Actuation of Nanostructured Thermoplastic Elastomer Gels with Ultralarge Electrostriction Coefficients. *Adv. Funct. Mater.* **2011**, *21*, 3242–3249.

(22) Sawada, H.; Yamanaka, M. Synthesis of a Bis-Urea Dimer and Its Effects on the Physical Properties of an Amphiphilic Tris-Urea Supramolecular Hydrogel. *Chem. - An Asian J.* **2018**, *13* (8), 929–933.

(23) Li, L.; Zhang, P.; Zhang, Z.; Lin, Q.; Wu, Y.; Cheng, A.; Lin, Y.; Thompson, C. M.; Smaldone, R. A.; Ke, C. Hierarchical Co-Assembly Enhanced Direct Ink Writing. *Angew. Chemie - Int. Ed.* **2018**, *57* (18), 5105–5109.

(24) Zhang, G.; Chen, Y.; Deng, Y.; Ngai, T.; Wang, C. Dynamic Supramolecular Hydrogels: Regulating Hydrogel Properties through Self-Complementary Quadruple Hydrogen Bonds

and Thermo-Switch. *ACS Macro Lett.* **2017**, *6* (7), 641–646.

(25) Yuan, H.; Xu, J.; Van Dam, E. P.; Giubertoni, G.; Rezus, Y. L. A.; Hammink, R.; Bakker, H. J.; Zhan, Y.; Rowan, A. E.; Xing, C.; et al. Strategies to Increase the Thermal Stability of Truly Biomimetic Hydrogels: Combining Hydrophobicity and Directed Hydrogen Bonding. *Macromolecules* **2017**, *50* (22), 9058–9065.

(26) Tsitsilianis, C. Responsive Reversible Hydrogels from Associative "Smart" Macromolecules. *Soft Matter* **2010**, *6*, 2372–2388.

(27) Topp, M. D. C.; Dijkstra, P. J.; Talsma, H.; Feijen, J. Thermosensitive Micelle-Forming Block Copolymers of Poly(Ethylene Glycol) and Poly(N-Isopropylacrylamide). *Macromolecules* **1997**, *30* (26), 8518–8520.

(28) Kim, M. S.; Hyun, H.; Seo, K. S.; Cho, Y. H.; Lee, J. W.; Lee, C. R.; Khang, G.; Lee, H. B. Preparation and Characterization of MPEG–PCL Diblock Copolymers with Thermo-Responsive Sol–Gel–Sol Phase Transition. *J. Polym. Sci. Part A Polym. Chem.* **2006**, *44* (18), 5413–5423.

(29) Zhang, M.; Vora, A.; Han, W.; Wojtecki, R. J.; Maune, H.; Le, A. B. A.; Thompson, L. E.; McClelland, G. M.; Ribet, F.; Engler, A. C.; et al. Dual-Responsive Hydrogels for Direct-Write 3D Printing. *Macromolecules* **2015**, *48* (18), 6482–6488.

(30) Constantinou, A. P.; Georgiou, T. K. Thermoresponsive Gels Based on ABC Triblock Copolymers: Effect of the Length of the PEG Side Group. *Polym. Chem.* **2016**, *7* (11), 2045–2056.

(31) Hunt, J. N.; Feldman, K. E.; Lynd, N. A.; Deek, J.; Campos, L. M.; Spruell, J. M.; Hernandez, B. M.; Kramer, E. J.; Hawker, C. J. Tunable, High Modulus Hydrogels Driven by Ionic Coacervation. *Adv. Mater.* **2011**, *23* (20), 2327–2331.

(32) K. Y. Lee, D. J. M. Alginate: Properties and Biomedical Applications. *Prog. Polym. Sci.* **2012**, *37* (1), 106–126.

(33) Gao, H.; Wang, N.; Hu, X.; Nan, W.; Han, Y.; Liu, W. Double Hydrogen-Bonding PH-Sensitive Hydrogels Retaining High-Strengths over a Wide PH Range. *Macromol. Rapid Commun.* **2013**, *34* (1), 63–68.

(34) Zhang, S.; Bellinger, A. M.; Glettig, D. L.; Barman, R.; Lee, Y. A. L.; Zhu, J.; Cleveland, C.; Montgomery, V. A.; Gu, L.; Nash, L. D.; et al. A PH-Responsive Supramolecular Polymer Gel as an Enteric Elastomer for Use in Gastric Devices. *Nat. Mater.* **2015**, *14* (10), 1065–1071.

(35) O'Lenick, T. G.; Jiang, X.; Zhao, B. Thermosensitive Aqueous Gels with Tunable Sol-Gel Transition Temperatures from Thermo- and PH-Responsive Hydrophilic ABA Triblock Copolymer. *Langmuir* **2010**, *26* (11), 8787–8796.

(36) Dankers, P. Y. W.; Hermans, T. M.; Baughman, T. W.; Kamikawa, Y.; Kieltyka, R. E.; Bastings, M. M. C.; Janssen, H. M.; Sommerdijk, N. A. J. M.; Larsen, A.; Van Luyn, M. J. A.; et al. Hierarchical Formation of Supramolecular Transient Networks in Water: A Modular Injectable Delivery System. *Adv. Mater.* **2012**, *24* (20), 2703–2709.

(37) Pawar, G. M.; Koenigs, M.; Fahimi, Z.; Cox, M.; Voets, I. K.; Wyss, H. M.; Sijbesma, R. P. Injectable Hydrogels from Segmented PEG-Bisurea Copolymers. *Biomacromolecules*

2012, *13* (12), 3966–3976.

(38) Highley, C. B.; Rodell, C. B.; Burdick, J. A. Direct 3D Printing of Shear-Thinning Hydrogels into Self-Healing Hydrogels. *Adv. Mater.* **2015**, *27* (34), 5075–5079.

(39) Li, L.; Yan, B.; Yang, J.; Chen, L.; Zeng, H. Novel Mussel-Inspired Injectable Self-Healing Hydrogel with Anti-Biofouling Property. *Adv. Mater.* **2015**, *27* (7), 1294–1299.

(40) Engler, A. J.; Sen, S.; Sweeney, H. L.; Discher, D. E. Matrix Elasticity Directs Stem Cell Lineage Specification. *Cell* **2006**, *126* (4), 677–689.

(41) Burdick, J. A.; Prestwich, G. D. Hyaluronic Acid Hydrogels for Biomedical Applications. *Adv. Mater.* **2011**, *23* (12), H41–H56.

(42) Khetan, S.; Burdick, J. A. Patterning Hydrogels in Three Dimensions towards Controlling Cellular Interactions. *Soft Matter* **2011**, *7* (3), 830–838.

(43) Kolesky, D. B.; Truby, R. L.; Gladman, A. S.; Busbee, T. A.; Homan, K. A.; Lewis, J. A. 3D Bioprinting of Vascularized, Heterogeneous Cell-Laden Tissue Constructs. *Adv. Mater.* **2014**, *26* (19), 3124–3130.

(44) Wang, H.; Heilshorn, S. C. Adaptable Hydrogel Networks with Reversible Linkages for Tissue Engineering. *Adv. Mater.* **2015**, *27* (25), 3717–3736.

(45) Rosales, A. M.; Anseth, K. S. The Design of Reversible Hydrogels to Capture Extracellular Matrix Dynamics. *Nat. Rev. Mater.* **2016**, *1* (2), 15012/1-15.

(46) Sershen, S. R.; Westcott, S. L.; Halas, N. J.; West, J. L. Temperature-Sensitive Polymer-Nanoshell Composites for Photothermally Modulated Drug Delivery. *J. Biomed. Mater. Res.* **2000**, *51* (3), 293–298.

(47) Yamagata, T.; Morishita, M.; Kavimandan, N. J.; Nakamura, K.; Fukuoka, Y.; Takayama, K.; Peppas, N. A. Characterization of Insulin Protection Properties of Complexation Hydrogels in Gastric and Intestinal Enzyme Fluids. *J. Control. Release* **2006**, *112* (3), 343–349.

(48) Webber, M. J.; Matson, J. B.; Tamboli, V. K.; Stupp, S. I. Controlled Release of Dexamethasone from Peptide Nanofiber Gels to Modulate Inflammatory Response. *Biomaterials* **2012**, *33* (28), 6823–6832.

(49) Barry, R. A.; Shepherd, R. F.; Hanson, J. N.; Nuzzo, R. G.; Wiltzius, P.; Lewis, J. A. Direct-Write Assembly of 3D Hydrogel Scaffolds for Guided Cell Growth. *Adv. Mater.* **2009**, *21* (23), 2407–2410.

(50) Wojtecki, R. J.; Nelson, A. Small Changes with Big Effects: Tuning Polymer Properties with Supramolecular Interactions. *J. Polym. Sci. Part A Polym. Chem.* **2016**, *54* (4), 457–472.

(51) Yu, L.; Chang, G.; Zhang, H.; Ding, J. Temperature-Induced Spontaneous Sol–Gel Transitions of Poly(D,L-Lactic Acid-Co-Glycolic Acid)-b-Poly(Ethylene Glycol)-b-Poly(D,L-Lactic Acid-Co-Glycolic Acid) Triblock Copolymers and Their End-Capped Derivatives in Water. *J. Polym. Sci. Part A Polym. Chem.* **2007**, *45*, 1122–1133.

(52) Popescu, M.; Liontos, G.; Avgeropoulos, A.; Voulgari, E.; Avgoustakis, K.; Tsitsilianis, C. Injectable Hydrogel: Amplifying the PH Sensitivity of a Triblock Copolypeptide by

Conjugating the N-Termini via Dynamic Covalent Bonding. *ACS Appl. Mater. Interfaces* **2016**, *8*, 17539–17548.

(53) Binder, W. H.; Petraru, L.; Roth, T.; Groh, P. W.; Pálfi, V.; Keki, S.; Ivan, B. Magnetic and Temperature-Sensitive Release Gels from Supramolecular Polymers. *Adv. Funct. Mater.* **2007**, *17* (8), 1317–1326.

(54) Hu, X.; Vatankhah-Varnoosfaderani, M.; Zhou, J.; Li, Q.; Sheiko, S. S. Weak Hydrogen Bonding Enables Hard, Strong, Tough, and Elastic Hydrogels. *Adv. Mater.* **2015**, *27* (43), 6899–6905.

(55) Hirschberg, J. H. K. K.; Brunsveid, L.; Ramzi, A.; Vekemans, J. A. J. M.; Sijbesma, R. P.; Meijer, E. W. Helical Self-Assembled Polymers from Cooperative Stacking of Hydrogen-Bonded Pairs. *Nature* **2000**, *407* (6801), 167–170.

(56) Koevoets, R. A.; Versteegen, R. M.; Kooijman, H.; Spek, A. L.; Sijbesma, R. P.; Meijer, E. W. Molecular Recognition in a Thermoplastic Elastomer. *J. Am. Chem. Soc.* **2005**, *127* (9), 2999–3003.

(57) Binder, W. H.; Kunz, M. J.; Kluger, C.; Hayn, G.; Saf, R. Synthesis and Analysis of Telechelic Polyisobutylenes for Hydrogen-Bonded Supramolecular Pseudo-Block Copolymers. *Macromolecules* **2004**, *37* (5), 1749–1759.

(58) Vora, A.; Zhao, B.; To, D.; Cheng, J. Y.; Nelson, A. Blends of PS-PMMA Diblock Copolymers with a Directionally Hydrogen Bonding Polymer Additive. *Macromolecules* **2010**, *43* (3), 1199–1202.

(59) Sijbesma, R. P.; Beijer, F. H.; Brunsveld, L.; Folmer, B. J. B.; Hirschberg, J. H. K. K.; Lange, R. F. M.; Lowe, J. K. L.; Meijer. Reversible Polymers Formed from Self-Complementary Monomers Using Quadruple Hydrogen Bonding. *Science (80-.).* **1997**, *278* (5343), 1601–1604.

(60) Beijer, F. H.; Sijbesma, R. P.; Kooijman, H.; Spek, A. L.; Meijer, E. W. Strong Dimerization of Ureidopyrimidones via Quadruple Hydrogen Bonding. *J. Am. Chem. Soc.* **1998**, *120* (27), 6761–6769.

(61) Guo, M.; Pitet, L. M.; Wyss, H. M.; Vos, M.; Dankers, P. Y. W.; Meijer, E. W. Tough Stimuli-Responsive Supramolecular Hydrogels with Hydrogen-Bonding Network Junctions. *J. Am. Chem. Soc.* **2014**, *136* (19), 6969–6977.

(62) Chebotareva, N.; Bomans, P. H. H.; Frederik, P. M.; Sommerdijk, N. A. J. M.; Sijbesma, R. P. Morphological Control and Molecular Recognition by Bis-Urea Hydrogen Bonding in Micelles of Amphiphilic Tri-Block Copolymers. *Chem. Commun. (Camb).* **2005**, No. 39, 4967–4969.

(63) Tharcis, M.; Breiner, T.; Belleney, J.; Boué, F.; Bouteiller, L. Hydrogen Bonded Supramolecular Polymers in Protic Solvents: Role of Multitopicity. *Polym. Chem.* **2012**, *3* (11), 3093.

(64) Karis, D. G.; Ono, R. J.; Zhang, M.; Vora, A.; Storti, D.; Ganter, M. A.; Nelson, A. Cross-Linkable Multi-Stimuli Responsive Hydrogel Inks for Direct-Write 3D Printing. *Polym. Chem.* **2017**, *8* (29), 4199–4206.

(65) Liu, T.; Zhou, Z.; Wu, C.; Chu, B.; Schneider, D. K.; Nace, V. M. Self-Assembly of

Poly(Oxybutylene)-Poly(Oxyethylene)-Poly(Oxybutylene) (B6E46B6) Triblock Copolymer in Aqueous Solution. *J. Phys. Chem. B* **1997**, *101* (43), 8808–8815.

(66) Aoki, S.; Koide, A.; Imabayashi, S.; Watanabe, M. Novel Thermosensitive Polyethers Prepared by Anionic Ring-Opening Polymerization of Glycidyl Ether Derivatives. *Chem. Lett.* **2002**, *31* (11), 1128–1129.

(67) Isono, T.; Miyachi, K.; Satoh, Y.; Sato, S.; Kakuchi, T.; Satoh, T. Design and Synthesis of Thermoresponsive Aliphatic Polyethers with a Tunable Phase Transition Temperature. *Polym. Chem.* **2017**, *8*, 5698–5707.

(68) Heinen, S.; Rackow, S.; Schäfer, A.; Weinhart, M. A Perfect Match: Fast and Truly Random Copolymerization of Glycidyl Ether Monomers to Thermoresponsive Copolymers. *Macromolecules* **2017**, *50* (1), 44–53.

(69) Chang, Y. L.; West, M. A.; Fowler, F. W.; Lauher, J. W. An Approach to the Design of Molecular Solids. Strategies for Controlling the Assembly of Molecules into Two-Dimensional Layered Structures. *J. Am. Chem. Soc.* **1993**, *115* (14), 5991–6000.

(70) van Esch, J.; Schoonbeek, F.; de Loos, M.; Kooijman, H.; Spek, A. L.; Kellogg, R. M.; Feringa, B. L. Cyclic Bis-Urea Compounds as Gelators for Organic Solvents. *Chem. - A Eur. J.* **1999**, *5*, 937–950.

(71) Lortie, F.; Boileau, S.; Bouteiller, L.; Chassenieux, C.; Demé, B.; Ducouret, G.; Jalabert, M.; Lauprêtre, F.; Terech, P. Structural and Rheological Study of a Bis-Urea Based Reversible Polymer in an Apolar Solvent. *Langmuir* **2002**, *18* (19), 7218–7222.

(72) Lortie, F.; Boileau, S.; Bouteiller, L. N,N′-Disubstituted Ureas: Influence of Substituents on the Formation of Supramolecular Polymers. *Chem. - A Eur. J.* **2003**, *9* (13), 3008–3014.

(73) Simic, V.; Bouteiller, L.; Jalabert, M. Highly Cooperative Formation of Bis-Urea Based Supramolecular Polymers. *J. Am. Chem. Soc.* **2003**, *125* (43), 13148–13154.

(74) Bouteiller, L.; Colombani, O.; Lortie, F.; Terech, P. Thickness Transition of a Rigid Supramolecular Polymer. *J. Am. Chem. Soc.* **2005**, *127* (24), 8893–8898.

(75) Bellot, M.; Bouteiller, L. Thermodynamic Description of Bis-Urea Self-Assembly: Competition between Two Supramolecular Polymers. *Langmuir* **2008**, *24*, 14176–14182.

(76) Brocorens, P.; Linares, M.; Guyard-Duhayon, C.; Guillot, R.; Andrioletti, B.; Suhr, D.; Isare, B.; Lazzaroni, R.; Bouteiller, L. Conformational Plasticity of Hydrogen Bonded Bis-Urea Supramolecular Polymers. *J. Phys. Chem. B* **2013**, *117* (17), 5379–5386.

(77) Koevoets, R. A.; Karthikeyan, S.; Magusin, P. C. M. M.; Meijer, E. W.; Sijbesma, R. P. Cross-Polymerization of Hard Blocks in Segmented Copoly(Ether Urea)S. *Macromolecules* **2009**, *42* (7), 2609–2617.

(78) Ning, L.; De-Ning, W.; Sheng-Kang, Y. Crystallinity and Hydrogen Bonding of Hard Segments in Segmented Poly(Urethane Urea) Copolymers. *Polymer (Guildf).* **1996**, *37* (16), 3577–3583.

(79) Colombani, O.; Barioz, C.; Bouteiller, L.; Chanéac, C.; Fompérie, L.; Lortie, F.; Montés, H. Attempt toward 1D Cross-Linked Thermoplastic Elastomers: Structure and Mechanical

Properties of a New System. *Macromolecules* **2005**, *38* (5), 1752–1759.

(80) Versteegen, R. M.; Kleppinger, R.; Sijbesma, R. P.; Meijer, E. W. Properties and Morphology of Segmented Copoly(Ether Urea)s with Uniform Hard Segments. *Macromolecules* **2006**, *39* (2), 772–783.

(81) Versteegen, R. M.; Sijbesma, R. P.; Meijer, E. W. Synthesis and Characterization of Segmented Copoly(Ether Urea)s with Uniform Hard Segments. *Macromolecules* **2005**, *38* (8), 3176–3184.

(82) Boileau, S.; Bouteiller, L.; Lauprêtre, F.; Lortie, F. Soluble Supramolecular Polymers Based on Urea Compounds. *New J. Chem.* **2000**, *24*, 845–848.

(83) Sheth, J. P.; Klinedinst, D. B.; Pechar, T. W.; Wilkes, G. L.; Yilgor, E.; Yilgor, I. Time-Dependent Morphology Development in a Segmented Polyurethane with Monodisperse Hard Segments Based on 1,4-Phenylene Diisocyanate. *Macromolecules* **2005**, *38* (24), 10074–10079.

(84) Piana, F.; Case, D. H.; Ramalhete, S. M.; Pileio, G.; Facciotti, M.; Day, G. M.; Khimyak, Y. Z.; Angulo, J.; Brown, R. C. D.; Gale, P. A. Substituent Interference on Supramolecular Assembly in Urea Gelators: Synthesis, Structure Prediction and NMR. *Soft Matter* **2016**, *12* (24), 5489–5489.

(85) Chassenieux, C.; Colombani, O.; Nicolai, T. Controlling the Dynamics of Self-Assembled Triblock Copolymer Networks via the PH. *Macromolecules* **2011**, *44*, 4487–4495.

(86) Tsitsilianis, C.; Serras, G.; Ko, C.-H.; Jung, F.; Papadakis, C. M.; Rikkou-Kalourkoti, M.; Patrickios, C. S.; Schweins, R.; Chassenieux, C. Thermoresponsive Hydrogels Based on Telechelic Polyelectrolytes: From Dynamic to "Frozen" Networks. *Macromolecules* **2018**, *51*, 2169–2179.

(87) Sami, S.; Yildirim, E.; Yurtsever, M.; Yurtsever, E.; Yilgor, E.; Yilgor, I.; Wilkes, G. L. Understanding the Influence of Hydrogen Bonding and Diisocyanate Symmetry on the Morphology and Properties of Segmented Polyurethanes and Polyureas: Computational and Experimental Study. *Polym. (United Kingdom)* **2014**, *55* (18), 4563–4576.

(88) Baddi, S.; Madugula, S. S.; Sarma, D. S.; Soujanya, Y.; Palanisamy, A. Combined Experimental and Computational Study of the Gelation of Cyclohexane-Based Bis(Acyl-Semicarbazides) and the Multi-Stimuli-Responsive Properties of Their Gels. *Langmuir* **2016**, *32*, 889–899.

(89) Labbé, A.; Carlotti, S.; Deffieux, A.; Hirao, A. Controlled Polymerization of Glycidyl Methyl Ether Initiated by Onium Salt/Triisobutylaluminum and Investigation of the Polymer LCST. *Macromol. Symp.* **2007**, *249–250*, 392–397.

(90) Schömer, M.; Frey, H. Water-Soluble "Poly(Propylene Oxide)" by Random Copolymerization of Propylene Oxide with a Protected Glycidol Monomer. *Macromolecules* **2012**, *45* (7), 3039–3046.

(91) Barteau, K. P.; Wolffs, M.; Lynd, N. A.; Fredrickson, G. H.; Kramer, E. J.; Hawker, C. J. Allyl Glycidyl Ether-Based Polymer Electrolytes for Room Temperature Lithium Batteries. *Macromolecules* **2013**, *46* (22), 8988–8994.

(92) Lee, A.; Lundberg, P.; Klinger, D.; Lee, B. F.; Hawker, C. J.; Lynd, N. A. Physiologically

Relevant, PH-Responsive PEG-Based Block and Statistical Copolymers with N,N-Diisopropylamine Units. *Polym. Chem.* **2013**, *4* (24), 5735–5742.

(93) Yilgor, I.; Yilgor, E.; Das, S.; Wilkes, G. L. Time-Dependent Morphology Development in Segmented Polyetherurea Copolymers Based on Aromatic Diisocyanates. *J. Polym. Sci. Part B Polym. Phys.* **2009**, *47*, 471–483.

(94) Yilgor, E.; Isik, M.; Yilgor, I. Novel Synthetic Approach for the Preparation of Poly(Urethaneurea) Elastomers. *Macromolecules* **2010**, *43* (20), 8588–8593.

(95) Montero De Espinosa, L.; Balog, S.; Weder, C. Isophthalic Acid-Pyridine H-Bonding: Simplicity in the Design of Mechanically Robust Phase-Segregated Supramolecular Polymers. *ACS Macro Lett.* **2014**, *3* (6), 540–543.

(96) Nambam, J. S.; Philip, J. Thermogelling Properties of Triblock Copolymers in the Presence of Hydrophilic Fe3O4 Nanoparticles and Surfactants. *Langmuir* **2012**, *28* (33), 12044–12053.

(97) Liaw, C. Y.; Henderson, K. J.; Burghardt, W. R.; Wang, J.; Shull, K. R. Micellar Morphologies of Block Copolymer Solutions near the Sphere/Cylinder Transition. *Macromolecules* **2015**, *48* (1), 173–183.

(98) Gröschel, A. H.; Walther, A. Block Copolymer Micelles with Inverted Morphologies. *Angew. Chemie - Int. Ed.* **2017**, *56* (37), 10992–10994.

(99) Chu, B.; Hsiao, B. S. Small-Angle X-Ray Scattering of Polymers. *Chem. Rev.* **2001**, *101* (6), 1727–1761.

(100) Li, M.; Liu, Y.; Nie, H.; Bansil, R.; Steinhart, M. Kinetics of Hexagonal-Body-Centered Cubic Transition in a Triblock Copolymer in a Selective Solvent: Time-Resolved Small-Angle X-Ray Scattering Measurements and Model Calculations. *Macromolecules* **2007**, *40* (26), 9491–9502.

(101) Matsen, M. W.; Schick, M. Stable and Unstable Phases of a Diblock Copolymer Melt. *Phys. Rev. Lett.* **1994**, *72* (16), 2660–2663.

(102) Tyler, C. A.; Morse, D. C. Orthorhombic Fddd Network in Triblock and Diblock Copolymer Melts. *Phys. Rev. Lett.* **2005**, *94* (20), 1–4.

(103) Matsen, M. W. Effect of Architecture on the Phase Behavior of AB-Type Block Copolymer Melts. *Macromolecules* **2012**, *45* (4), 2161–2165.

(104) Ilavsky, J. Nika: Software for Two-Dimensional Data Reduction. *J. Appl. Crystallogr.* **2012**, *45* (2), 324–328.

Chapter 3. TRIBLOCK COPOLYMERS WITH ALKYL AND ARYL CHAIN ENDS

3.1 INTRODUCTION

The temperature-dependent aqueous solubility of some polymers is a critical property for applications like targeted drug delivery, tissue regeneration, and microfluidic devices.[1–5] Hydrogel-forming polymers that dissolve or "melt" in response to a temperature change allow homogeneous incorporation of additives and encapsulation or release of drug molecules. Thermoresponsive polymer hydrogels are also important in the 3D printing process. For example, polymers that exhibit lower critical solution temperature (LCST) behavior in water, like Pluronic F127, have been used as fugitive inks to print vasculature and other complex 3D objects.[6–8] Precise control of the temperature response is particularly valuable for injectable hydrogels, wherein the material is a gel at room temperature (~20-25 °C) but flows at human body temperature (~37 °C), or vice versa. For temperature-responsive poly(glycidyl ether)s, previous work has focused on controlling the transition temperature by changing the polymer side chain composition.[9–13] By altering the glycidyl ether side chain altogether or by synthesizing co-polymers of different glycidyl ethers, the cloud point temperature (T_{cp}) of these polymers can be tuned over a wide range, from about 10-90 °C. However, novel glycidyl ether monomers require optimization of polymerization conditions, and some may require lab-scale synthesis. Furthermore, polymers like poly(methyl glycidyl ether) are difficult to prepare except in the presence of air and moisture-sensitive catalysts.[14] A simpler strategy to tune the thermal response of polymer hydrogels that does not require extensive synthesis, design, or iterative optimization would be more time and

cost-effective. The ideal process would require only 1-2 high-yielding synthetic transformations and would afford significant, measurable changes in the temperature response.

Herein, I report triblock co-polymers with temperature responses that can be changed merely by altering the polymer end groups in a single synthetic step. The strategy is similar to the chain-end ureas reported in Chapter 2, but utilizes C_2, C_6, or C_7 alkyl/aryl esters instead of aryl ureas. The design is straightforward; a single polymer composition with four different end groups afforded a range of thermal responses. This ongoing, unpublished work demonstrates that small synthetic changes to polymer end groups have macroscopic effects on the thermal responses of the corresponding hydrogels.

3.2 Results and Discussion

Data from DSC and SAXS experiments showed that in the 25 wt% 8k-iPr-bisU system (Chapter 2), significant microphase separation occurred between the block co-polymer and the *bis*-urea chain ends, resulting in a regular nanostructure. Although inconclusive, VT-IR experiments implied that even at low temperatures, the *bis*-urea motifs remained strongly hydrogen-bonded to each other. Nevertheless, the *bis*-urea motifs were flanked by benzene rings, which are quite hydrophobic. During investigation of how urea chain ends affect hydrogel temperature response and mechanical properties, it was difficult to distinguish between the purely hydrophobic contributions of these rings and the hydrogen-bonding assembly of the ureas. I theorized that the rings acted both as rigid anchor points to limit conformational flexibility of the ureas as well as hydrophobic “shields” to screen the ureas from competing hydrogen-bonding interactions with water.

To better understand the effects of replacing hydroxyl end groups with hydrophobic end groups, I chose unsubstituted alkyl and aryl hydrocarbons as the next chain ends to study. These relatively simple end groups would serve as a control to differentiate between weak non-covalent interactions (*e.g.*, induced dipole-induced dipole) and stronger non-covalent interactions (*e.g.*, hydrogen-bonding, charge-charge, dipole-dipole). The 8k-iPr polymer composition was changed to M_n = 20,000 g mol^{-1} PEO and poly(ethyl glycidyl ether) (PEGE), or 20k-Et for short. We discovered that a longer PEO chain decreased the critical polymer concentration required for gelation. This was true for all 20k-PEO polymer triblocks compared to 8k-PEO polymers with equivalent block volume fractions. The trend also seemed largely independent from the composition of the glycidyl ether blocks. For example, 20k-PEO triblocks with relatively hydrophilic PEGE blocks were capable of gelation at 10 wt%, which was not true for 8k-PEO triblocks with comparatively hydrophobic poly(isopropyl glycidyl ether) (PiPGE) blocks. I chose PEGE as the glycidyl ether block because it is more hydrophilic than PiPGE or statistical PEGE/PiPGE blends.[13] I predicted that the increased hydrophilicity of PEGE would offset the hydrophobic nature of the chain ends, thereby preserving thermoreversibility while affording measurable shifts in transition temperatures.

Four triblock co-polymers were prepared *via* anionic ring-opening polymerization of EGE from a 20k-PEO macroinitiator. The final DP of each PEGE block was 39-40, or 78-80 total, resulting in the total M_n ~ 28,000 g mol^{-1}. This polymer was subsequently esterified using alkyl or aryl acid chlorides to afford the polymers 20k-Et-C_2, 20k-Et-C_6, and 20k-Et-C_{7Ar} (Figure 3.1).

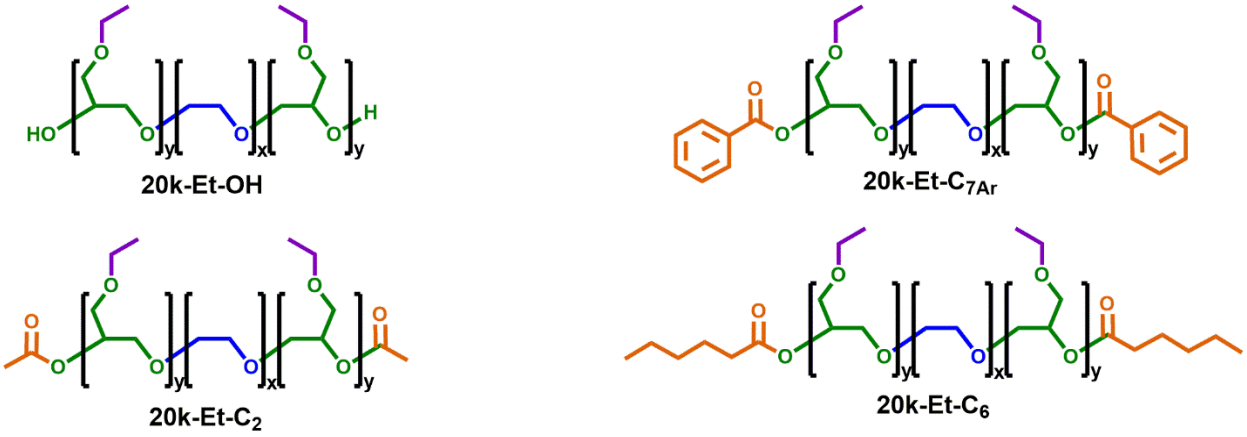

Figure 3.1. 20k-Et polymers with alkyl or aryl end groups

The same polymer formulation with four different end groups resulted in significant changes to the thermal response. Polymers were functionalized with alkyl/aryl acid chlorides as described in the experimental section.

Successful derivatization of polymer chain ends was confirmed by ^{1}H NMR spectroscopy. The degree of functionalization (f_n), as reported in the experimental section, was > 90% for the C_2 and C_6 formulations, and as high as 88% for the C_{7Ar} formulation. Some methylene proton signals in the C_6 chain end overlapped partially with polymer side-chain peaks or trace water. This overlap resulted in slight under- or over-integration when calculating f_n.

3.2.1 *Characterization of Thermal Response*

Vial-inversion temperature-concentration phase diagrams (Figure 3.2) were constructed for all formulations. As noted in the experimental section, the “viscous” regime was subjective and described flow behavior that was visibly slower than pure water. Notably, the sol-gel transition for the 20 wt% formulations correlated well with the T_{gel} values that were measured rheometrically (Figure 3.4 (b)); the transition for 20 wt% 20k-Et-OH occurred between 20-25 °C, while for 20%

20k-Et-C_6 the transition occurred between 5-10 °C. Although exact values for T_{gel} could not be determined from the phase diagrams, the diagrams showed where gels were immobile and self-supporting, both good indicators of gelation. Furthermore, the phase diagrams showed an appreciable decrease in the minimum polymer concentration required for gelation (C_{min}) at particular temperatures. For example, C_{min} at 25 °C was between 15-20% for 20k-Et-OH, but between 1-5% for 20k-Et-C_6. Rather than implying that fewer polymer chains are required to produce a physically cross-linked gel network, this apparent "effect" is likely an interpretation of the decrease in T_{gel} for each concentration. In other words, 5 wt% 20k-Et-OH might show a sol-gel transition at a temperature greater than 50 °C. The minimum concentration required for gelation at *any* temperature is unknown for these formulations, but it is likely > 1 wt%.

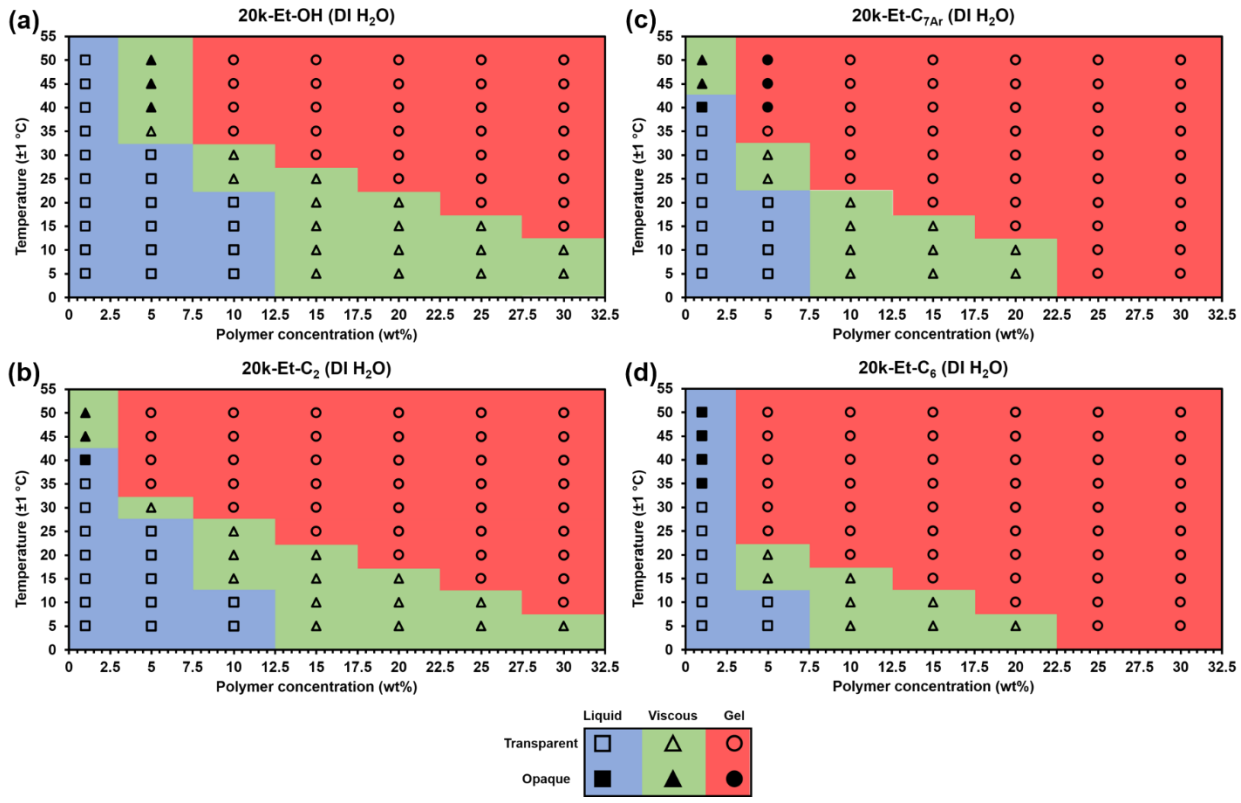

Figure 3.2. Temperature-concentration phase diagrams for 20k-Et polymers

All gels were prepared in DI water. (a) Phase diagram for 20k-Et-OH formulation. (b) Phase diagram for 20k-Et-C_2 formulation. (c) Phase diagram for the 20k-Et-C_{7Ar} formulation. (d) Phase diagram for the 20k-Et-C_6 formulation. Each concentration was maintained at the specified temperature for 5 min prior to inversion.

The temperature-driven sol-gel transition was quantified by two parameters: the cloud point temperature, T_{cp}, and the gelation temperature, T_{gel}. At and above the T_{cp}, a temperature-responsive polymer in solution forms aggregates sufficiently large to scatter visible light. For polymers showing LCST behavior in solvents, T_{cp} is often reported as "the" lower critical solution temperature, since this extent of aggregation usually signifies macroscopic phase separation. T_{cp} of the 20k-Et co-polymers decreased from 39.4 ± 0.1 °C (OH) to 36.3 ± 0.1 °C (C_2) to 30.8 °C (C_{7Ar}) to 27.3 ± 0.1 °C (C_6) (Figure 3.3). This trend suggests that the polymer became more

hydrophobic overall when the hydroxyl end-groups of the poly(ethyl glycidyl ether) blocks were converted to simple alkyl or aryl esters. The hydroxyl end-groups were capable of hydrogen-bonding interactions with water molecules, providing an enthalpic driving force that favored solvation. This means that PEGE blocks were less energetically likely to aggregate in aqueous solution. Therefore, hydrophobic aggregation and desolvation did not occur to a significant extent in the 20k-Et-OH formulation unless temperatures were high enough – in this case, around 39 °C.

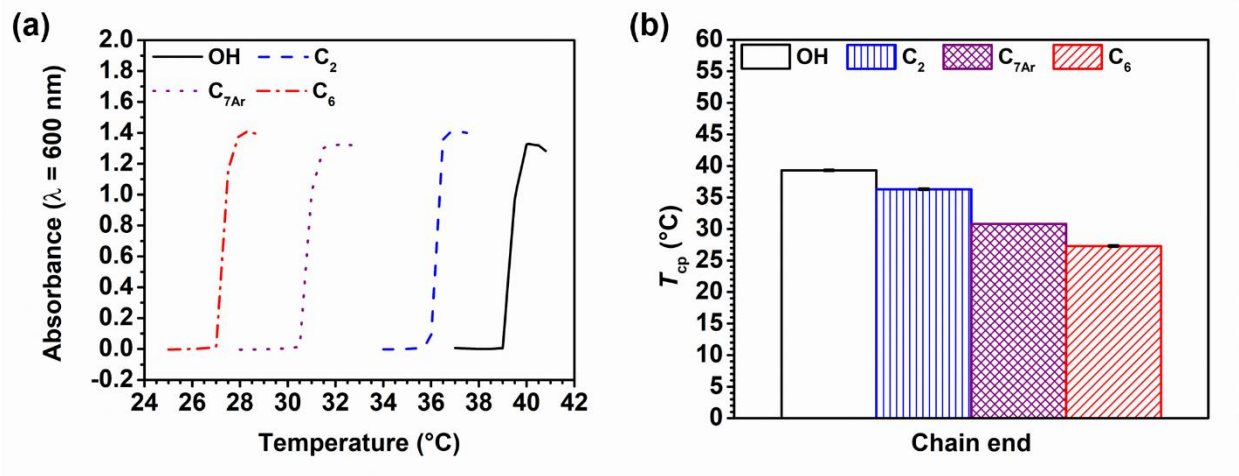

Figure 3.3. Cloud point temperatures for 20k-Et polymers

(a) T_{cp} was determined by heating 1 wt% polymer solutions at a rate of 0.5 °C min^{-1}, with 2 min equilibration at each temperature. Absorbance/transmittance was measured at λ = 600 nm for each temperature. T_{cp} is reported as the temperature at 50% of the difference between the initial absorbance and the maximum final absorbance. Gradual decreases in absorbance beyond the T_{cp} are due to density-dependent settling of aggregated polymer. (b) Plotted mean T_{cp} values for each formulation. Error bars represent standard deviation. The T_{cp} values for OH, C_2, C_{7Ar}, and C_6 are 39.4 ± 0.1, 36.3 ± 0.1, 30.8, and 27.3 ± 0.1 °C, respectively. Statistically significant differences are reported as follows: OH & C_2 ($p < 1 \times 10^{-6}$); OH & C_{7Ar} ($p < 1 \times 10^{-4}$); OH & C_6 ($p < 1 \times 10^{-8}$); C_2 & C_{7Ar} ($p < 1 \times 10^{-4}$); C_2 & C_6 ($p < 1 \times 10^{-8}$); C_{7Ar} & C_6 ($p < 1 \times 10^{-4}$).

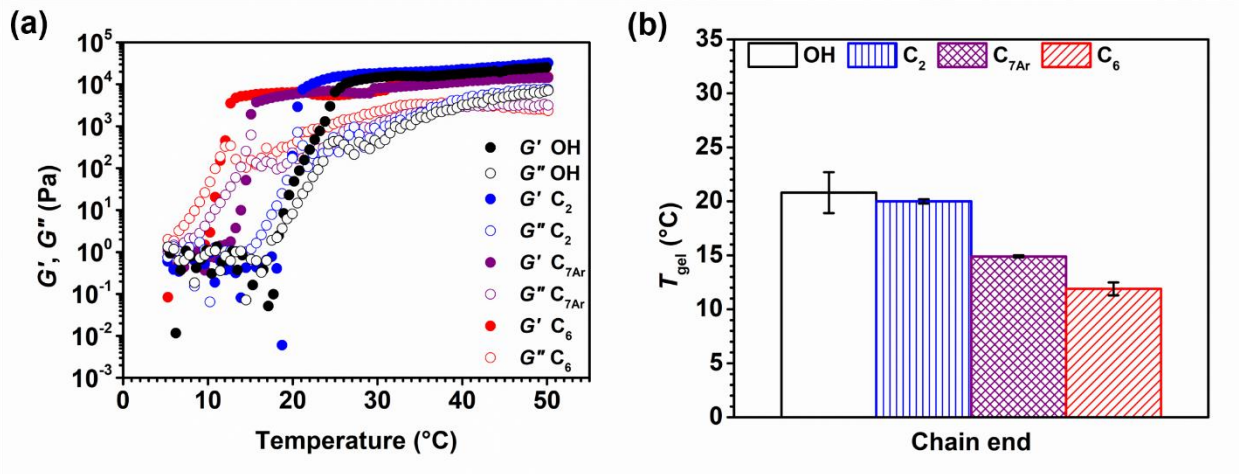

Figure 3.4. Temperature-ramp experiments for 20k-Et polymers

Rheometric temperature-ramp experiments were used to determine T_{gel} for all formulations. (a) Temperature-ramp experiments conducted between 5-50 °C at a heating rate of 2 °C min^{-1}, with γ = 0.1% and ω = 1 Hz. All plots are the mean of at least 3 experiments. (b) T_{gel} decreased when the hydroxyl end-group was replaced with alkyl and aryl esters. Error bars represent standard deviation. T_{gel} for the OH, C_2, C_{7Ar}, and C_6 formulations were 21 ± 2, 20.0 ± 0.2, 14.9 ± 0.1, and 11.9 ± 0.6 °C, respectively. Statistically significant differences are reported as follows: OH & C_{7Ar} ($p < 1 \times 10^{-2}$); OH & C_6 ($p < 1 \times 10^{-2}$); C_2 & C_{7Ar} ($p < 1 \times 10^{-5}$); C_2 & C_6 ($p < 1 \times 10^{-6}$); C_{7Ar} & C_6 ($p < 1 \times 10^{-3}$).

Rheometrically, T_{gel} can be defined in two ways: 1) the point at which *G' = G"* and after which *G' > G"*, or 2) the onset of *G'* increase, calculated using linear regression techniques. The onset point was difficult to accurately determine due to the "noise" in the data near the detection limits of the rheometer (moduli < 1 Pa); however, the crossover point was unique and unambiguous for each experiment. Hence, all reported measurements of T_{gel} refer to the point of modulus crossover. T_{gel} followed the same trend as T_{cp}, with values decreasing from OH (21 ± 2 °C) to C_2 (20.0 ± 0.2 °C) to C_{7Ar} (14.9 ± 0.1 °C) to C_6 ends (11.9 ± 0.6 °C) (Figure 3.4). There was no statistically significant difference in T_{gel} for the 20k-Et-OH and 20k-Et-C_2 formulations. The explanation is the same: hydrophobic aggregation of PEGE blocks is entropically driven, and with

increasing temperature, the equilibrium distribution of solvated polymer chains and assembled micelles shifts appreciably toward micelles. Notably, T_{gel} is much lower than T_{cp} for all formulations. T_{gel} is merely the formal rheological definition of gelation and does not itself describe the extent of aggregation or the mechanical properties of the gel. Simply put, when $T \geq T_{gel}$, polymer chains have aggregated enough to form an elastic, cross-linked network. Such a network may only form if individual micelles are bridged by PEO chains. The interdigitation of PEO chains between closely-packed micelles is likely also important for gelation. Vial-inversion phase diagrams show that no visible light-scattering aggregates form up to 50 °C when polymer concentrations are high enough for gelation. Although the T_{cp} was not quantitatively determined for polymer concentrations > 1 wt%, it is possible that at high enough concentrations, the T_{cp} transition is replaced altogether by the T_{gel} transition. At 1 wt%, these triblock copolymers are above their aqueous critical micelle concentration (CMC), according to unpublished work from our group. However, this concentration is low enough that a gel network cannot form. As such, there are fewer bridging and packing interactions between individual micelles.

3.2.2 *Rheometric Characterization of Viscoelastic Properties*

There was no statistically significant difference in either *G'* or the complex modulus, *G**, between any of the formulations (Figure 3.5). However, *G"* was significantly higher for the alkyl and aryl formulations compared to the hydroxyl formulation. Physically, this difference in *G"* (and thus, tan δ) means that the alkyl/aryl gels are less brittle and "tackier" than the OH gels. Nevertheless, the gels are equally rigid when shear is applied (because *G'* values are essentially the same). This could mean that hydrogen-bonding interactions between hydroxyl chain ends

provide more solid-like character. On the other hand, there is no hydrogen-bonding possible between alkyl/aryl ends, only weaker London dispersion forces.

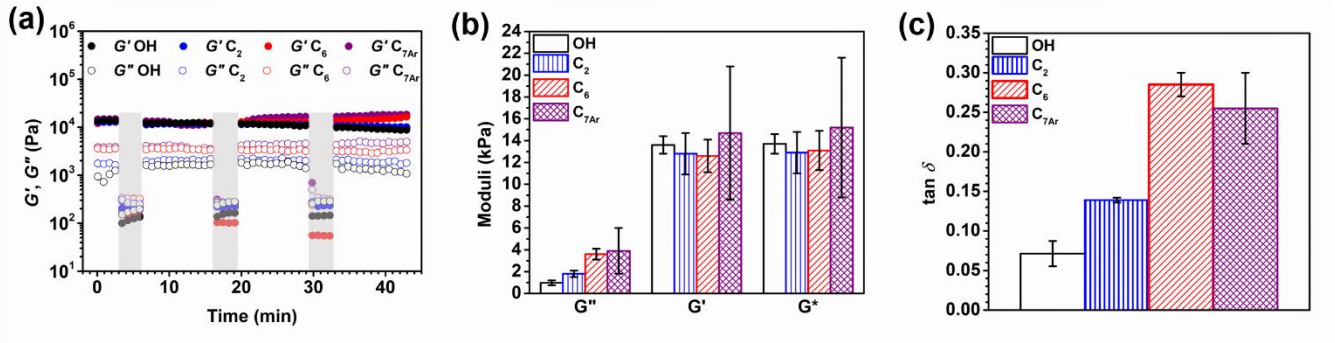

Figure 3.5. Cyclic step-strain experiments for 20k-Et polymers

All experiments were conducted at 30 °C and ω = 1 Hz. Strain amplitude alternated between 0.1% (white regions) and 100% (shaded regions). All plots are the mean of at least 3 experiments. (b) The complex (G^*) and storage (G') moduli were approximately equal for all formulations, but there were significant differences in G'': OH & C_2 ($p < 1 \times 10^{-2}$); OH & C_6 ($p < 5 \times 10^{-2}$); C_2 & C_6 ($p < 1 \times 10^{-2}$). (c) Statistically significant differences in the loss factor, tan δ, were as follows: OH & C_2 ($p < 1 \times 10^{-5}$); OH & C_6 ($p < 1 \times 10^{-6}$); OH & C_{7Ar} ($p < 5 \times 10^{-2}$); C_2 & C_6 ($p < 1 \times 10^{-5}$); C_2 & C_{7Ar} ($p < 5 \times 10^{-2}$).

At the molecular and nanoscales, the higher value of G'' for the alkyl/aryl gels indicates that a greater proportion of applied force is dispersed or lost, rather than elastically stored. The mechanism of energy dissipation is relative motion between polymer chains, resulting in friction and viscous heating. It is likely easier for relative motion to occur between polymer chains in the alkyl/aryl formulations because only weak London dispersion forces occur between the hydrocarbon moieties. The alkyl and aryl chain ends might act as plasticizers, lowering the glass transition temperature (T_g) of the PEGE blocks. Although the T_g of a PEGE homopolymer with one hydroxyl chain end is already well below room temperature, any decrease in T_g means that polymer chains have increased mobility at temperatures above the T_g. By contrast, energetically

stronger hydrogen-bonding interactions are possible in the hydroxyl end group gels. Whether disordered or not, these hydrogen bonds require more energy to disrupt, increasing the energy barrier for relative motion between PEGE chains. The presence of these hydrogen-bonding interactions may explain why the hydroxyl gels show a lower *G"* than the alkyl/aryl gels. Applied energy is "stored" or absorbed by hydrogen bonds, and so the hydroxyl gels exhibit a greater degree of rigid, elastic behavior compared to the alkyl/aryl gels.

No statistically significant difference in the critical stress value (σ_c) was observed between any of the gel formulations (Figure 3.6 (b,d)). However, the C_6 gels showed a higher critical strain value (γ_c = 2.2 ± 0.3%) than both the OH (γ_c = 1.2 ± 0.4%) and C_{7Ar} gels (γ_c = 1.0 ± 0.5%) (Figure 3.6 (a,c)). This means that the C_6 gels underwent about twice as much deformation as the OH and C_{7Ar} gels when subjected to approximately the same amount of pressure. This result is supported by the measurements of loss modulus: *G"* is higher for the C_6 gels, reflecting a higher ratio of viscous energy dissipation in response to applied force. The C_6 gels were less rigid than the OH gels and therefore underwent greater relative deformation before breaking. However, considering the high degree of variability for γ_c and σ_c measurements, these statistically significant differences may not be meaningful. Physically, the difference between 1% and 2% deformation is not especially significant.

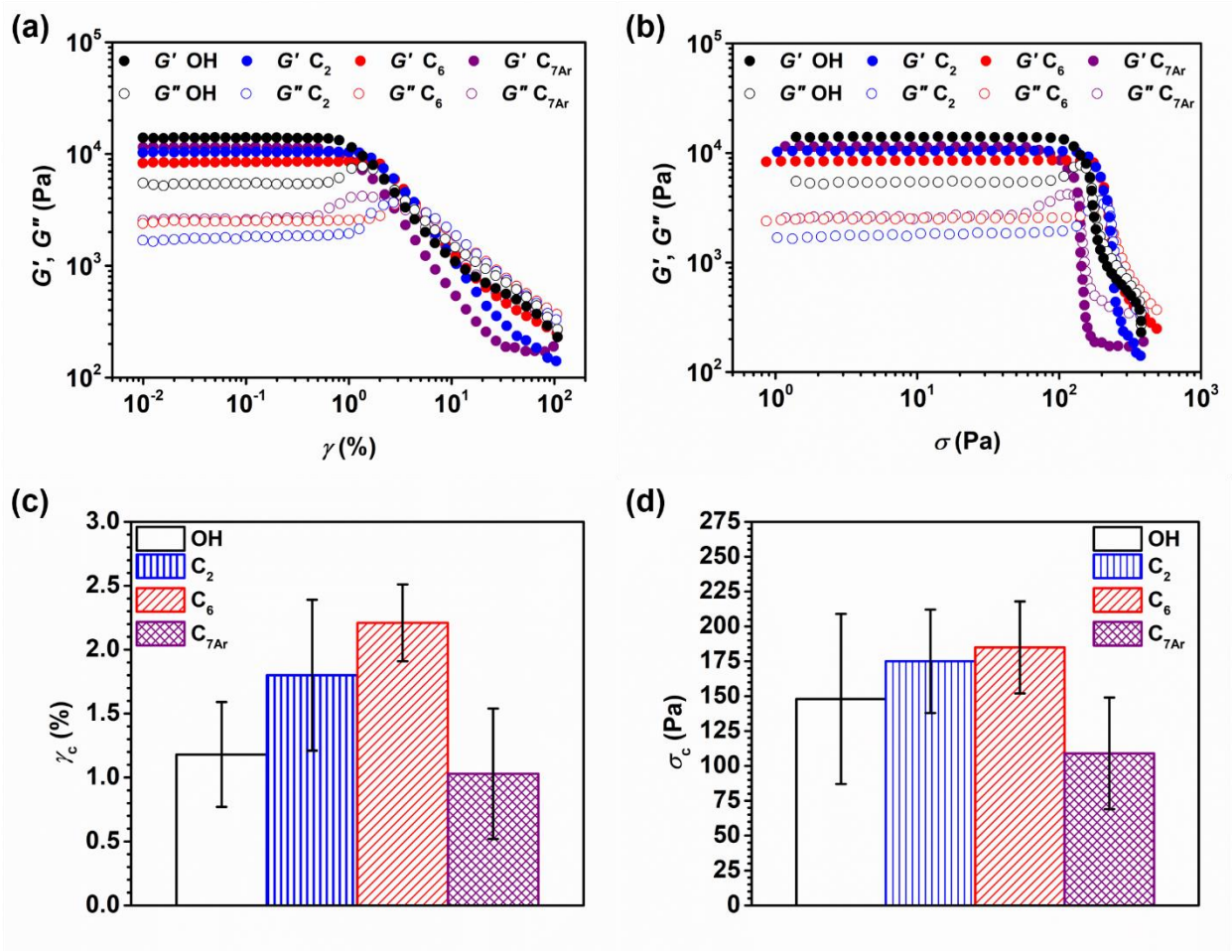

Figure 3.6. Strain amplitude and stress sweeps for 20k-Et polymers

All experiments were conducted at 30 °C and ω = 1 Hz. (a) Strain amplitude sweeps. The critical strain (γ_c) is reported as the point at which *G'* has decreased by 10% from the plateau value. (b) Stress sweeps derived from the strain-sweep experiments. The critical stress (σ_c) is reported as the point at which *G'* has decreased by 10% from the plateau value. All plots are the mean of at least 3 experiments. (c) The value of γ_c for the C_6 formulation was higher compared to the OH and C_{7Ar} polymers: OH & C_6 ($p < 5 \times 10^{-2}$); C_{7Ar} & C_6 ($p < 5 \times 10^{-2}$). (d) There were no statistically significant differences in σ_c between any of the formulations.

I hypothesized that the characteristic stress relaxation time, λ, for each of the gel formulations would be different due to changes in non-covalent intermolecular forces (Figure 3.7). For these physically cross-linked hydrogels, the mechanism of stress relaxation is thought to be

disassembly of individual micelles *via* chain pull-out. As relaxation occurs, bridging polymer chains pull out from their respective micelles and reform bridging interactions elsewhere in the network. Gels may also relax stress through rearrangement of non-covalent cross-links within hydrophobic micelle cores. It stands to reason that the alkyl/aryl formulations, with weaker intermolecular forces and greater chain mobility, showed a shorter λ than the hydroxyl formulation. Nevertheless, high variability in replicate measurements made it difficult to determine if the observed differences are statistically significant or physically meaningful.

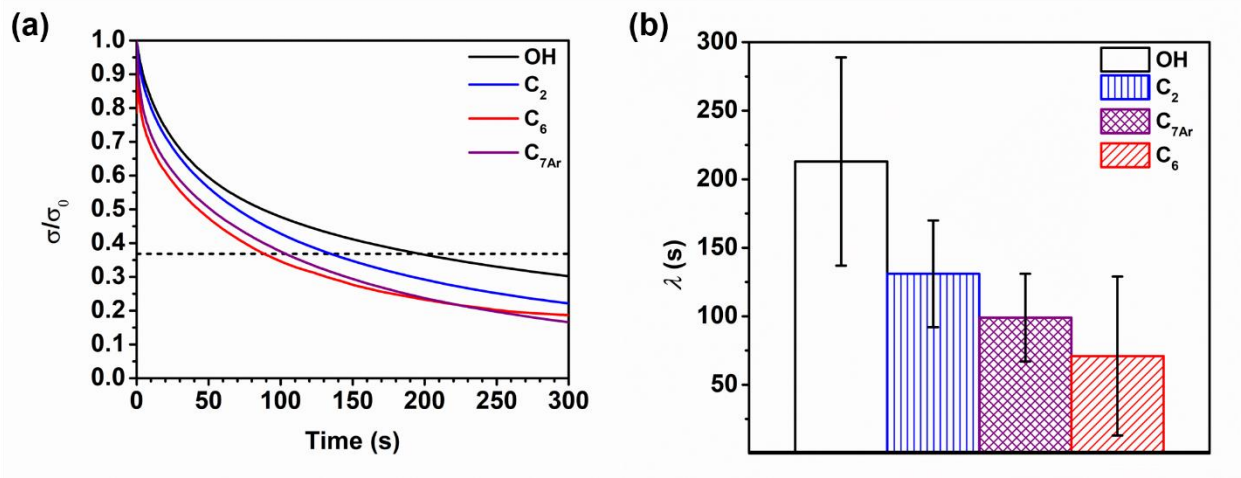

Figure 3.7. Stress relaxation experiments for 20k-Et hydrogels

(a) All gels (20 wt%, 30 °C) were pre-strained at 0.01% deformation for 60 s to help with reproducibility between samples (data not shown). Then, the gels were kept at 1.0% strain for up to 1 h. Only the first 5 min (300 s) are shown for clarity. The relaxation time, λ, is defined as the time required to reach 36.8% (1/e) of the initial stress value. All plots are the mean of at least 3 experiments. (b) There were no statistically significant differences in λ between the formulations, but the relaxation time appeared to decrease when the OH chain-end was replaced with an alkyl or aryl ester.

3.2.3 *X-Ray Scattering Experiments*

SAXS and WAXS experiments were performed on 20k-Et polymers as both 20 wt% hydrogels and powders to determine if end groups significantly altered polymer morphology,

particularly in the gel state. Based on previous SAXS experiments using the 8k-iPr urea-functionalized polymers, I expected the 20k-Et polymers to demonstrate either body-centered or face-centered cubic packing of spherical micelles in the gel state at 20 wt%. I did not expect end-group modification to radically alter gel morphology, but I did predict changes to the characteristic spacing (*i.e.*, periodicity) between micelles due to changes in polymer hydrophobicity and therefore micelle size and packing.

WAXS plots of intensity *vs.* scattering vector (q, $Å^{-1}$) for each 20k-Et formulation in the solid state (Figure 3.8) demonstrated that the alkyl/aryl end groups did not significantly alter the crystalline structure compared to the 20k-Et-OH polymer. As expected, the scattering profile of each 20k-Et polymer resembled that of highly crystalline PEO, with intense Bragg peaks at q = 1.3 and 1.5 $Å^{-1}$ and smaller peaks throughout.[15–17] The Bragg peak intensity is likely lower than that of pure PEO due to the presence of amorphous poly(ethyl glycidyl ether) domains, which disrupt the crystalline structure to some extent.

SAXS plots of intensity *vs.* scattering vector (q, $Å^{-1}$) for each 20k-Et formulation as a 20 wt% gel (Figure 3.9) showed a single correlation peak for each formulation. Poor signal-to-noise ratio precluded observation of any additional peaks, so peak-position ratios could not be used to determine packing order. The periodicity, $d = 2\pi / q$, ranged from 19.8-21.7 nm (198-217 Å), showing little to no difference between polymer formulations.

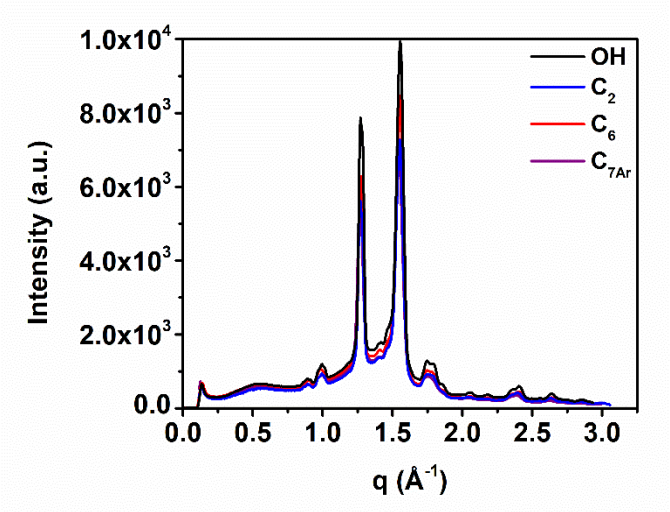

Figure 3.8. WAXS plots for 20k-Et polymers

WAXS plots were obtained for each 20k-Et polymer formulation in the solid state. Polymer end groups had no apparent effect on the crystalline packing.

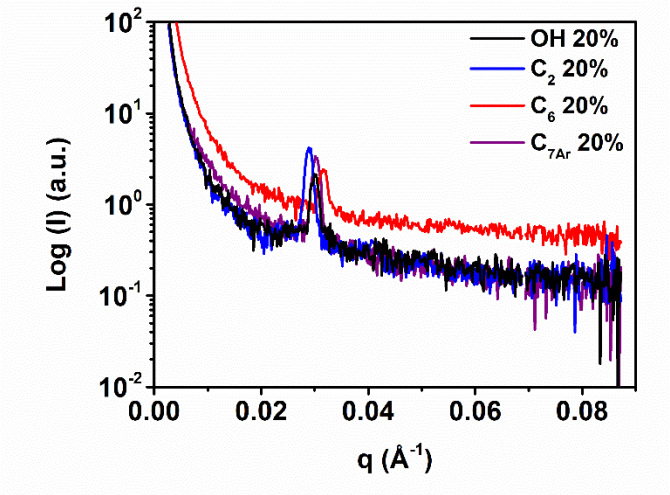

Figure 3.9. SAXS plots for 20k-Et polymer hydrogels

All formulations were tested as 20 wt% hydrogels. Poor signal-to-noise ratio precluded assessment of packing order, and only one correlation peak was observed for each formulation. Periodicity, $d = 2\pi / q$, ranged from 19.8-21.7 nm (198-217 Å).

3.3 CONCLUSIONS

Converting hydroxyl end groups to purely hydrophobic alkyl or aryl esters resulted in increased overall hydrophobicity of the triblock co-polymers. This change was reflected in the temperature-dependent phase behavior of the polymer hydrogels: both T_{cp} and T_{gel} decreased when end groups were converted from an OH group to a C_x hydrocarbon. I propose that this decrease in transition temperatures was due to the same thermodynamic principles that drive LCST behavior in poly(alkyl glycidyl ether)s. As temperature increases, the free energy of solvation for the poly(alkyl glycidyl ether) blocks changes from negative (favorable) to positive (unfavorable) due in part to the entropic effects of clathrate-like solvation by water molecules. Although T_{cp} and T_{gel} both decreased, G' and σ_c were unchanged between hydroxyl and hydrocarbon chain ends. However, G'' and tan δ were both greater for alkyl/aryl chain-end formulations compared to hydroxyl ends. These increases in viscous behavior and plasticity were due to the replacement of hydrogen-bonding interactions with energetically weaker London dispersion forces between hydrocarbons.

3.4 EXPERIMENTAL

3.4.1 *Synthesis of 20k-Et-OH Polymer*

An oven-dried, 5-neck reactor flask was charged with poly(ethylene oxide) (PEO; 1.00 eq / 25.6 g, Sigma BioUltra, M_n = 20,000 g mol^{-1}), 18-crown-6 ether (2.49 eq / 0.841 g, TCI America, > 98.0%), and a glass-coated stir bar. The flask was evacuated and purged with argon three times, and PEO/18-crown-6 were then dried under reduced pressure at 80 °C for 24 h. Dried PEO/18-crown-6 was cooled to 65 °C, then dissolved in anhydrous THF

(~75 mL) under argon atmosphere to a final PEO concentration of ~35% w/v. Potassium naphthalenide 1.0 M THF solution (1.8 eq / 3.0 mL) was slowly added *via* syringe to the dissolved PEO. Degassed EGE (114 eq / 14.9 g) was added quickly *via* syringe.

After 22 h of polymerization at 70 °C under argon atmosphere, an aliquot (~0.5 mL) of reaction mixture was removed and quenched with 50 µL of 2% v/v AcOH:MeOH. The quenched aliquot was purified as described below, then analyzed by ^{1}H NMR in $CDCl_3$ (5% w/v). Following analysis of this first aliquot, additional EGE (72.8 eq / 9.52 g) was added by dry, argon-purged syringe. Subsequent aliquots were analyzed every 24 h until the desired poly(ethyl glycidyl ether) (PEGE) block length (DP = 39-40) was observed by ^{1}H NMR. In total, 187 eq of EGE was used, and the polymerization time was 145 h at 70 °C.

The reaction was then quenched by addition of degassed 2% v/v AcOH:MeOH (~20 mL). The reaction mixture was concentrated *in vacuo,* then precipitated in a large excess (1.5 L) of anhydrous Et_2O at RT for 30 min. The slurry was centrifuged, and the supernatant was discarded. The settled, off-white solid was rinsed a total of three times with fresh Et_2O. Recovered white solid was dried in air at RT for 1 h, then dried at RT under reduced pressure for 72 h.

To remove traces of potassium ion (and potentially naphthalene/dihydronaphthalene), dried polymer was reconstituted in ~300 mL CH_2Cl_2, then stirred with 1.05 g Dowex 50WX8 cation exchange resin (Sigma-Aldrich, hydrogen form, 100-200 mesh) at RT for 45 min. Following vacuum filtration and concentration, the pure polymer was dried under reduced pressure at 40-50 °C for 48 h. Degree of polymerization (DP) for the PEGE blocks was estimated by ^{1}H NMR spectroscopy to be DP = 39-40 (78-80 total; approximately 8,100 g mol^{-1}) as described in section

3.4.4. Gel permeation chromatography (GPC) indicated narrow dispersity, Đ = 1.19, suggesting little to no chain transfer or termination, in agreement with the living nature of the polymerization.

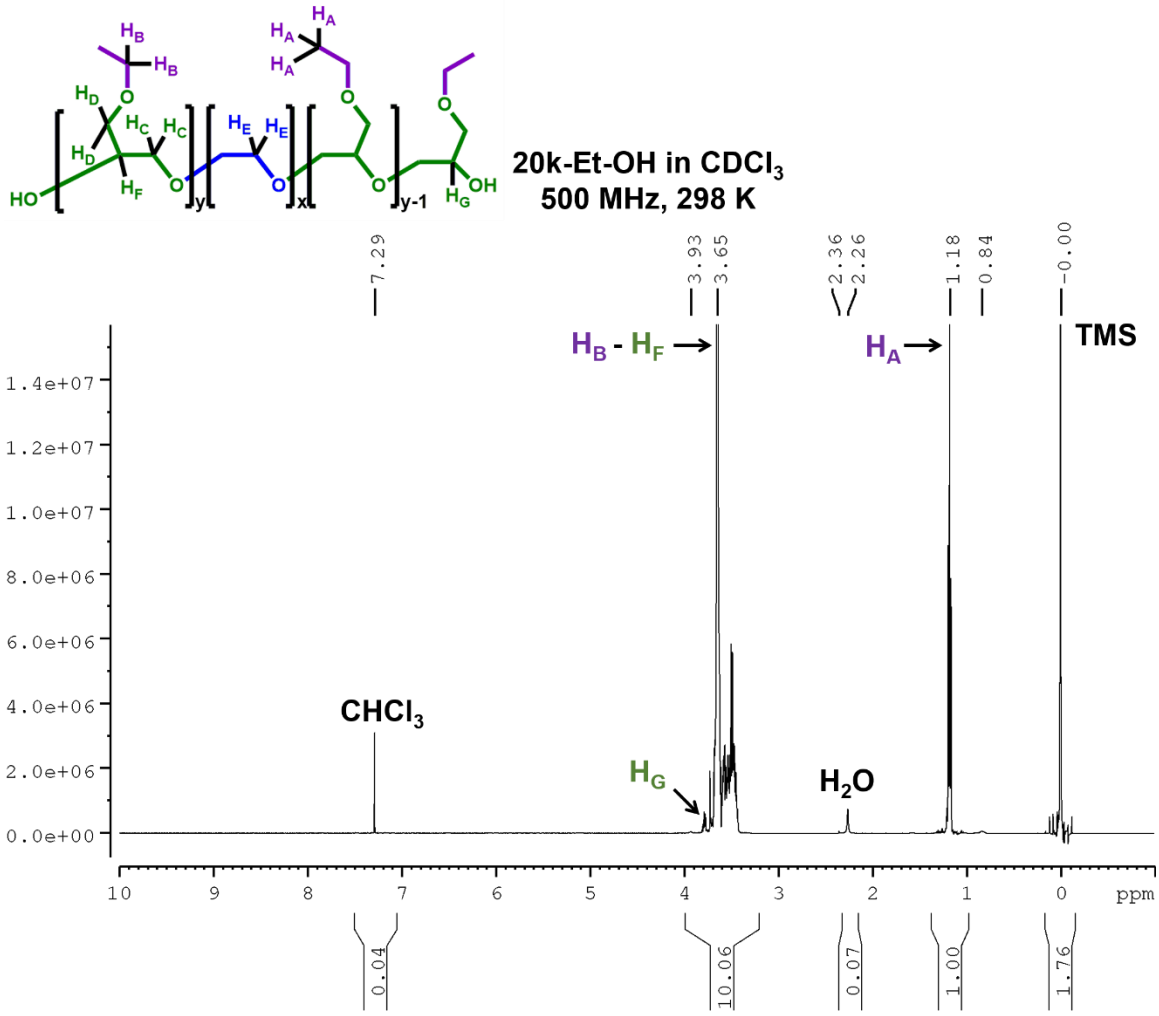

Figure 3.10. ^{1}H NMR spectrum of 20k-Et-OH in $CDCl_3$

500 MHz / *T* = 298 K

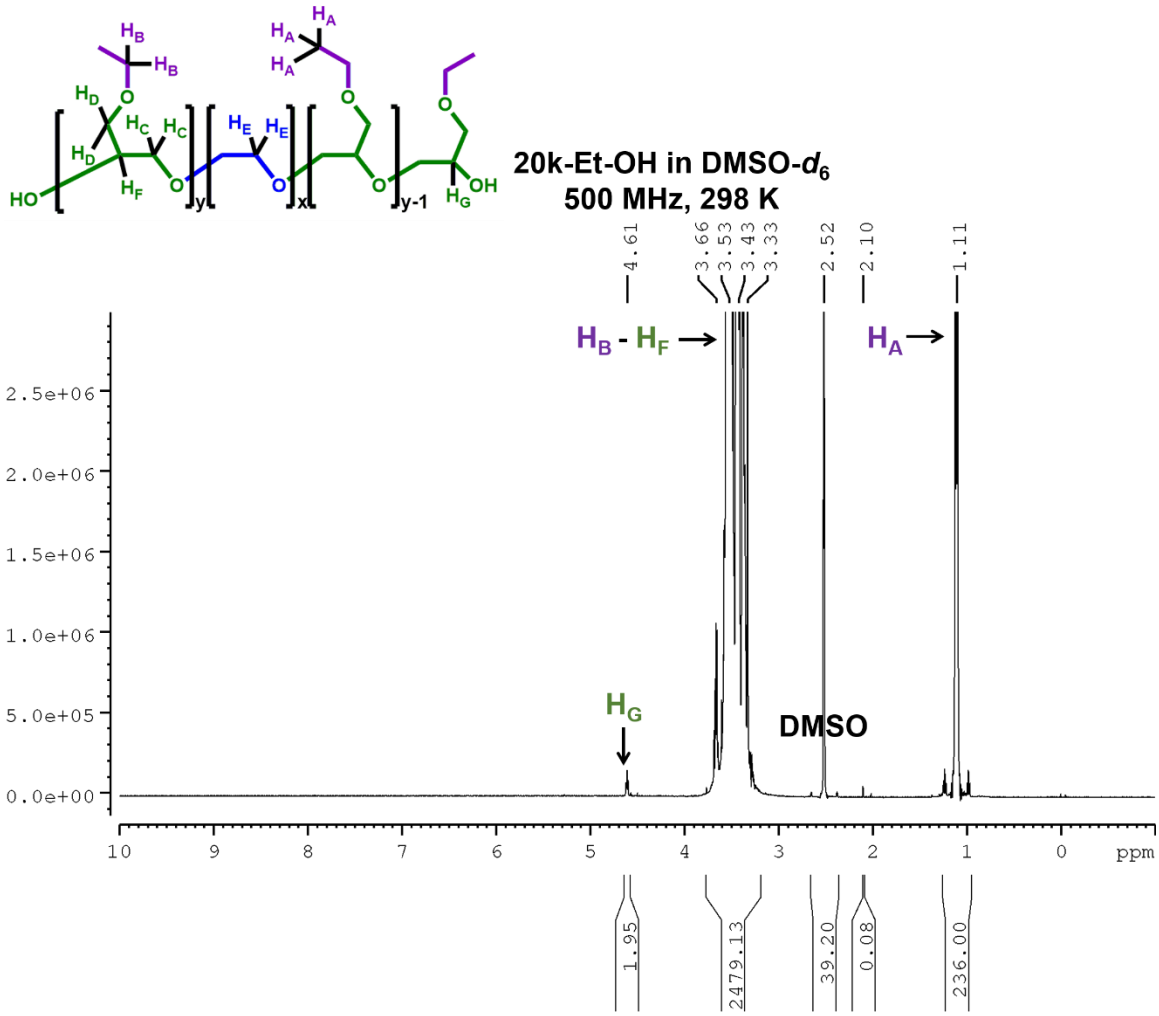

Figure 3.11. ^{1}H NMR spectrum of 20k-Et-OH in DMSO-d_6
500 MHz / T = 298 K

3.4.2 *Synthesis of 20k-Et-C_2 and 20k-Et-C_6*

Prior to functionalization, a multi-neck RBF was charged with 1.0 eq of 20k-Et-OH polymer and a Teflon-coated magnetic stir bar. The flask was evacuated, then backfilled with N_2 a total of two times. Polymer was then dried at 70 °C under reduced pressure for 18-20 h. Under N_2 atmosphere, dried polymer was dissolved in two-thirds the final target volume of CH_3CN (dried over anhydrous $MgSO_4$ at RT). NEt_3 (10 eq, distilled from CaH_2) was added *via* oven-dried syringe

needle to the dissolved polymer. The relevant acid chloride (100 eq) was dissolved in the remaining one-third final volume of CH_3CN. The polymer/NEt_3 solution was cooled to 0 °C in a water/ice bath. Diluted acid chloride was then added dropwise *via* addition funnel to the polymer/NEt_3 at 0 °C at a rate of ~1.5 mL min^{-1}. The reaction mixture was maintained at 0 °C for 10 min, then warmed to 25 °C in a PDMS bath and stirred for 18-20 h. At all times, the reaction mixture was kept under positive N_2 pressure.

After 18-20 h total reaction time, solvent was removed *in vacuo*, and the residue was stirred in excess Et_2O (~50 mL per gram of polymer) at RT for 15 min, then centrifuged. The supernatant was discarded, and the pelleted polymer was rinsed three times with fresh Et_2O. Recovered polymer was dried for 30 min at RT at ambient pressure, then dried under reduced pressure at RT for 1-2 h. Dried polymer was reconstituted in CH_2Cl_2 to a final concentration of 2-3% w/v. The solution was extracted three times with aqueous 0.1 M HCl, then once with brine (saturated aqueous NaCl). The CH_2Cl_2 layer was subsequently dried over anhydrous $MgSO_4$, filtered, and concentrated *in vacuo*. Finally, the remaining solvent was removed by drying under reduced pressure at RT for 18-24 h to afford polymers 20k-Et-C_2 and 20k-Et-C_6. Alkyl-functionalized polymers were recovered as white solids. Degree of functionalization (f_n) was estimated by ^1H NMR in $CDCl_3$ as described in section 3.4.5. For acetate (C_2) ends: f_n = 92-96% (mean = 94%). For hexanoate (C_6) ends: f_n = 91-100% (mean = 98%).

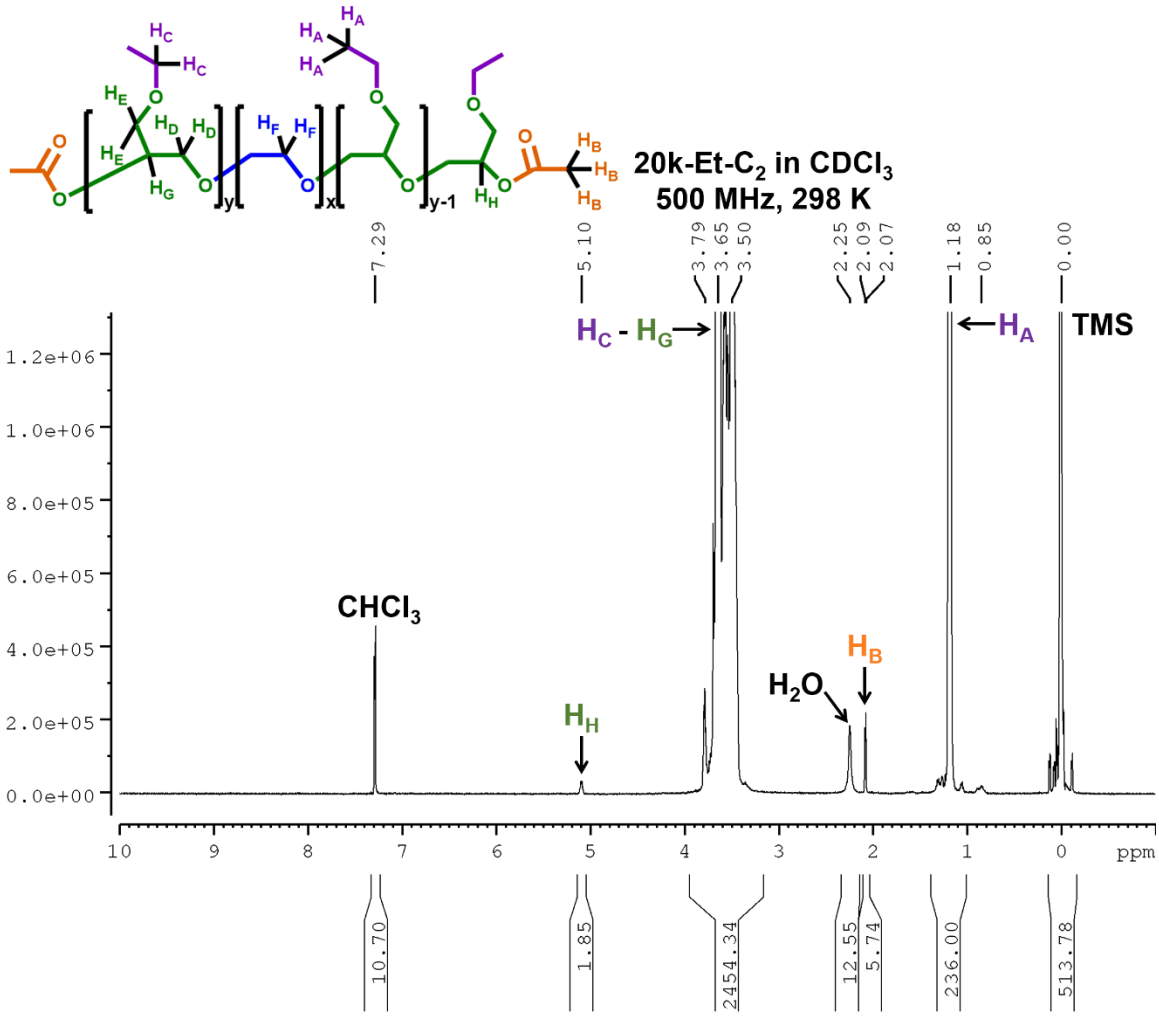

Figure 3.12. ^{1}H NMR spectrum of 20k-Et-C_2 in $CHCl_3$

500 MHz / T = 298 K

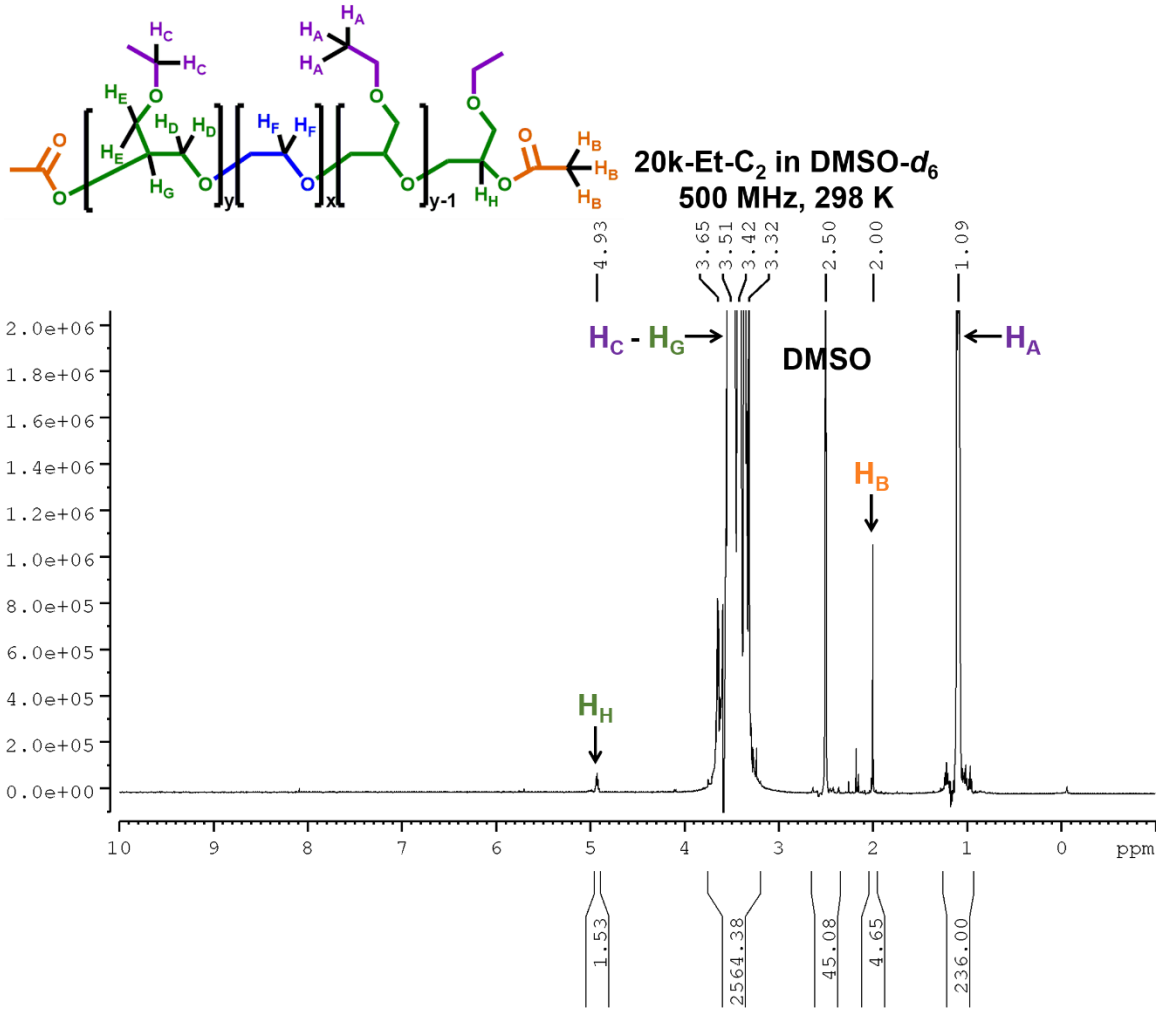

Figure 3.13. ^{1}H NMR spectrum of 20k-Et-C_2 in DMSO-d_6

500 MHz / T = 298 K

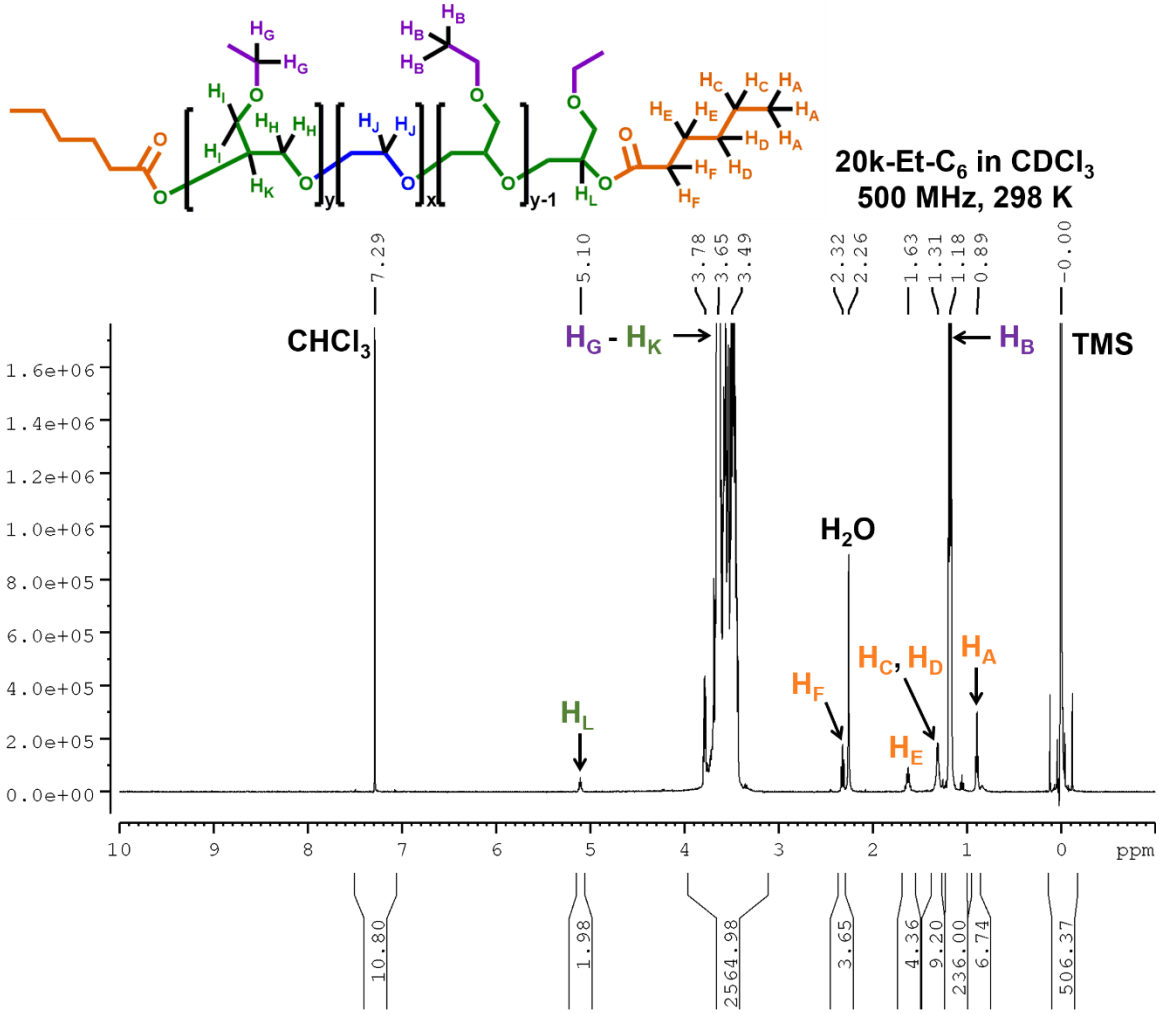

Figure 3.14. ^{1}H NMR spectrum of 20k-Et-C_6 in $CHCl_3$

500 MHz / *T* = 298 K

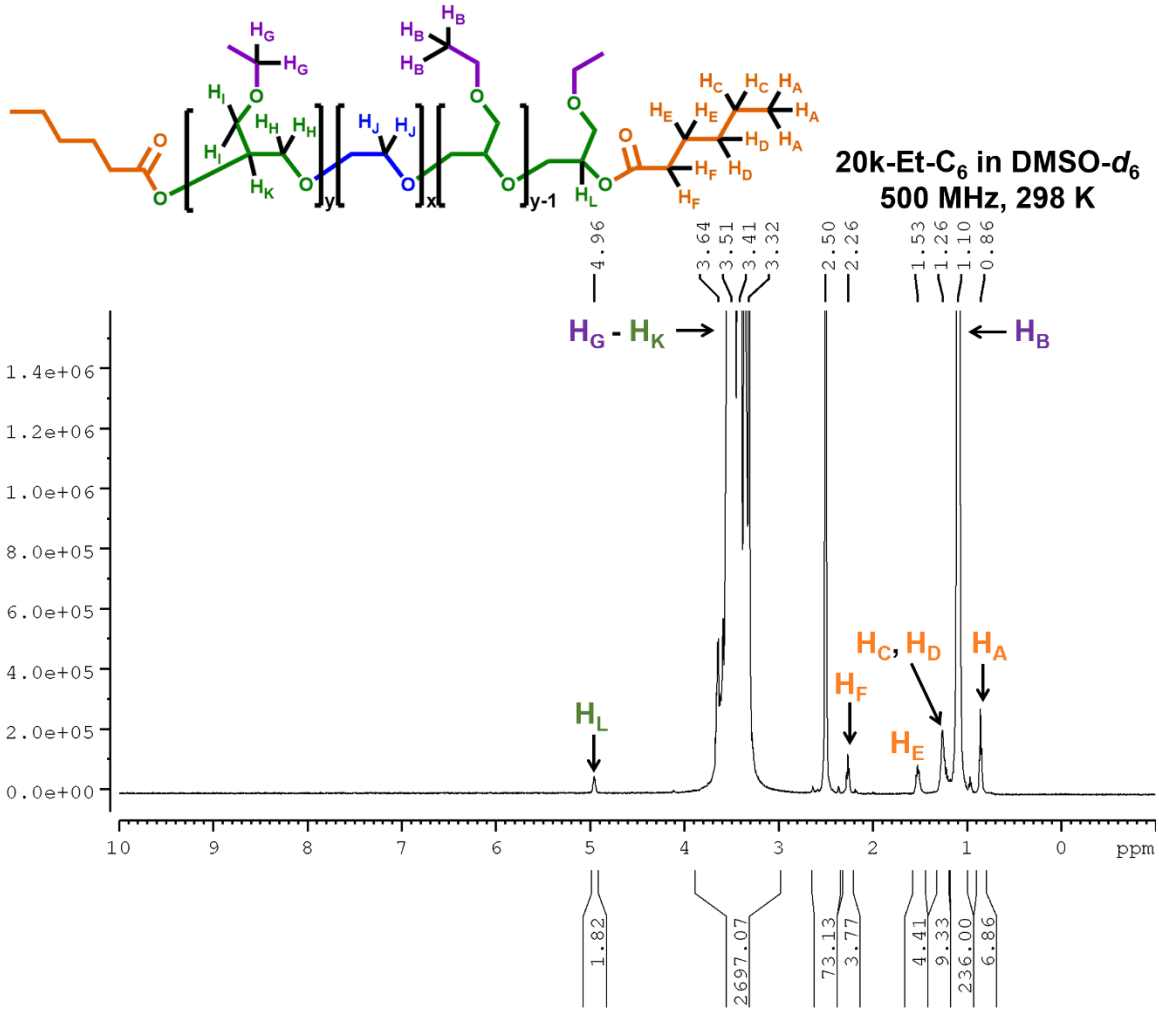

Figure 3.15. ^{1}H NMR spectrum of 20k-Et-C_6 in DMSO-d_6
500 MHz / T = 298 K

3.4.3 *Synthesis of 20k-Et-C_{7Ar} Polymer*

Prior to functionalization, an oven-dried RBF was charged with 1.0 eq of 20k-Et-OH polymer and a Teflon-coated magnetic stir bar. The flask was evacuated, then backfilled with N_2 a total of three times. Polymer was then dried at RT under reduced pressure for 45 h. The RBF was subsequently heated to 50 °C in a PDMS bath and dried under reduced pressure for an additional 20 h.

Under N_2 atmosphere, the dried polymer was dissolved in three-quarters the final target volume of CH_3CN (dried over anhydrous $MgSO_4$ at RT). NEt_3 (10 eq, distilled from CaH_2) was added *via* oven-dried syringe needle to the dissolved polymer. Benzoyl chloride (105 eq, TCI America, >98.0%) was mixed with the remaining one-quarter final volume of CH_3CN. The polymer/NEt_3 solution was cooled to 0 °C in a water/ice bath. Diluted benzoyl chloride was then added dropwise *via* addition funnel to the polymer/NEt_3 at 0 °C at a rate of ~1.5 mL min^{-1}. The reaction mixture was maintained at 0 °C for 10 min, then warmed to 35 °C in a PDMS bath and stirred for 22 h. At all times, the reaction mixture was kept under positive N_2 pressure.

The solvent was removed *in vacuo*, and the residue was stirred in excess Et_2O (~50 mL per gram of polymer) at RT for 20 min, then centrifuged. The supernatant was discarded, and the pelleted polymer was rinsed twice with fresh Et_2O. Recovered polymer was dried for 15 min at RT and ambient pressure, then dried at RT under reduced pressure for another 15 min. Dried polymer was reconstituted in CH_2Cl_2 to a final concentration of 7% w/v. In a separatory funnel, the CH_2Cl_2 layer was extracted three times with 10-mL portions of 0.01 M HCl, then once with brine (saturated NaCl solution). Next, the CH_2Cl_2 layer was dried over anhydrous $MgSO_4$ overnight. The following day, the dried CH_2Cl_2 solution was vacuum-filtered, then concentrated *in vacuo*. Recovered residue was stirred in excess Et_2O for 30 min, then centrifuged. The supernatant was discarded, and the solid polymer was washed once with fresh Et_2O. Finally, the polymer was dried at RT and ambient pressure for 30 min, then at RT under reduced pressure for at least 24 h to afford 20k-Et-C_{7Ar}. Degree of functionalization was estimated by ^{1}H NMR in DMSO-d_6 as described in section 3.4.5. f_n = 88% by chain-end methyne shift. f_n = 80-86% (mean = 82%) by integration against PEGE ethyl side chains.

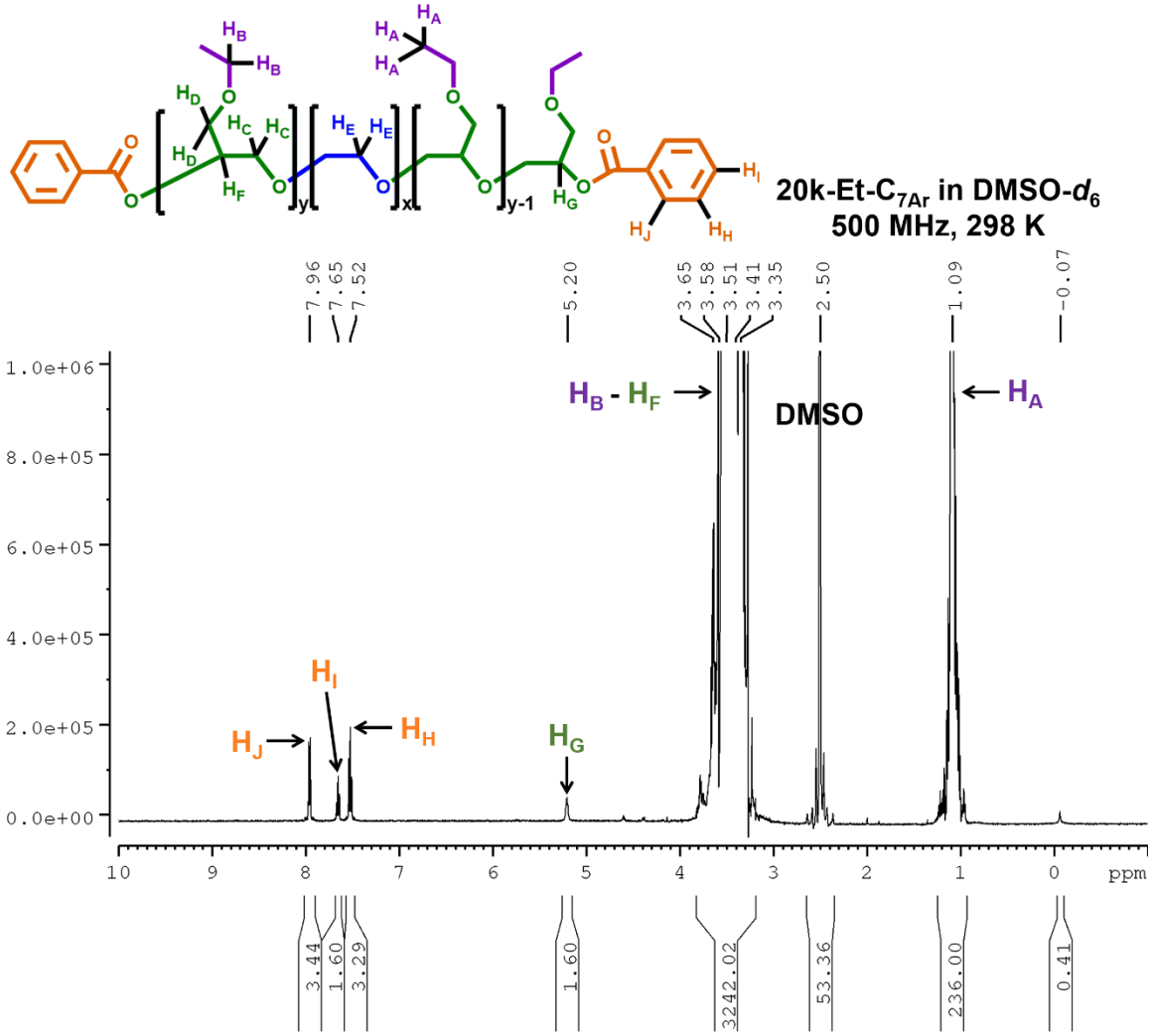

Figure 3.16. ^{1}H NMR spectrum of 20k-Et-C_{7Ar} in DMSO-d_6

500 MHz / T = 298 K

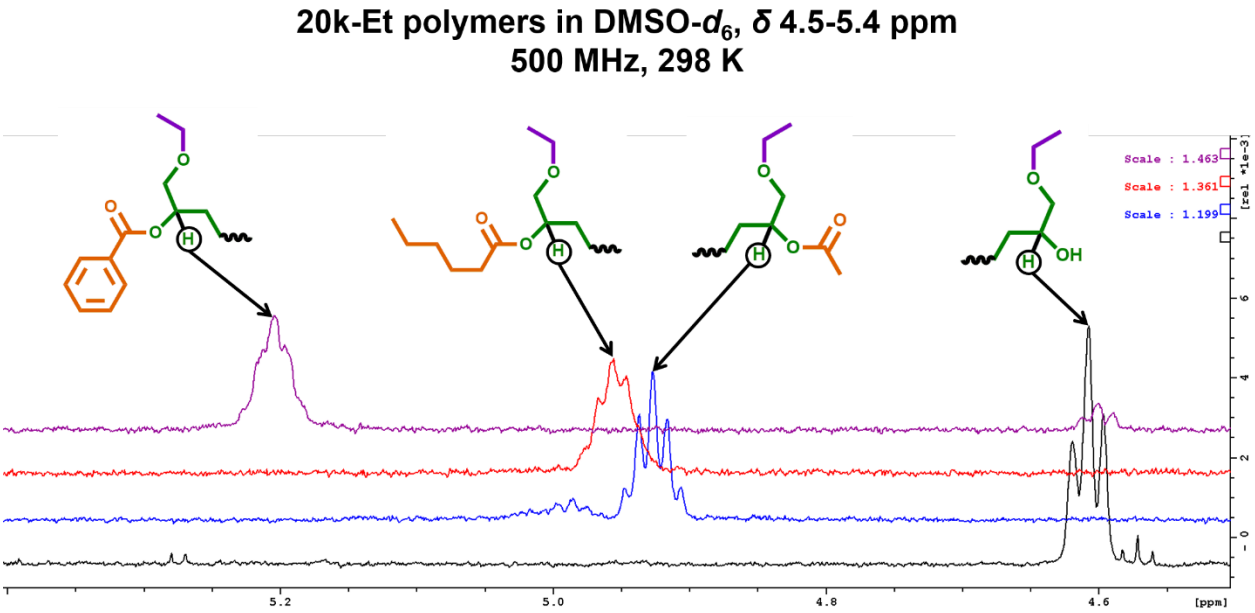

Figure 3.17. Overlaid 20k-Et ^{1}H NMR spectra in DMSO-d_6

Note the downfield shift of the chain-end methyne proton after esterification. Also note the presence of a residual OH methyne peak in the C_{7Ar} spectrum (top, purple). 500 MHz / T = 298 K

3.4.4 *Estimation of DP by ^{1}H NMR Spectroscopy*

Let 'x' equal the integration per proton for EGE. Let 'y' equal the integration per proton for PEO. Using Figure 3.10 as a sample spectrum, this gives the equations $3x = 1$ for the 3 protons that contribute to the ethyl resonance at 1.18 ppm, and $4y + 7x = 10.06$ for the 4 PEO protons and 7 EGE protons that contribute to the poly(ether) backbone resonances between 3.3-3.9 ppm. Solving these equations yields:

$$x = \frac{1}{3} \quad y \sim 1.93$$

Which gives the PEO:PEGE molar ratio:

$$\frac{y}{x} \sim 5.80$$

With a known M_n for PEO of 20.0 kg mol^{-1} and the monomer mass of ethylene oxide (44.05 g mol^{-1}), the average number of PEO repeat units is:

$$\frac{20{,}000}{44.05} \sim 454$$

Dividing this by the ratio of PEO to PEGE, we obtain the total repeat units of EGE:

$$\frac{454}{5.80} \sim 78.3$$

Or 39.2 repeat units per PEGE block, rounded down to 39.

3.4.5 *Estimation of f_n by ^{1}H NMR Spectroscopy*

The efficiency of esterification reactions for the 20k-Et-C_2, 20k-Et-C_6, and 20k-Et-C_{7Ar} polymers was estimated by ^{1}H NMR spectroscopy using two techniques. In the first technique, the polymer chain-end methyne proton for the esterified chain ends (δ 4.9-5.2 ppm, DMSO-d_6) was integrated against the methyne proton for the free (hydroxyl) chain end (δ 4.6 ppm, DMSO-d_6). Taking the 20k-Et-C_{7Ar} polymer as an example:

$$\frac{1.60\ (integration\ of\ ester\ chain\ end)}{1.60 + 0.227\ (integration\ of\ hydroxyl\ chain\ end)} \times 100 \sim 88\%$$

For the 20k-Et-C_2 and 20k-Et-C_6 polymers, no methyne proton corresponding to the hydroxyl chain end was present, suggesting quantitative chain-end functionalization (Figure 3.17).

In the second technique, the chain-end methyne and alkyl/aryl protons were normalized to the integration of the EGE ethyl protons (δ 1.18 ppm, $CDCl_3$). Using the known DP (39.2) of the PEGE blocks, the EGE ethyl resonance was calibrated to *39.2 x 2 x 3 = 235* or *236*, depending on small variations in integrations and rounding. Using the 20k-Et-C_2 polymer as an example (Figure 3.12), this normalization resulted in integrations of 1.85 for the chain-end methyne proton (δ 5.1 ppm, $CDCl_3$) and 5.74 for the acetyl protons in the end group (δ 2.08 ppm, $CDCl_3$). Dividing by the theoretical integrations of 2 and 6, respectively, gave an estimate of f_n = 93-96%.

3.4.6 *Vial-Inversion Phase Diagrams*

Polymers were dissolved in deionized (DI) water at a range of concentrations between 1-30 wt%. First, the appropriate mass of polymer was weighed into a clean glass vial. DI water was then added by syringe. Solutions were stirred at 0 °C in a water ice bath for 1-2 h, then incubated at 5 °C in a refrigerator for at least 18 h, until the solutions were transparent, and no trace polymer was visible. To construct phase diagrams, vials were rubber-banded together, then submersed in a water bath. Vials were maintained at each temperature for 5 min, then quickly inverted for several seconds to determine the physical state of the sol/gel. The “viscous” classification is subjective; the objective differences in the phase diagram are between formulations that flowed when inverted (“liquid” and “viscous”) and those that did not (“gel”).

3.4.7 *Rheometric Experiments*

All rheometric experiments were performed using a TA Instruments Discovery HR-2 hybrid rheometer with a Peltier temperature control accessory. All experiments used a 20 mm

parallel-plate geometry, except for the shear rate sweep experiments, which used a 40 mm cone-and-plate geometry (1.019° cone angle) to compensate for differential shear across the sample. All tests were carried out at least three times to ensure reproducibility, except for the shear rate sweeps. All tests were performed at 30 °C, except for the temperature-ramp experiments.

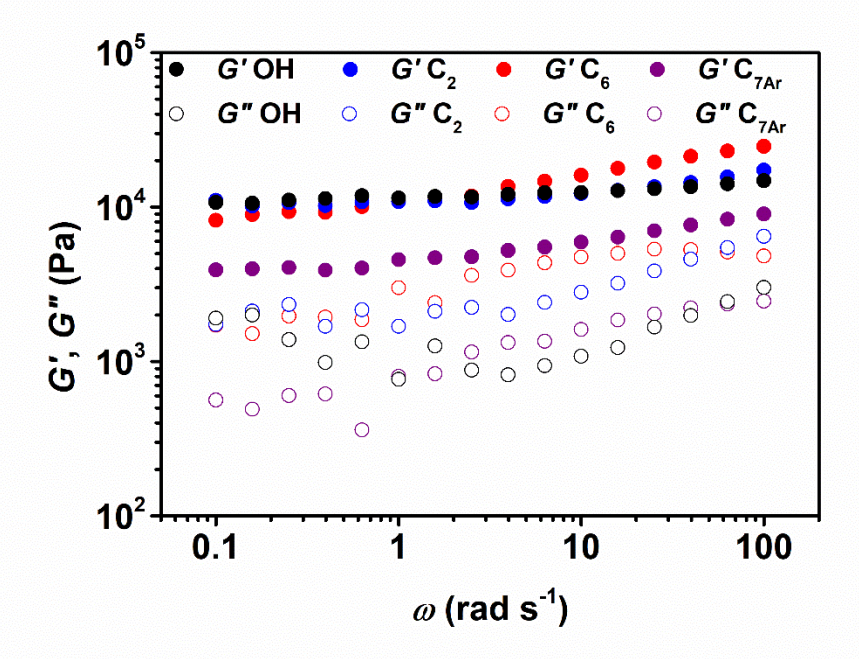

Figure 3.18. Frequency sweeps for 20k-Et hydrogels
Frequency amplitude sweeps were conducted for 20 wt% hydrogels at 30 °C.

3.4.8 *WAXS Experiments*

WAXS scattering plots were obtained under reduced pressure using a laboratory beamline system (Xeuss 2.0; Xenocs, Inc.) with an X-ray wavelength of 1.54 Å and a sample-to-detector distance of 15 cm. Images were collected on a Pilatus 1M detector (Dectris, Inc.) and processed using the Nika software package, along with WAXStools (Wavemetrics Igor Pro). Scattering plots were obtained for each of the 20k-Et polymer formulations as powders under vacuum.

3.4.9 *SAXS Experiments*

SAXS scattering plots were obtained under ambient pressure using a laboratory beamline system (Xeuss 2.0; Xenocs, Inc.) with an X-ray wavelength of 1.54 Å, an exposure time of 2 h, and a sample-to-detector distance of 2 or 4 m. Diffraction images were collected on a Pilatus 1M detector (Dectris, Inc.), then processed using the Nika software package, along with WAXStools (Wavemetrics Igor Pro). Scattering plots were obtained for each of the 20k-Et polymer formulations as 20% w/w hydrogels under ambient pressure to minimize evaporation. Plots of scattering intensity (*I*) *vs.* scattering vector (*q*, $Å^{-1}$) showed that all gel formulations had a characteristic periodicity of 20-21 nm, according to the equation $2\pi / q$, where *q* is the scattering vector at the apex of the first correlation peak.

3.4.10 *Statistical Analysis*

Data reported with error bars are the mean ± standard deviation. Statistically significant differences were determined *via* one-way analysis of variance (ANOVA) followed by pairwise *f*-tests and two-tailed Student's *t*-tests.

3.5 REFERENCES

(1) Schild, H. G. Poly (N-Isopropylacrylamide): Experiment , Theory and Application. *Prog. Polym. Sci.* **1992**, *17* (2), 163–249.

(2) Bakarich, S. E.; Gorkin, R.; Panhuis, M. In Het; Spinks, G. M. 4D Printing with Mechanically Robust, Thermally Actuating Hydrogels. *Macromol. Rapid Commun.* **2015**, *36* (12), 1211–1217.

(3) Priya James, H.; John, R.; Alex, A.; Anoop, K. R. Smart Polymers for the Controlled Delivery of Drugs – a Concise Overview. *Acta Pharm. Sin. B* **2014**, *4* (2), 120–127.
(4) Jochum, F. D.; Theato, P. Temperature- and Light-Responsive Smart Polymer Materials. *Chem. Soc. Rev.* **2013**, *42* (17), 7468–7483.
(5) Aseyev, V.; Tenhu, H.; Winnik, F. M. Non-Ionic Thermoresponsive Polymers in Water. *Adv. Polym. Sci.* **2011**, *242* (1), 29–89.
(6) Basu, A.; Saha, A.; Goodman, C.; Shafranek, R. T.; Nelson, A. Catalytically Initiated Gel-in-Gel Printing of Composite Hydrogels. *ACS Appl. Mater. Interfaces* **2017**, *9* (46), 40898–40904.
(7) Millik, S. C.; Dostie, A. M.; Karis, D. G.; Smith, P. T.; McKenna, M.; Chan, N.; Curtis, C. D.; Nance, E.; Theberge, A. B.; Nelson, A. 3D Printed Coaxial Nozzles for the Extrusion of Hydrogel Tubes toward Modeling Vascular Endothelium. *Biofabrication* **2019**, *11* (4), 045009(1-11).
(8) Kolesky, D. B.; Truby, R. L.; Gladman, A. S.; Busbee, T. A.; Homan, K. A.; Lewis, J. A. 3D Bioprinting of Vascularized, Heterogeneous Cell-Laden Tissue Constructs. *Adv. Mater.* **2014**, *26* (19), 3124–3130.
(9) Aoki, S.; Koide, A.; Imabayashi, S.; Watanabe, M. Novel Thermosensitive Polyethers Prepared by Anionic Ring-Opening Polymerization of Glycidyl Ether Derivatives. *Chem. Lett.* **2002**, *31* (11), 1128–1129.
(10) Ogura, M.; Tokuda, H.; Imabayashi, S. I.; Watanabe, M. Preparation and Solution Behavior of a Thermoresponsive Diblock Copolymer of Poly(Ethyl Glycidyl Ether) and Poly(Ethylene Oxide). *Langmuir* **2007**, *23* (18), 9429–9434.
(11) Isono, T.; Miyachi, K.; Satoh, Y.; Sato, S.; Kakuchi, T.; Satoh, T. Design and Synthesis of Thermoresponsive Aliphatic Polyethers with a Tunable Phase Transition Temperature. *Polym. Chem.* **2017**, *8*, 5698–5707.
(12) Heinen, S.; Rackow, S.; Schäfer, A.; Weinhart, M. A Perfect Match: Fast and Truly Random Copolymerization of Glycidyl Ether Monomers to Thermoresponsive Copolymers. *Macromolecules* **2017**, *50* (1), 44–53.
(13) Fellin, C. R.; Adelmund, S. M.; Karis, D. G.; Shafranek, R. T.; Ono, R. J.; Martin, C. G.; Johnston, T. G.; DeForest, C. A.; Nelson, A. Tunable Temperature- and Shear-Responsive Hydrogels Based on Poly(Alkyl Glycidyl Ether)S. *Polym. Int.* **2019**, *68* (7), 1238–1246.
(14) Imbrogno, J.; Ferrier, R. C.; Wheatle, B. K.; Rose, M. J.; Lynd, N. A. Decoupling Catalysis and Chain-Growth Functions of Mono(μ-Alkoxo)Bis(Alkylaluminums) in Epoxide Polymerization: Emergence of the N-Al Adduct Catalyst. *ACS Catal.* **2018**, *8* (9), 8796–8803.
(15) Manoravi, P.; Joseph, M.; Sivakumar, N. Pulsed Laser Ablation - Thin Film Deposition of Polyethylene Oxide. *J. Phys. Chem. Solids* **1998**, *59* (8), 1271–1277.
(16) Lazzara, G.; Milioto, S.; Gradzielski, M.; Prevost, S. Small Angle Neutron Scattering, X-Ray Diffraction, Differential Scanning Calorimetry, and Thermogravimetry Studies to Characterize the Properties of Clay Nanocomposites. *J. Phys. Chem. C* **2009**, *113* (28), 12213–12219.
(17) Innocenzi, P.; Malfatti, L.; Marcelli, A.; Piccinini, M. Evaporation-Induced Crystallization of Pluronic F127 Studied in Situ by Time-Resolved Infrared Spectroscopy. *J. Phys. Chem. A* **2010**, *114* (1), 304–308.

Chapter 4. 3D BIOPRINTING OF MECHANICALLY TUNED BIOINKS DERIVED FROM CARDIAC DECELLULARIZED EXTRACELLULAR MATRIX

4.1 ABSTRACT

3D bioprinting is a powerful technique for engineering tissues used to study cell behavior and tissue properties *in vitro*. With the right formulation and printing parameters, bioinks can provide native biological and mechanical cues while allowing for versatile 3D structures that recapitulate tissue-level organization. Bio-based materials that support cellular adhesion, differentiation, and proliferation - including gelatin, collagen, hyaluronic acid, and alginate - have been successfully used as bioinks. In particular, decellularized extracellular matrix (dECM) has become a promising material with the unique ability to maintain both biochemical and topographical micro-environments of native tissues. However, dECM has shown technical limitations for 3D printing (3DP) applications posed by its intrinsically low mechanical stability. Herein, we report hydrogel bioinks composed of partially digested, porcine cardiac decellularized extracellular matrix (cdECM), Laponite-XLG nanoclay, and poly(ethylene glycol)-diacrylate (PEG-DA). The Laponite facilitated extrusion-based 3DP, while PEG-DA enabled photo-polymerization after printing. Improving upon previously reported bioinks derived from dECM, our bioinks combine extrudability, shape fidelity, rapid cross-linking, and cytocompatibility in a single formulation (> 97% viability of encapsulated human cardiac fibroblasts and > 94% viability of human induced pluripotent stem cell derived cardiomyocytes after 7 days). The compressive modulus of the cured hydrogel bioinks was tunable from 13.4-89 kPa by changing the concentration of PEG-DA in the bioink formulation. Importantly, this span of mechanical stiffness

encompasses ranges of tissue stiffness from healthy (compressive modulus ~5-15 kPa) to fibrotic (compressive modulus ~30-100 kPa) cardiac tissue states. The printed constructs demonstrated shape fidelity, adaptability to different printing conditions, and high cell viability following extrusion and photo-polymerization, highlighting the potential for applications in modeling both healthy and fibrotic cardiac tissue.

4.2 INTRODUCTION

3D bioprinting technologies enable the fabrication of tissue-like constructs that aim to replicate the complexity of biological systems. These digital manufacturing processes can take advantage of imaging techniques such as CT and MRI scans to create computer-aided design (CAD) files. The digital files provide the blueprint for 3D bioprinters to fabricate a desired tissue construct. Therefore, the growth of the 3D bioprinting field provides opportunities to employ this technology for *in vitro* disease modeling. Such models could be utilized for applications in drug screening, disease mechanism research, and pre-clinical studies in the tissue of interest.[1–10]

Recent advances in bioinks for 3D bioprinting have sought to modify the biochemical and mechanical properties of the bioink matrix for *in vitro* disease modeling and tissue engineering.[4,11,20–24,12–19] However, an existing challenge in the field is the balance between the rheological properties required for printing and the physicochemical properties required of the printed matrix. The complex relationship between rheological parameters, printability, and cell viability has been recently reviewed[25,26] for common 3D bioprinting techniques, including inkjet printing and micro-extrusion. For extrusion-based 3DP, one of the most important properties of a bioink is shear-thinning behavior, in which the material flows under high shear stress but maintains a significantly higher viscosity under low-shear conditions (“at rest”).[27,28] In addition, the

viscoelastic properties of the bioinks have been shown to be critical for maintaining cell viability during the printing process.[29–31]

Conventionally, both natural hydrogel materials (gelatin,[32–34] collagen,[4,33] hyaluronic acid,[32,35,36] alginate[37–39]) and synthetic hydrogels (poly(lactic acid),[40] PEG-DA,[41,42] Pluronic F127[43–45]) have been popular choices for bioinks. Synthetic hydrogels exhibit good gelation kinetics and mechanical tunability, which is advantageous for bioprinting. However, these materials lack the ability to closely mimic the biological cues of the native ECM micro-environment. On the other hand, naturally derived hydrogels have the ability to emulate tissue micro-environments through their biophysical and biochemical properties but can be more challenging to tune with respect to their viscoelastic properties during the printing process and the mechanical properties that arise after printing. Among the naturally derived hydrogels, dECM-derived bioinks have attracted significant attention for their enhanced tissue functionality, which is unmatched by other hydrogels. dECM bioinks are unique in that they preserve some of the growth factors, extracellular matrix (ECM) proteins, and glycosaminoglycans (GAGs) specific to the source tissue. Previous studies have demonstrated 3DP of dECM bioinks derived from a variety of sources including liver,[32,46,47] heart,[46,48,49] kidney,[10,50] cartilage,[51,52] adipose,[48] and tendons.[53] However, similar to other naturally derived hydrogels, dECM gels are marked by a lack of mechanical and structural stability (with compressive, tensile, or shear moduli < 1 kPa), which is lost during both the decellularization and digestion processes.[48] Recent work has focused on tailoring the mechanical properties of dECM-based bioinks to match the properties of a particular tissue. For example, one recent study reported the improvement of mechanical stability through a two-step gelation process requiring both temperature control and UV cross-linking using vitamin B to engineer a physiologically relevant cardiac tissue compressive modulus (~15 kPa).[52]

While multiple approaches have enabled dECM-based bioinks to recapitulate the modulus of native cardiac tissues, current methods have not fully investigated strategies for modeling diseased cardiac tissues, which manifest a higher tissue stiffness (compressive modulus between 30-100 kPa).[54,55] For instance, cardiac fibrosis is one of the hallmarks of cardiac disease, accompanied by many cardiomyopathies such as hypertrophic cardiomyopathy, idiosyncratic dilated cardiomyopathy, and myocardial infarction.[56] Therefore, introducing technologies to recapitulate mechanical properties of fibrotic cardiac tissue in 3D platforms is valuable for modeling cardiac diseases. A key event in cardiac fibrosis, a process marked by disproportionate deposition of collagen and abnormal proliferation of fibroblasts, is the differentiation of fibroblasts to myofibroblasts.[57–59] While many factors influence activation of myofibroblasts, one of the most important is substrate stiffness.[60–63] However, the mechanism by which myofibroblasts recognize and respond to substrate elasticity is not well understood. Therefore, there is a need to develop *in vitro* systems with precisely tunable mechanical properties that mimic the extracellular environment.

Herein, we report a cdECM-based bioink that has been modified with Laponite and PEG-DA to afford bioinks that can be extrusion-printed to fabricate constructs with tunable mechanical properties. To the best of our knowledge, this is the first report of a bioink that uses dECM, Laponite, and PEG-DA concurrently to afford a single bioink capable of extrusion and rapid photo-polymerization. This naturally derived bioink can print without supports, cure quickly, and promote high viability of encapsulated cells. To date, there are few examples of dECM-derived bioinks that can be photo-cross-linked in 1 minute or less while simultaneously preserving shape fidelity and cell viability. Specifically, we show that the desired mechanical stiffness of cross-linked cdECM bio-constructs can be achieved by varying the concentration of PEG-DA, covering

all physiological compressive stiffness ranges from healthy (5-15 kPa) to pathological (30-100 kPa) conditions. Additionally, Laponite has been shown to provide necessary rheological properties[64] and print fidelity[65–68] while providing the biocompatibility that is crucial for bioinks.[69] Therefore, our bioinks satisfy the need for high-stiffness bio-constructs without sacrificing biocompatibility or the capacity to fabricate complex 3D structures. Our work improves upon a previous report[48] in which dECM-based bioinks, both with and without living cells, were extrusion printed into a poly(caprolactone) support framework, then thermally cured at 37 °C for 30 minutes. In particular, the current strategy eliminates the need for both support frameworks and long thermal gelation periods by adding Laponite to facilitate stacking of filaments and PEG-DA to promote rapid photo-polymerization (1 minute or less). Other bioinks require support frameworks or fugitive inks (like Pluronic F127) for mechanical reinforcement,[70,71] while our bioinks are free-standing and self-supporting. Our bioinks cross-link rapidly and irreversibly due to the photo-polymerization of PEG-DA, while bioinks that use alginate[70–72] or dECM without a photo-cross-linker[71] require replenishment of exogenous cations to preserve cross-linking interactions or long thermal curing times that may result in loss of shape fidelity. Finally, our bioinks require mild processing and printing conditions, in contrast to bioink formulations that require higher extrusion pressures (like collagen, ECM, and tannic acid[73]) or freeze-drying, harsh chemical cross-linking, and solvent treatment.[74] Whereas harsh processing and printing conditions are acceptable for applications wherein cells are seeded onto printed constructs, it is critical to avoid conditions that cause cell death for bioinks with encapsulated cells. Overall, the all-in-one bioinks reported herein simplify the extrusion-printing process, requiring no support frameworks, no long gelation periods, and no harsh chemical treatments or printing pressures that damage embedded cells.

With the ability to rapidly photo-polymerize filaments, 3D-printed constructs maintain structural integrity in contrast to constructs that are cured slowly, which often collapse due to destabilization of the underlying layers. Furthermore, varying the concentration of PEG-DA affords more precise control over the final stiffness of printed constructs compared to thermal gelation. Through incorporation of both Laponite and PEG-DA, we show that the printed cdECM bio-constructs have the potential to be used for disease modeling of cardiac fibrosis by controlling the mechanical properties to afford compressive moduli that mimic both native and diseased cardiac tissue. Additionally, the cdECM bioinks demonstrate high cell viability of human cardiac fibroblasts, with > 97% viable cells after 7 days. These are promising results for the fabrication of functional 3D-printed constructs containing active cardiac cells.

4.3 Results and Discussion

4.3.1 *Preparation of Composite cdECM-Laponite-PEG-DA Bioinks*

Fabrication and printing of the cdECM bioink required multiple processing steps (Figure 4.1). Initially, left ventricular tissues harvested from porcine hearts were decellularized with chemical detergents to effectively remove cellular components and to preserve the cardiac ventricular ECM. The cdECM harbors many of the biophysical and biochemical cues present in the native cardiac micro-environment and therefore provides some of the crucial intrinsic features (*i.e.* morphological similarities, specific cell-matrix interactions, tissue specificity) that cannot be replicated by other materials.[78,79] We have previously shown that porcine cardiac tissues could be effectively decellularized (~98% removal of cellular content) while maintaining major ECM components (such as collagen and GAGs) using a combination of chemical detergents: 1% SDS

and 1% Triton X-100.[48,80] The cdECM was then digested with gastric pepsin at low pH to create a concentrated, soluble form of cdECM that could be utilized in the extrudable composite bioinks.

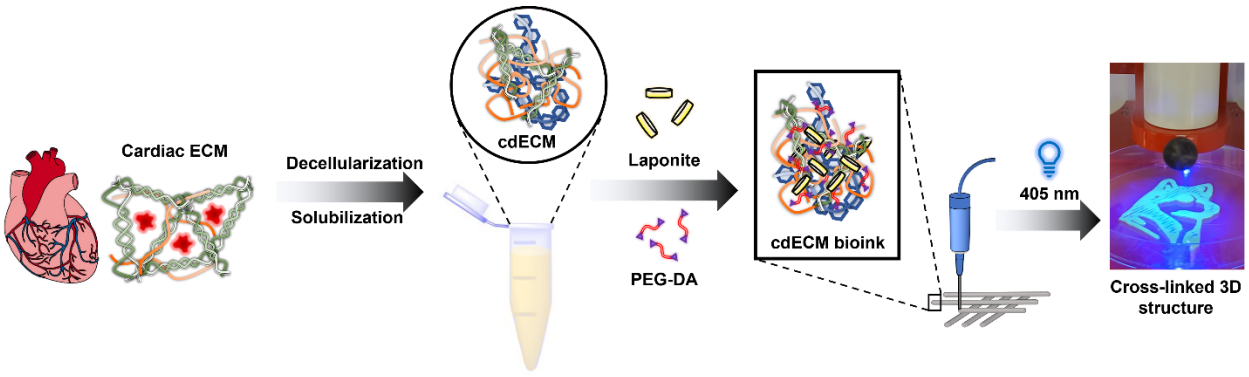

Figure 4.1. Overview of cdECM bioink preparation

Schematic overview of the fabrication and printing of engineered cdECM bioinks. Fabrication of the bioink involved decellularization and solubilization of cardiac tissues into pre-gels which were modified with Laponite to afford a viscoelastic bioink capable of providing a high-fidelity print. Incorporation of the cross-linker PEG-DA and a photo-initiator, lithium phenyl-2,4,6-trimethylbenzoylphosphinate, allowed tunable mechanical properties by changing PEG-DA concentration.

An important consideration throughout optimization of the bioink included the ability for the hydrogel to maintain its shape after extrusion. To date, one of the challenges of using dECM-based bioinks has been the poor intrinsic mechanical properties – such as low modulus, viscosity, and yield stress – which prevent a high-fidelity print, especially in the *z*-direction. Our formulation with 4.6% cdECM alone was too low in shear modulus and viscosity to be suitable for extrusion-based 3DP. To address this challenge, we introduced a clay-based bioceramic, Laponite-XLG, to enhance the printability of the bioink. Laponite, a disc-like crystalline colloid, has been previously used for modification of rheological properties.[64,81] Studies showed that incorporation of Laponite enabled high print fidelity and exhibited the biocompatibility required for bioinks.[72] Combining rheological experiments (section 4.3.2) with qualitative manual extrusion, it was determined that

a concentration of 2.3% w/w Laponite was sufficient to impart the desired rheological properties to the cdECM bioink.

Furthermore, the tunability of mechanical properties - *via* introduction of cross-linking agents - can afford a wider array of bioinks for engineering stiffness. In cardiac tissue, the myocardium stiffness is regulated by different cardiac cellular subtypes such as cardiomyocytes, cardiac fibroblasts, and endothelial cells that regulate the ECM. Therefore, the interplay between resident cardiac cells and paracrine signaling within their micro-environment can result in modification of ECM stiffness. In particular, various forms of cardiac myopathies that lead to inflammation and scar tissue formation, such as myocardial infarction and ventricular ischemia, can trigger progressive fibrosis and excessive deposition of ECM. Many cdECM based bioink studies have so far recapitulated the tissue stiffness of the healthy myocardium (compressive; ~5-15 kPa) through thermal and photo-initiated cross-linking but have not emulated the material stiffness required for modeling cardiac diseases that are closely associated with tissue ECM stiffness. To address this issue, we incorporated different concentrations of a PEG-DA cross-linker to afford constructs with a range of stiffness following photo-polymerization. Iterative rheological photo-curing (section 4.3.3) was used to determine the range of PEG-DA concentrations that could accurately represent the stiffness of different cardiac disease states.

4.3.2 *Rheological Characterization of cdECM-Laponite-PEG-DA Bioinks*

With the necessary components of the bioinks in hand, we attempted to quantify printability using rheological experiments. For the remainder of the manuscript, bioink formulations are referred to by weight percentage, using the general formula cdECM-Laponite-PEG-DA%. To validate the use of each bioink component, we prepared a full range of six bioink

formulations: cdECM alone (4.6-0-0% w/w), cdECM with PEG-DA (4.6-0-6.0% w/w), cdECM with Laponite (4.6-2.3-0% w/w), and three "printable" formulations, each containing 4.6% w/w cdECM, 2.3% w/w Laponite, and 6.0, 8.25, or 10.5% w/w PEG-DA. For a bioink to be suitable for direct-write extrusion 3DP, it must exhibit several desirable viscoelastic properties. Some rheological parameters that have been shown to impact printability include yield stress, σ_y,[27,28,82,83] loss factor, tan δ (G''/G'),[84] and viscosity, η.[65,85] Specifically, bioinks with gel character ($G' > G''$) tend to exhibit high shape fidelity after extrusion-based 3DP. It is also important for such materials to be shear-thinning, which facilitates pneumatic extrusion. With these parameters in mind, three rheological experiments were performed on each cdECM bioink formulation. Each test was performed for each of the six different formulations, with comparisons made against the control 4.6-0-0% ink.

The first test was an oscillatory strain amplitude sweep from 0.01 to 100% strain (Figure 4.9 (a,b)). The primary purpose of this test was to determine the equilibrium shear moduli and to establish the linear viscoelastic region (LVR) for each formulation to ensure that all subsequent oscillatory measurements would occur without irreversible deformation. Based on this experiment, 1% strain was chosen as the standard for all subsequent oscillatory measurements. Additionally, the strain amplitude sweep allowed estimation of σ_y by calculating oscillatory stress from the applied strain and then plotting shear moduli *vs.* stress (Figure 4.2 (b)). Yield stresses were estimated by determining the onset point of G' decrease using regression techniques in Trios software (TA Instruments).

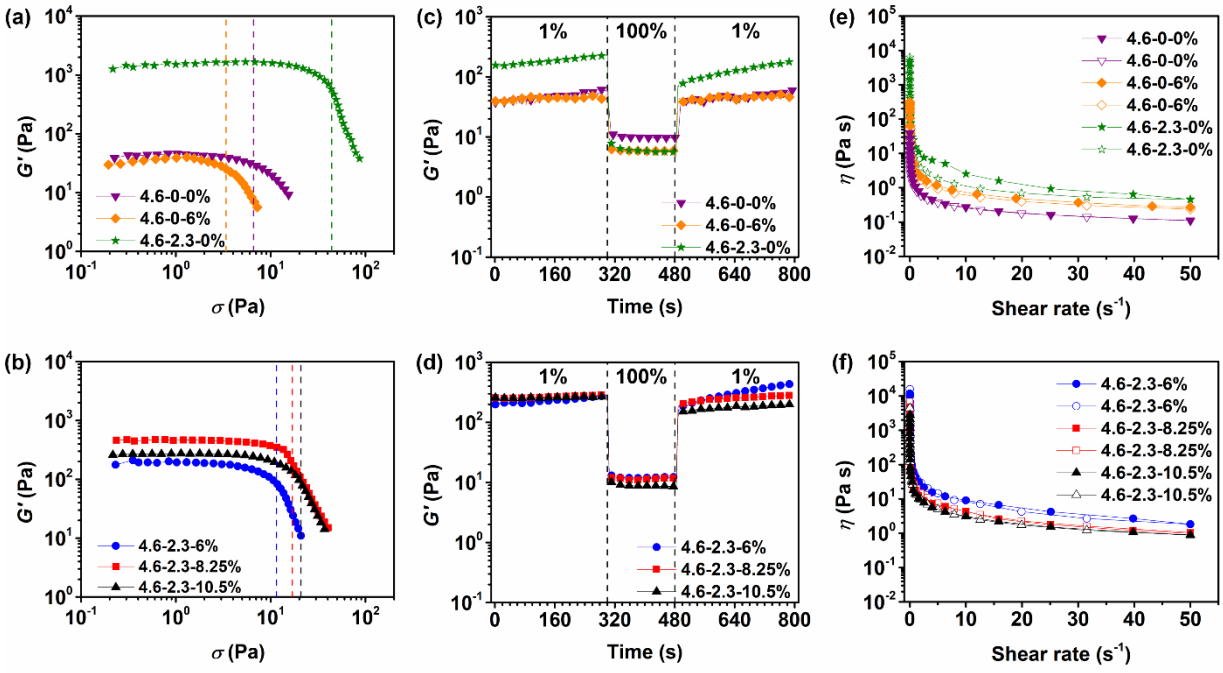

Figure 4.2. Rheometric characterization of cdECM composite bioinks

(a,b) Oscillatory stress sweep experiments conducted at 1 Hz angular frequency for (a) control formulations and (b) printable formulations. The onset of *G'* decrease was reported as the apparent yield stress, σ_y. The mean yield stress for each formulation is plotted as a dashed vertical line. All plots are the mean of 3 tests. (c,d) Dynamic oscillatory strain experiments conducted at 1 Hz angular frequency for (c) control formulations and (d) printable formulations. Strain amplitude alternated between 1 and 100%. All plots are the mean of 3-4 tests. (e,f) Plots of viscosity vs. shear rate for control formulations (e) and printable formulations (f) demonstrated the shear-thinning behavior and different viscosities of each formulation. Filled symbols indicate increasing shear rate, while open symbols indicate decreasing shear rate. All plots shown are the mean of 3-4 tests.

For viscoelastic gels, σ_y is a critical stress value below which any deformation is small and reversible.[86] Above σ_y, the gel network breaks down, the material flows and becomes deformed. Therefore, higher values for σ_y suggest better stackability of printed filaments in the *z*-direction and better shape fidelity.

There was only one statistically significant difference in σ_y (Figure 4.3 (c)) compared to the control formulation consisting only of cdECM (4.6-0-0%), likely due to difficulty with reproducibility of experiments. This makes it difficult to draw any conclusions about the effects of Laponite and PEG-DA on the σ_y values for the cdECM bioinks; however, the statistically significant difference ($p < 0.05$) between the 4.6-2.3-10.5% and 4.6-0-0% formulations, together with analysis of *G'* and tan δ, imply that Laponite may be responsible for any increase in the yield stress of the bioink. The effects of Laponite on the rheological characteristics of the bioink are discussed further in analysis of *G'* and tan δ.

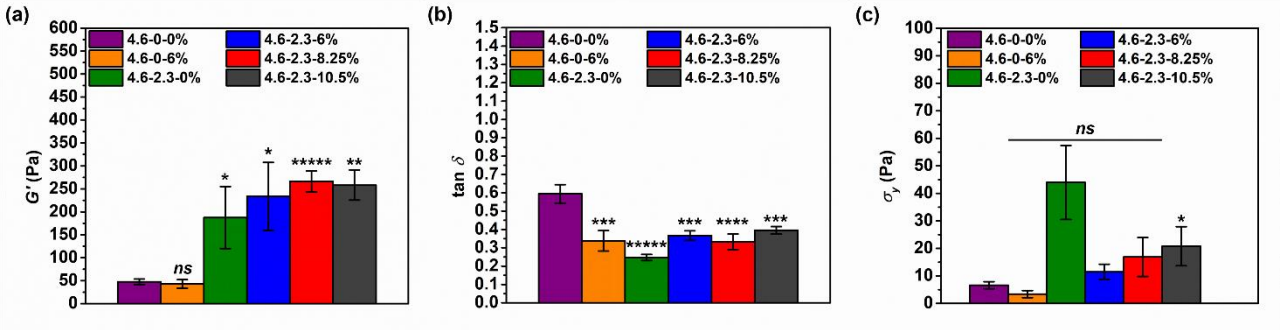

Figure 4.3. Laponite increases *G'* and decreases tan δ for cdECM composite bioinks
Statistically significant differences were determined via one-way analysis of variance (ANOVA), followed by pairwise *f*-tests and two-tailed Student's *t*-tests. All formulations were compared to the 4.6-0-0% bioink formulation as a control. Asterisks indicate significance levels: *$p < 0.05$; **$p < 0.01$; ***$p < 0.001$; ****$p < 0.0001$; *****$p < 0.00001$; *ns* = not significant. (a) Formulations containing Laponite exhibited significantly greater plateau *G'* values, largely due to the formation of a Laponite gel network. The addition of PEG-DA alone (4.6-0-6%, orange) had no significant effect on measured *G'* values. N = 4-5 for each measurement. (b) The loss factor, tan δ, was lower compared to the control (4.6-0-0%, purple) for all formulations. This is an expected result for inks containing Laponite, but somewhat unexpected for the 4.6-0-6% formulation. N = 4-5 for each measurement. (c) The yield stress, σ_y, showed too much variability in measurement to assess any significant differences; however, the trend appeared to be an increase in yield stress in the presence of Laponite. N = 3 for each measurement.

Next, dynamic oscillatory strain experiments (Figure 4.2 (c,d)), in which samples were subjected to alternating periods of 1% and 100% strain at constant angular frequency, were performed. These tests provided estimates of the shear storage and loss (*G"*) moduli, as well as the loss factor, tan δ. More importantly, the tests provided information about the mechanical recovery of inks following periods of high strain well outside of the LVR. The tests demonstrated that all formulations behave as low-modulus viscoelastic solids with $G' > G''$ and tan $\delta < 1$ under low-strain conditions, which are meant to model behavior of the inks at rest. At high strain, all formulations exhibited a rapid decrease in *G'* and tan $\delta > 1$, characteristic of fluid-like materials. Upon reversion to low strain, all formulations recovered nearly to the initial plateau value of *G'*. Many replicates showed a sloping curve for *G'* which made a plateau value difficult to estimate. Therefore, the exact time required for *G'* to reach the plateau value following high strain could not be determined. In general, formulations with Laponite were stiffer than those without, reflected by higher *G'* values (Figure 4.3 (a)). Indeed, *G'* was higher for all formulations compared to the cdECM alone, excluding the 4.6-0-6.0% formulation that did not contain Laponite. This is likely due to the formation of a non-covalent Laponite gel network. Laponite, a disc-like platelet composed of sodium-magnesium-lithium silicates, is known to bear a negative charge on the face of the disc and a positive charge on the edges. At concentrations above ~ 1% w/w in aqueous solution and at pH < 9, the platelets may aggregate to form a so-called "house-of-cards" gel network, with the positively-charged edges of one disc interacting with the negatively-charged face of another.[87,88] The pH of the cdECM bioinks was maintained at ~ 7.4, and the concentration of Laponite was 2.3% w/w, meaning conditions were favorable for the formation of an ionic gel network. It is almost certain that Laponite discs interact not only with themselves, but also with partially-digested cdECM proteins. Indeed, strong electrostatic interactions between Laponite and

collagen or type A gelatin[89–91] have been well-characterized. The additional structure afforded by Laponite and Laponite-protein networks increased the solid-like characteristics of the bioink by providing cross-links, thereby increasing the storage modulus and rendering the bioinks stiffer. PEG-DA alone (4.6-0-6.0% formulation) had no significant effect on *G'* compared to the control. This is unsurprising, given that the interaction between PEG-DA of relatively low molecular weight (M_n = 700 g mol^{-1}) and cdECM proteins is expected to be minimal. At this molecular weight, PEG is quite hydrophilic and does not present enough amphiphilic character to interact with hydrophobic residues in proteins.[92]

Moreover, non-cross-linked PEG-DA in water is not expected to self-assemble into a gel network. The values of tan δ for our cdECM bioinks were significantly lower for all formulations compared to the control formulation comprised solely of cdECM (Figure 4.3 (b)). This result is expected for inks containing Laponite, since the cross-linking interactions in the gel network impart a greater proportion of solid-like properties to the inks. As such, the ratio *G''* / *G'* becomes smaller. It is unclear why tan δ for the 4.6-0-6.0% formulation is significantly lower than the control, since PEG-DA is not expected to participate in any gel-network formation that could alter tan δ. It is possible that the observed effect is simply due to the slight reduction in water content for the 4.6-0-6.0% formulation compared to the control: The loose network of cdECM components occupies a slightly smaller volume of water and may not interact significantly with the PEG-DA, thereby increasing the measured solid-like behavior of the ink. Of course, if true, this reduction in water content could partially account for the reduction in tan δ for the other formulations as well. For bioinks that must be extruded and maintain shape fidelity, the value of tan δ should be between zero and one. Theoretically, inks with tan δ closer to one extrude uniformly and require only gentle pressure but exhibit poor shape fidelity and limited stackability. Inks with tan δ closer to zero are

robust and self-supporting but require higher printing pressures and may be too brittle to extrude uniformly. These observations are rationalized by considering the physical meaning of tan δ, which is an expression of the ratio of fluid, viscous behavior (G'') to solid, elastic behavior (G') in a viscoelastic material. If this ratio is ≥ 1, the material is mostly fluid and behaves correspondingly, meaning it tends to spread and flow and should not exhibit a yield stress. If the ratio is < 1, the material is mostly solid; this regime is typical for hydrogels. The closer tan δ is to 0, the more likely a material is to be self-supporting, but also more brittle due to the increased solid-like, elastic character of the material. Tan δ is also an important factor for measuring the glass transition temperature (T_g) of amorphous polymers *via* dynamic mechanical analysis: Below the T_g, tan $\delta << 1$, and the polymer is brittle, while at and above the T_g, tan δ increases to reflect rubbery, elastomeric character. Therefore, a bioink with tan $\delta \sim 1$ is likely to be fluid and runny, while a bioink with tan $\delta \sim 0$ is likely to be rigid and brittle. Using a gelatin-alginate bioink, Lee and co-workers[84] found that a range of tan δ values between 0.25-0.45 were optimal for balancing smooth extrusion, shape fidelity, and cell viability. Additionally, bioinks with relatively low moduli ($G' <$ 5 kPa) required lower extrusion pressure and were therefore better for cell viability. While these parameters were determined for a different bioink composition than the present study, it is nevertheless interesting to note that tan δ for each of our extrudable cdECM bioink formulations (*i.e.*, formulations containing all three components cdECM, PEG-DA, and Laponite) is between 0.25-0.45. Overall, the results of the dynamic strain experiments indicate that all inks are capable of mechanical recovery following deformation beyond the LVR, while inks containing Laponite are higher-modulus and lower in tan δ compared to the control cdECM-only formulation.

The shear-thinning behavior of the bioinks was evaluated by rotational shear rate sweep experiments (Figure 4.2 (e,f)). All ink formulations exhibited shear-thinning behavior, wherein the

viscosity decreased with increasing shear rate. Formulations without Laponite had relatively low viscosity (< 500 Pa·s) at low shear rates, while all formulations containing Laponite had viscosity above 5 000 Pa·s under low-shear conditions. The higher viscosity of the Laponite-containing inks (compared to the control cdECM-only formulation) might indicate more favorable printability. If the viscosity of an ink is too low, extruded filaments may spread or collapse upon contact with the printing stage or the previous layer of a printed object. However, to determine viscosity more accurately at a specific shear rate, it would be necessary to make repeated measurements at the shear rate of interest. Thus, the absolute values reported for viscosity may be inaccurate, although the trends between different formulations are expected to hold. Furthermore, the shear rate sweep experiments provided another estimate of σ_y. Indeed, flow curves of stress *vs.* shear rate (Figure 4.9 (e,f)) indicate that all ink formulations had a non-zero yield stress when fit to Herschel-Bulkley curves (fits not shown). However, the oscillatory strain amplitude sweeps were preferred for calculation of σ_y due to the gel-like nature of the bioinks.[86]

Finally, a frequency amplitude sweep was performed to evaluate the frequency dependence of the moduli for each bioink formulation (Figure 4.9 (c,d)). A noticeable frequency dependence of the moduli was observed for bioinks formulated without Laponite, wherein the moduli values increased with increasing angular frequency. This trend is characteristic of weakly interacting or weakly cross-linked polymer chains, wherein the material is more fluid-like at lower frequencies, while more solid-like at higher frequencies.[86] However, inks formulated with Laponite showed no apparent frequency dependence. This trend is observed for solid-like materials with fairly strong cross-linking interactions and a stress relaxation time that must be greater than the inverse of the lowest applied frequency (0.1 rad s^{-1}). Thus, Laponite imparts structural stability to the bioinks through non-covalent interactions.

Overall, the rheological data demonstrate that, in principle, any of the cdECM bioinks could be suitable for extrusion-based 3DP. They are all hydrogels at rest, with measurable yield stresses. However, bioink formulations without Laponite were not printable in practice. Rheological experiments showed that cdECM bioinks formulated with Laponite are higher-modulus, have lower tan δ, and are more viscous, both at rest and when flowing, than inks without. Physically, this means that inks containing Laponite should have better extrudability, shape fidelity, and stackability in the *z*-dimension.

4.3.3 *Characterization of PEG-DA-Mediated Mechanical Tunability in Composite cdECM Bioinks*

The precise tunability of the mechanical properties of 3D-printed bioinks is critical to the development of tissue models that can replicate native structure and function with a high degree of fidelity. Therefore, an important consideration in the gelation/cross-linking process of engineered bioinks is the curing of the printed construct to reach a target modulus. As such, most dECM-based bioinks have utilized thermal gelation kinetics, wherein the printing process takes advantage of the change in temperature to induce physical cross-linking of abundant collagen within the dECM. However, the rate of thermal gelation is insufficient for extrusion-based bioprinting processes that do not involve the use of a temporary support gel,[93] especially as additional layers are stacked in the *z*-direction. To overcome such challenges, multifaceted cross-linking schemes have been introduced, from two-step thermal gelation approaches[49] to incorporation of photo-polymerizable cross-linkers,[52] which have successfully enhanced the mechanical properties of the cdECM-based bioinks to recapitulate representative cardiac tissue compressive moduli in the range of 5-15 kPa. However, there is still a lack of tissue-derived 3D

bioinks that can recapitulate the mechanical properties of pathological cardiac conditions observed in the fibrotic heart. To take full advantage of the opportunities provided by 3D bioprinting (*i.e.*, *in vitro* disease modeling, drug-screening applications) it is beneficial to create mechanically versatile bioinks that can be tuned to match specific tissue compressive moduli found in both healthy (5-15 kPa) and diseased states (30-100 kPa).

PEG-DA is a common synthetic polymer for hydrogel biomaterials with tunable elastic properties, solute permeability, and biocompatibility.[94,95] Therefore, we sought to incorporate different concentrations of PEG-DA to fabricate a mechanically tunable bioink that can recapitulate a wide range of cardiac tissue compressive moduli. LAP was employed as a water-soluble photo-initiator to rapidly initiate polymerization of the PEG-DA; a prompt polymerization of PEG-DA was desired as rapid cross-linking kinetics are necessary to maintain pattern fidelity of the bio-construct. LAP has also been shown to permit high survival of the encapsulated cells, an important property required to engineer a bioink.[96] Thus, the cdECM composite bioinks in this investigation comprised cdECM-Laponite hydrogels with PEG-DA (6.0%, 8.25%, or 10.5% w/w) and 0.4% w/w LAP.

To quantify both the gelation kinetics and the ability to formulate hydrogels with distinct mechanical properties, we performed oscillatory time sweep measurements with photo-curing (405 nm, 28 mW cm^{-2}) for three printable formulations of our composite cdECM bioink. Each formulation consisted of 4.6% w/w digested cdECM, 2.3% Laponite, and 0.4% LAP, with PEG-DA concentrations of 6.0%, 8.25%, or 10.5%. For the first 120 s of the test, *G'* and *G"* were measured at 1 Hz and 1% strain to obtain baseline moduli prior to photo-polymerization. Irradiation started at 120 s and lasted for 60 s, resulting in fast and stable cross-linking of the bioink (Figure 4.4 (a,b)). The photo-polymerization was rapid for all formulations, with the ink reaching

95% of the final plateau modulus in approximately 14 s (10.5% PEG-DA), 17 s (8.25%) and 20 s (6.0%). These blue-light curing tests also validated the ability to optimize and control material stiffness by varying PEG-DA concentration. As expected, the final stiffness of each bioink increased with increasing PEG-DA concentration from G' = 0.761 kPa (6.0% PEG-DA) to 5.23 kPa (8.25%) to 36.9 kPa (10.5%) (Figure 4.4 (c)). The substantial increase in G' corresponding to a relatively small increase in PEG-DA concentration is likely due to a considerable increase in cross-link density (ρ_x) and decrease in molecular weight between cross-links (M_c). The relationship between moduli (shear, compressive, and tensile) and PEG-DA molecular weight/concentration has been well-characterized in the literature.[97–101]

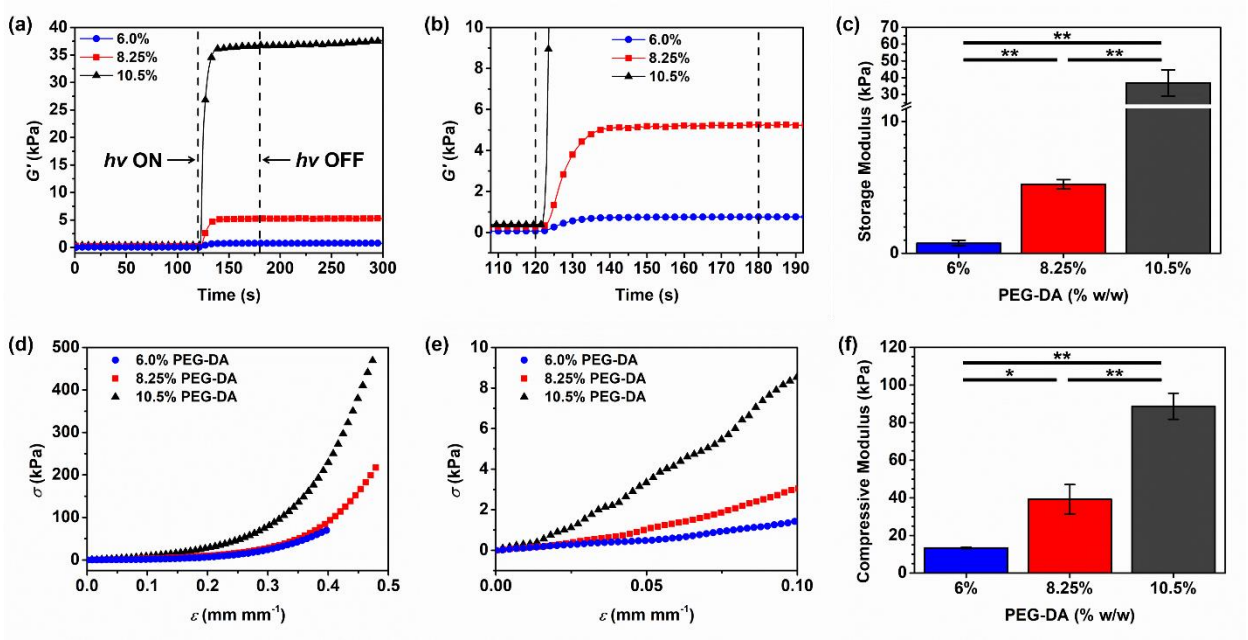

Figure 4.4. Tunable mechanical properties by incorporation of PEG-DA into the cdECM bioinks (a) Oscillatory time sweep analysis (γ = 1%, ω = 1 Hz) of each gel formulation before and after photo-cross-linking. The light was turned on at 120 s and turned off at 180 s. (b) Zoomed time sweep plot between 110-190 s, demonstrating rapid increase in *G'* upon photo-curing. (c) Analysis of *G'* after photo-induced cross-linking (60 s) for different PEG-DA concentrations in cdECM bioinks. Error bars are ± one standard deviation. (d) Stress-strain curves from uniaxial compression testing showing characteristic behavior of hydrogels. All plots are the mean of 3-4 tests. (e) Zoomed stress-strain plot between 0-10% strain, showing linear regions from which compressive moduli were calculated. (f) Analysis of compressive moduli for each PEG-DA concentration between 0-10% strain, showing that the different formulations can be used to recapitulate cardiac tissue stiffness associated with normal (blue) and diseased conditions (red and grey). Error bars are ± one standard deviation. Statistically significant differences were determined via one-way analysis of variance (ANOVA), followed by two-tailed Student's *t*-tests. Asterisks indicate significance levels: *$p < 0.01$; **$p < 0.005$.

Next, uniaxial compression testing was performed on cured hydrogels generated from each composite cdECM bioink formulation. Each formulation was photo-cross-linked in a cylindrical PDMS mold. A representative stress-strain curve was obtained for each composite cdECM bioink

(Figure 4.4 (d)). The linear region of the stress-strain curve between 0-10% strain was used to calculate the compressive modulus (Figure 4.4 (e)). The compressive moduli of the three printable formulations were 13.4 ± 0.4 kPa (6.0% PEG-DA), 39 ± 8 kPa (8.25%), and 89 ± 7 kPa (10.5%) (Figure 4.4 (f)). Importantly, all the printable formulations mimicked either the compressive modulus of healthy (5-15 kPa) or fibrotic (30-100 kPa) cardiac tissues.[54,55] Thus, our low-modulus bioink (6.0% PEG-DA) can be cured to a stiffness that approximates healthy tissue while the intermediate (8.25% PEG-DA) and high-modulus (10.5% PEG-DA) bioinks may be suitable for recapitulating fibrotic tissue.

4.3.4 *3D Printing of Composite cdECM Bioinks*

3DP of intricate tissue constructs requires precise control of optimal printing parameters. Extrusion-based printing offers a high degree of freedom wherein print parameters can be manipulated to determine the dimensions of the extruded bioink, allowing enhanced linewidth resolution and shape fidelity. However, the resolution and fidelity of the print in extrusion-based 3D bioprinting is limited by the inherent properties of the bioink itself. Rheological experiments (Figure 4.2) showed that our printable formulations harbor the necessary characteristics of an extrudable bioink, which inspired confidence in the ability for our bioink to extrude and maintain the intended shape. To further assess the feasibility and versatility of our composite cdECM bioink for extrusion-based printing, we created a simple square CAD design and subjected our bioinks to various printing conditions.

All our printable composite cdECM bioinks were tested using different nozzle sizes and pressures. Two nozzle sizes with distinct inner diameters (25G: 260 μm and 27G: 210 μm), four print pressures (6, 7, 8 and 9 psi), and three PEG-DA concentrations (6.0%, 8.25%, and 10.5%

w/w) were correlated to the linewidth of the extruded filament (Figure 4.5). The printing parameters (*i.e.*, nozzle sizes and print pressures) used to assess printability were chosen based on the ability to reproducibly generate prints with good shape fidelity. The linewidth measurements from 24 different conditions showed that the width of the line can be adjusted from 370 μm to 3 mm. The range of linewidth dimension allows use of lower pressures and smaller nozzle diameters to print constructs with structural detail, while higher pressures and larger nozzle diameters will enable efficient printing of larger structures. The width of the measurement was mostly dependent upon the nozzle diameter, except for the low-modulus bioink (6.0% PEG-DA) which was not as affected by the size of the nozzle (Figure 4.5 (a)). We observed that an increase in the extrusion pressure corresponded with larger linewidth measurements for both nozzle sizes. Interestingly, the concentration of PEG-DA within the bioink was one of the governing factors for linewidth. With the low-modulus bioink (6.0% PEG-DA) (Figure 4.5 (a)), the printed lines were comparably thinner than the intermediate (8.25%) (Figure 4.5 (b)) and high (10.5%) modulus bioinks (Figure 4.5 (c)). This is likely due to the lower viscosity values observed for the intermediate and high-modulus bioinks. While G', tan δ, and σ_y values were similar for the 6.0%, 8.25%, and 10.5% PEG-DA bioinks, the viscosity appeared to decrease from 6.0% to 8.25% to 10.5%. It should be noted that, for the experiments performed, it is difficult to accurately determine statistically significant differences in viscosity values between formulations.

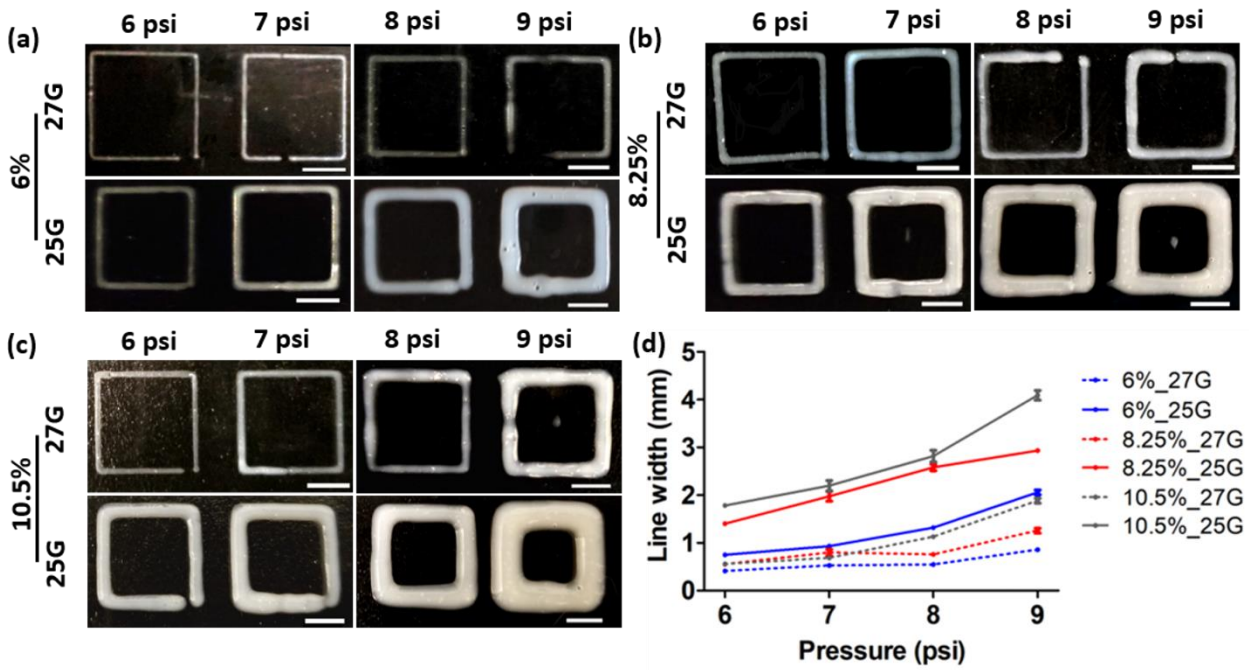

Figure 4.5. Printed line fidelity of cdECM composite bioinks

3D printing of a square CAD model demonstrates adaptability of the bioink for different formulations. The size of the nozzle (25G: 260 μm and 27G: 210 μm) and the feed pressure were varied to generate 8 different print conditions for all three (a) low modulus bioink, (b) intermediate modulus bioink, and (c) high modulus bioink (total of 24 print parameters). The analysis of printability was conducted by quantifying the width of each line print (n = 4). (d) Linewidth measurement graph showing the trend of linewidth with respect to nozzle size, print pressure and composite cdECM bioink formulations. Scale bars: 5 mm.

Furthermore, we prepared a line print using our low-modulus bioink (6.0% PEG-DA) and tested our bioink stability by measuring the width of our print immediately and 7 days after immersion in a salt-balanced aqueous solution. The results showed that the width of our line print is maintained at 2 mm at both time points, indicating that our composite bioinks do not undergo swelling (Figure 4.11).

Next, we created more complex CAD models to demonstrate that our bioink could be applied to print more versatile structures with intricate geometries. We created three distinct

designs: an acronym representing the University of Washington (UW) (Figure 4.6 (a)), a concentric circular design (Figure 4.6 (b)), and a UW husky logo (Figure 4.6 (c)). The low-modulus bioink (4.6% w/w cdECM, 2.3% Laponite, 6.0% PEG-DA) was chosen based on its ability to create higher-resolution prints. Each design was printed at 9 psi and cross-linked immediately after with a 405 nm light module located on the print head (Figure 4.6 (d)). All the designs balanced aqueous solution. The results showed that the width of our line print is maintained at 2 mm at both were printed with high fidelity with respect to the sliced CAD model. Specifically, there was no bleeding of printed bioink, resulting in crisp borders, no disparity in the resolution of different diameters of concentric circles, and high shape fidelity with respect to infill patterns and infill density within the husky logo.

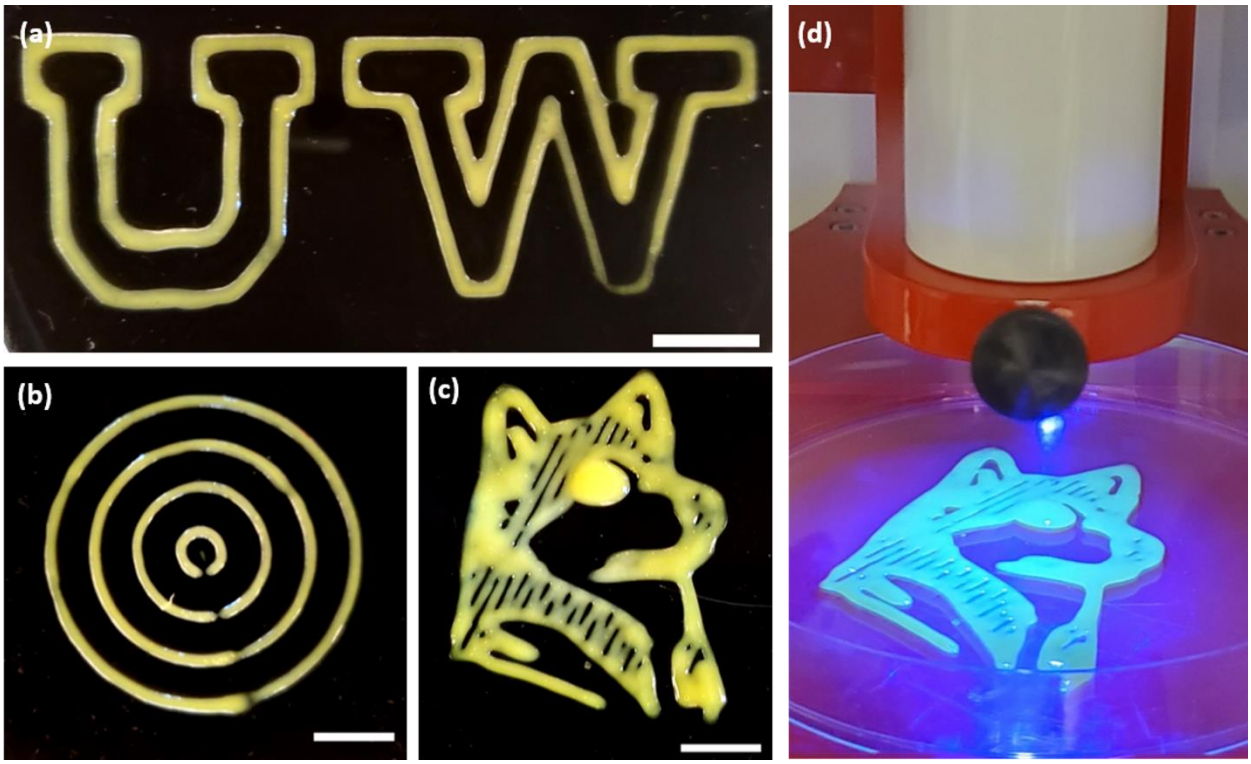

Figure 4.6. Printing of complex geometries using cdECM composite bioink
3D printing of complex geometries demonstrates adaptability of the bioink to create complex structures. cdECM composite bioink with 6.0% PEG-DA was used to print (a) the alphabetic acronym of the University of Washington, (b) a concentric circle and (c) the UW husky logo. (d) Demonstration of blue-light (405 nm) mediated cross-linking for the cdECM composite bioink post-print. Scale bars: 1 cm.

Finally, we tested the feasibility of our composite cdECM bioink to generate a multi-layered 3D construct. Demonstration of stacking of filaments in the *z*-direction was performed *via* layer-by-layer printing of the low-modulus (6.0% PEG-DA) bioink. To improve the durability of the overall construct, 30 s photo-cross-linking (405 nm) of each construct was performed before a subsequent layer was printed on top (Figure 4.7 (a)). The layer-by-layer 3D extrusion printing of the composite bioink afforded a multi-layered construct up to 18 layers (Figure 4.7 (b)). The resulting structure was a flexible elastomer that could be picked up with forceps and maintained

its structure over one month. A multi-layered construct printed using a smaller nozzle size (25G at 9 psi) shows that extruded filaments maintain their shape prior to cross-linking and enhance the fidelity of each print in the *z*-direction (Figure 4.7 (c,d)). The top view image, especially, validates that the material did not collapse as more ink was deposited, suggesting high durability and structural integrity of the bioink (Figure 4.7 (d)). The printability of our bioink in the *z*-direction was quantitatively validated through measurement of each layer width at different *z*-positions (heights) of the construct. Indeed, the linewidths were relatively similar throughout the entire multi-layered construct, which further validated the high fidelity and mechanical durability enabled by our composite cdECM bioink (Figure 4.7 (c)).

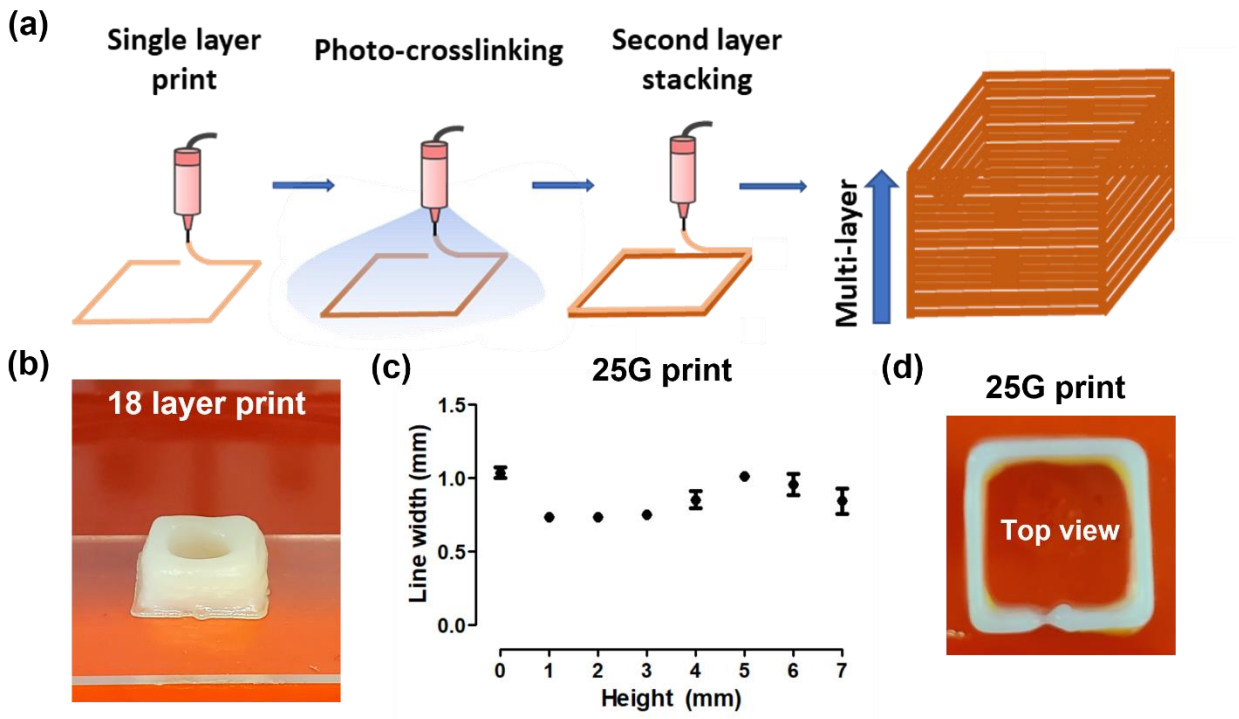

Figure 4.7. 3D printing of cdECM composite bioink in the *z*-direction

3D printing of multiple stacks of square prints was conducted to demonstrate the ability to fabricate a mechanically stable, layered 3D construct in the (vertical) *z*-direction. (a) Schematic of the 3DP process involved in an 18-layered tower. Each print was conducted using a 25G nozzle at 9 psi or a 22G nozzle at 8 psi with the low-modulus bioink (6.0% PEG-DA) and immediately cross-linked using blue-light (405 nm) irradiation for 30 s. This process was repeated 18 times to create a stable, 18-layered construct. (b) Picture of an 18-layered construct printed with a 22G nozzle at 8 psi. (c) Analysis of the linewidth quantified for different heights of the 18-layered construct printed with a 25G nozzle at 9 psi post-print (n = 4) and (d) top view of the construct printed with a 25G nozzle at 9 psi. The measurements were taken using calipers every 1 mm until the final layer.

4.3.5 *Biocompatibility Assessment of Composite cdECM Bioinks*

To demonstrate the feasibility of utilizing our engineered cdECM composite bioink as a tissue engineering scaffold, we tested the biocompatibility of various control and printable bioink formulations. Previous studies have shown that bioinks comprised of cdECM were able to support cellular survival up to 7 days post-print, indicating that the cdECM-based bioinks were not only biocompatible but also able to withstand shear conditions during the pneumatic printing process.[46,48] To test whether the incorporation of Laponite, high concentrations of PEG-DA, and LAP photo-initiator diminishes the biocompatibility of our bioink, we demonstrated cell viability using primary human cardiac fibroblasts (HCFs) and human induced pluripotent stem cell derived cardiomyocytes (hiPSC-CMs). HCF cells were chosen based on previous studies that have investigated the effect of substrate stiffness on trans-differentiation of myofibroblasts. As myofibroblast trans-differentiation manifests in cardiac fibrosis through mechano-transduction of stiffening cardiac ECM, HCFs serve as an ideal cell type to investigate a potential mechano-transduction pathway involved in cardiac fibrosis, a potential application of the mechanically tunable composite bioink.[57,102,103] Characterization of cell survival was conducted through a Live/Dead Assay kit on varying formulations of cdECM, Laponite and PEG-DA containing gels. Initially, we tested the viability of cells in a 0-0-6% (PEG-DA only) gel, a 0-2.3-6% (Laponite and PEG-DA) gel, and a 4.6-0-6% (cdECM and PEG-DA) gel (Figure 4.12). Viability results showed that addition of Laponite and cdECM significantly increased the cellular survival after 7 days. In particular, Laponite enabled the highest survival of HCFs cultured within the gels, maintaining viability above 98% throughout a 7-day long culture period. This finding aligns well with previous reports of cdECM-based hydrogels and Laponite-containing hydrogels that exhibit excellent biocompatibility both *in vitro* and *in vivo.*[72,104]

Next, we tested the viability of HCFs within our composite printable bioink formulations with varying concentrations of PEG-DA (6.0%, 8.25% and 10.5% w/w) and compared the results to the 4.6-0-0% (cdECM only) gel. To better understand the possible effects of synthetic additives (*i.e.* Laponite, PEG-DA and LAP photoinitiator) on cell viability, we performed hand extrusion of cell-laden bioinks using the exact syringes and needles required for 3D printing. This method was chosen because: 1) the printing pressure required to print our material is similar to the pressure applied during hand extrusion and 2) it avoids variability that may arise from printing parameters. To ensure the consistency of shear stress applied to the cells within the bioink, we utilized the same needle gauge used to 3D print our cell-laden bioinks. Therefore, we do not expect to observe significant changes between the overall percent viability of the cells within hand extruded bioinks and 3D printed bioinks, aside from larger variations in the standard error caused by the variability of print parameters used in the 3D printing system. Our composite bioink exhibited high cellular survival 1 day and 7 days after printing and cross-linking (> 97% viability), indicating that the PEG-DA concentrations used in our hydrogels do not cause any deleterious effects (Figure 4.8). Moreover, compared to the cdECM-only formulation, our printable formulations (*i.e.*, those containing Laponite) showed reduced cellular cytotoxicity, suggesting that the addition of Laponite drastically enhanced the viability of the cells. In addition, comparing the viability results of cells in cdECM-only gels (Figure 4.8) with cells in cdECM and PEG-DA gels show that introduction of PEG-DA-mediated cross-linking increased cellular survival. Because PEG-DA photo-polymerization occurred within 30 s, cured constructs were immersed in culture media quickly after printing. By contrast, the thermally cured cdECM-only gels required 30 minutes of gelation time, depriving encapsulated HCFs of media for a long period of time and decreasing cellular survival.

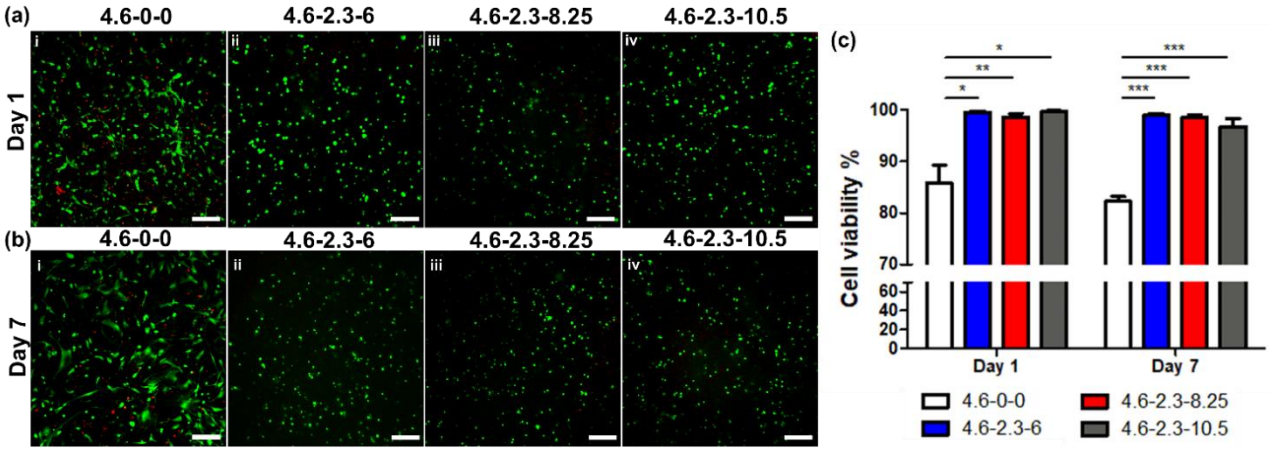

Figure 4.8. Viability of human cardiac fibroblasts embedded in cdECM bioinks

Live/Dead cell viability was performed on HCFs encapsulated within composite bioinks. x-y-z numbers in the legends refer to x: cdECM % w/w, y: Laponite %, and z: PEG-DA % within the bioink. (a,b) Representative fluorescence images with live/dead viability staining at (a) day 1 and (b) day 7 of culture. Cellular survival was higher in all composite bioink formulations with (ii) 6.0% PEG-DA; (iii) 8.25% PEG-DA; and (iv) 10.5% PEG-DA compared to (i) cdECM only (4.6-0-0%) gels. (c) Quantification of cell viability showed that HCFs maintained high viability (> 97%) within all bioink formulations compared to the cdECM-only gel. Although viability was lower in the cdECM-only gel, HCFs exhibited more spreading, suggesting that cdECM only was more favorable for enzymatic degradation by HCFs. Scale bar: 200 μm. Statistically significant differences were determined via one-way analysis of variance (ANOVA), followed by two-tailed Student's *t*-tests. Asterisks indicate significance levels: *$p < 0.001$; **$p < 0.05$; ***$p < 0.0005$.

One drawback to our printable formulation, however, is the inability of HCFs to spread out and assume their native fibroblast morphology as observed in the cdECM-only gel. This is likely a direct result of diminished biochemical cues and the presence of dense, non-biodegradable PEG-DA networks that prevented the cells from enzymatically degrading and remodeling the matrix. Similarly, unlike the normal EHT tissues, which are able to compact and generate functional cardiomyocyte beating within one week, EHTs generated from our bioinks showed limited

compaction (data not shown), re-confirming our hypothesis that cell-cell interaction between the stromal cells responsible for contraction of EHT was limited by the dense, cross-linked PEG-DA network within our gels that reduced cellular ability to remodel the matrix. Nevertheless, the incorporation of Laponite and PEG-DA were necessary for high-fidelity extrusion 3D printing and for recapitulating the mechanical properties that we are aiming to model. Furthermore, previous studies showed that Laponite and gold nanoparticles incorporated into an injectable dECM hydrogel allowed enhanced functionality of cardiac tissues, suggesting that Laponite may not significantly impair the functionality of cardiac cells.[105] Our results also show that all four EHTs harboring hiPSC-CMs exhibited high viability (> 94%) after 7 days of culture, thus validating that additives within our printable bioink formulations can support the survival of less robust cells such as hiPSC-CMs (Figure 4.13). However, we recognize that further analysis of cellular activity needs to be addressed for application of the bioinks in disease modeling. One possibility is the inclusion of enzymatically cleavable bonds within the cross-linkers for facile degradation of the surrounding matrix, which would further support functional activity of cardiac cells within the system.

4.4 CONCLUSIONS

Composite bioinks derived from porcine cdECM were engineered for extrusion-based 3DP of constructs with tunable elasticity. Laponite-XLG nanoclay enabled shape fidelity and high resolution by increasing the shear storage modulus and viscosity of the cdECM-based hydrogels. The final compressive modulus of the photo-polymerized hydrogels was adjustable from 13.4-89 kPa according to the concentration of PEG-DA in the bioink formulation. This range of moduli encompasses the stiffness of both healthy and fibrotic cardiac tissue and shows that our printed constructs could be viable models of cardiac disease states. The linewidths of the extruded cdECM

bioink filaments were correlated to both extrusion pressure and nozzle diameter, demonstrating quantification of print resolution and shape fidelity. Complex and multi-layer structures could also be printed, which are important considerations for future printing of biologically relevant 3D bio-constructs. Finally, encapsulated human cardiac fibroblasts survived both extrusion and photo-polymerization to show > 97% viability after 7 days, demonstrating the cytocompatibility of the cdECM composite bioinks. Additional viability testing with human induced pluripotent stem cell derived cardiomyocytes also showed that our bioinks could support the survival of less robust cardiac cells. This study lays the groundwork for 3D bioprinting of constructs intended to model both healthy and fibrotic cardiac tissue states by recapitulating biological cues and biomechanical properties.

4.5 EXPERIMENTAL

4.5.1 *Decellularization of Porcine Cardiac Tissue*

Cardiac tissues were obtained from porcine hearts, purchased from a local butcher. Left ventricles were specifically harvested from porcine hearts and stored at -20 °C, up to 6 months. Cardiac tissues were thawed, diced, washed in deionized (DI) water for 2 h and decellularized using multiple chemical detergents, following a published protocol.[48] Briefly, the rinsed cardiac tissues were immersed in 1% sodium lauryl sulfate (Fisher Scientific; SDS) in phosphate buffered saline (PBS, Invitrogen) for 72 h. Following SDS treatment, porcine heart cubes were treated with 1% Triton X-100 (Sigma-Aldrich) in PBS for 1 h, then washed in PBS for 72 h. All rinsing and detergent washing steps involved stirring of the solution on stir plates at 200 rpm. Solution changes for 1% SDS (in PBS) and PBS occurred daily to ensure efficient removal of cellular debris and

thorough washing of remaining detergents. After PBS washes, the decellularized scaffold tissues were collected in tubes and stored at -80 °C until lyophilization.

4.5.2 *Composite cdECM Bioink Preparation*

Fabrication of the cdECM pre-gel was conducted by lyophilizing frozen samples of cdECM for 72 h. Lyophilized cdECMs were stored at 4 °C up to 3 months prior to pepsin digestion. Upon digestion, lyophilized cdECM was shredded and finely chopped into flakes using razor blades. To prepare the cdECM pre-gel, cdECM flakes were massed in a glass vial for digestion at ~9-10% w/v; typically, 500 mg of cdECM was combined with 50 mg of pepsin (P7000, from porcine gastric mucosa, Sigma-Aldrich) and 4.3 mL of 0.1 M aqueous HCl at room temperature for one week. Following digestion, solubilized 10% cdECM pre-gel was diluted with 0.5 mL of 10X RPMI to account for ionic balance. The remaining volume (200 μL) was used to adjust final pH to 7.4 using 10 M aqueous NaOH. A pH meter was used to monitor the change during pH adjustment. cdECM pre-gels were stored at 4 °C up to 2 weeks.

The solubilized cdECM was combined with a nanoclay viscosity modifier, Laponite-XLG (BYK Additives & Instruments), a photo-curable cross-linker, PEG-DA (M_n = 700 g mol^{-1}, Sigma-Aldrich), and a photo-initiator, lithium phenyl-2,4,6-trimethylbenzoylphosphinate (LAP; Sigma-Aldrich). Laponite powder was pre-dissolved in DI water at 9.1% w/w to prevent separation of Laponite and cdECM and to help form a homogeneous gel. All gels were formulated by mass/weight. Typical bioink preparation was as follows: First, the LAP photo-initiator was added to a clean glass vial. Next, the appropriate mass of cdECM pre-gel was added to the glass vial, followed by 9.1% w/w Laponite gel. A small volume of 10X RPMI 1640 media was then added to ensure final 1X concentration. This was followed by DI water, and finally by PEG-DA (liquid

at room temperature). The final concentrations of each component were 0.4% w/w LAP, 1X RPMI, 4.6% w/w cdECM, 2.3% w/w Laponite, and 6.0, 8.25, or 10.5% w/w PEG-DA, with DI water constituting the remaining mass. The final composite bioinks were briefly vortexed, then centrifuged for ~30 s at 2 000 rpm to ensure collection of all components at the bottom of the vial. Finally, the bioinks were covered with reflective foil and stirred at room temperature until visually homogeneous, at least 18 h.

4.5.3 *Rheometric Analysis*

All rheometric experiments were performed on a TA Instruments Discovery HR-2 hybrid rheometer equipped with a Peltier temperature-control accessory. All experiments utilized a flat-plate 8 mm stainless steel geometry and were conducted at 21 °C. First, strain amplitude sweep experiments were conducted for each cdECM ink formulation to establish the linear viscoelastic region (LVR). All strain amplitude sweeps were conducted at a constant angular frequency (ω) of 1 Hz (6.28 rad s^{-1}). Then, frequency amplitude sweeps were performed at constant 1% oscillatory strain (γ) to determine the viscoelastic behavior of the gels at both short and long time scales. To help quantify printability, shear-thinning experiments were carried out during which samples were subjected to increasing rates of shear (0.005-50 s^{-1}). To further establish the reversible mechanical yielding and recovery of the bioinks, short oscillatory step-strain experiments were conducted at constant frequency (1 Hz) with alternating cycles of 1% and 100% strain amplitude. Finally, blue-light (405 nm) photo-curing at 28 mW cm^{-2} intensity was performed using a Mightex BLS-series BioLED analog control module coupled to a Mightex WLS-series WheeLED^{TM} light source. These curing experiments demonstrated rapid photo-curing of the bioinks. It should be noted that these rheological curing experiments provided measures of the *shear* modulus (G'), which is a different

parameter from the *compressive* modulus measured on a load frame. Moreover, the intensity of light used to cure rheological samples (28 mW cm^{-2}) may not have been the same intensity as the light used for curing compressive samples, which could not be accurately quantified. The purpose of the rheological curing experiments was simply to demonstrate rapid photo-curing and to provide an estimate of the range of material stiffness that could be achieved.

4.5.4 *Compressive Modulus Testing*

Cylindrical samples for compression testing, approximately 9 mm in diameter by 5 mm in height, were cast in PDMS molds. Samples were cured under 395-400 nm irradiation (QUANS UV LED flood light, 20 W) at a distance of 15 cm from the light for 60 s. Uniaxial compression testing was performed on an Instron 5585H load frame using a 50 N load cell at a rate of 1.3 mm min^{-1}. Uniaxial compressive force was applied to the hydrogel constructs until the point of failure. The compressive modulus was calculated using linear regression analysis of the stress-strain curve between 0-10% strain. Each bioink formulation was measured at least in triplicate.

4.5.5 *Characterization of Bioink Printability*

Allevi 2, a two-syringe 3D bioprinter with a pneumatic pressure system, was used to print the cdECM-Laponite-PEG-DA “composite” bioink. Testing of the bioink printability was conducted for all formulations (6.0%, 8.25% and 10% w/w PEG-DA) by printing a square CAD model (10 mm x 10 mm). Prior to printing, the cdECM composite bioink was loaded into a 10-mL syringe by filtering through a 25G needle to ensure successful printing. The syringe was then connected to an external pressure source to enable pneumatic extrusion. Various ranges of

pneumatic pressure (6, 7, 8 and 9 psi) and the diameter of the nozzle (25G: 260 μm and 27G: 210 μm) were used to optimize best printing parameters as well as to demonstrate the versatility and adaptability of the cdECM composite bioink. After each print, an external blue-light module (405 nm) located under the extruder head was turned on for 60 s to immediately cross-link the printed bioink. Photographs of printed constructs were analyzed using ImageJ software to quantify the print linewidth measurements and to analyze overall printability of the cdECM bioinks.

Demonstration of the cdECM composite bioink printability was further validated by creating and printing CAD models harboring complex geometries. Three different designs, the UW husky logo, University of Washington acronym, and concentric circles with varying diameters, were prepared. For visualization, 1 μL of yellow food dye (Whole Foods 365 Brand; based on vegetable glycerin and turmeric) was incorporated into the final gel formulation. The husky logo was 2 cm x 3 cm with infill density of 30%, and the concentric circles consisted of 4 different circles (1, 2, 3, and 4 cm in diameter). All prints were demonstrated using the cdECM composite bioink comprised of 6.0% PEG-DA and 2.3% Laponite. A 25G nozzle at 9 psi was used to print each design at room temperature. After printing, each design was photocured using a blue-light module for 30 s. Confirmation of the stability of our printed material was conducted using the 6.0% PEG-DA bioink, which was printed, photo-cured and immersed in Hank's buffered solution for 1 week.

The ability to print a multi-layer construct was analyzed by layering square prints to create a *z*-construct of 18 layers. To test printability in the *z*-direction, the cdECM-Laponite-PEG-DA "composite" bioink (6.0% PEG-DA) was printed using both a 25G nozzle at 9 psi and a 22G nozzle at 8 psi. *Z*-stacks were created through a layer-by-layer method whereby each layer was extruded then cross-linked using 405 nm irradiation for 30 s before a subsequent layer was printed on top

of the previous cured layer. Following curing steps, the print stage was lowered by 0.4 mm. The thickness of each layer was measured from each side of the printed 3D construct and was used to quantify the structural durability of the *z*-stack.

4.5.6 *Cell Culture*

Human cardiac fibroblasts (HCFs), human induced pluripotent stem cell (hiPSC) derived cardiomyocytes, and HS27A human bone marrow derived stromal cells (ATCC) were cultured for use in assessing the biocompatibility of the cdECM-Laponite-PEG-DA composite bioink. Briefly, HCFs were cultured in Fibroblast Medium-2 (ScienCell) supplemented with 5% Fetal Bovine Serum (ScienCell), fibroblast growth supplement-2 (ScienCell; FGS-2) and 1% Penicillin/Streptomycin (ScienCell). Media was changed every 2 days, and cells between passage 3-5 were utilized. ATCCs were cultured and maintained in high-glucose DMEM (Invitrogen) supplemented with 10% fetal bovine serum.

UC 3-4 urine-derived hiPSCs[75] were cultured and differentiated into cardiomyocytes following an adaptation of a previously published method.[76] In brief, hiPSCs were induced with RPMI 1640 medium (Invitrogen) supplemented with B-27 without insulin (Invitrogen) and 10 μM CHIR-99021 (Selleck Chemicals). After 18 h, the medium was replaced with fresh RPMI/B-27 without insulin for 48 h. The medium was then replaced with RPMI/B-27 without insulin supplemented with 5 μM IWP-4 (REPROCELL) for 48 h, after which the medium was once again replaced with fresh RPMI/B-27 without insulin for 48 h. Finally, medium was replaced with RPMI/B-27 with insulin (Invitrogen). Spontaneously beating cells are typically observed 10-12 days after induction.

4.5.7 *Fabrication of Engineered Heart Tissue Constructs*

The design and fabrication of the hardware utilized for both generating the engineered heart tissues (EHTs) and measuring forces *in situ* has been previously described.[77] In brief, post pair arrays were fabricated by pouring polydimethylsiloxane (PDMS; Sylgard 184, Dow Chemical) at a 10:1 base to curing agent ratio into an acrylic mold. A glass capillary tube was inserted into one post of each pair to impart rigidity to that post. Molds were then placed into a 65 °C oven overnight to cure the PDMS. Cured post pair arrays were then removed from the mold. Each post was 12.5 mm long and 1.5 mm in diameter and featured a cap structure 0.5 mm thick and 2 mm in diameter to assist with tissue attachment. Post-to-post spacing was 8 mm. Wells for tissue casting were fabricated by pouring approximately 1 mL of PDMS into the wells of a 24-well culture plate before inserting custom 3D printed spacers that would form rectangular wells with dimensions of 12 mm x 4 mm x 4mm (length x width x depth). After curing the PDMS overnight, molds were removed.

hiPSC-CMs and HS-27A stromal cells were mixed in the cdECM-Laponite-PEG-DA composite bioink (6.0% PEG-DA) at cell densities of 20 x 10^6 cells/mL and 10 x 10^6 cells/mL, respectively. 70 μL of this cell-hydrogel mixture was then pipetted into each casted PDMS well, after which PDMS post arrays were positioned upside-down into the wells, ensuring that each post tip was immersed in the cell-hydrogel solution. The 24-well plate was then exposed to blue light for 30 seconds before it was placed into an incubator at 37°C and 5% CO2 for approximately 60 min. 1 mL of RPMI/B-27 with insulin (supplemented with Y-27632 dihydrochloride ROCK inhibitor and 1% penicillin/streptomycin) was then added to each well. After 24 h, the media was replaced with fresh RPMI/B-27 with insulin, and media changes were conducted every other day.

4.5.8 *Cell Viability Testing*

Cell viability was assessed on a thin disc of cdECM-Laponite-PEG-DA hydrogel (0.1 mm thick x 1 mm in diameter) containing HCFs and on EHTs containing hiPSC-CMs and ATCCs. HCFs were resuspended into respective bioink formulations at a density of 2.0 x 10^6 cells/mL. Each formulation was syringe-extruded into thin discs (7mm x 7mm x 1mm). After 1 day and 7 day culture periods, cell viability analysis was performed using a live/dead cell assay kit (Invitrogen Life Technologies, USA) following the protocol provided by the manufacturer. Stained samples were imaged using 10X magnification through a confocal microscope (Spinning disk, Nikon Instruments, NY, USA) and quantified using ImageJ image processing software (National Institutes of Health, MD, USA). Green fluorescence signals indicated live cells (calcein-AM excitation/emission: 488/515 nm) whereas red fluorescence signals indicated dead cells (ethidium homodimer-1 excitation/emission: 570/602 nm). Viability analysis was conducted by quantifying the number of live cells in each culture condition using ImageJ software.

4.5.9 *Statistical Analysis*

All data are reported as mean ± standard deviation. Statistical significance was determined *via* a one-way analysis of variance (ANOVA) test for all the quantification measurements, including comparisons of compressive modulus, storage modulus, tan δ, and yield stress (σ_y). Pairwise *f*-tests and two tailed Student's *t*-tests were subsequently conducted for pairs of data sets.

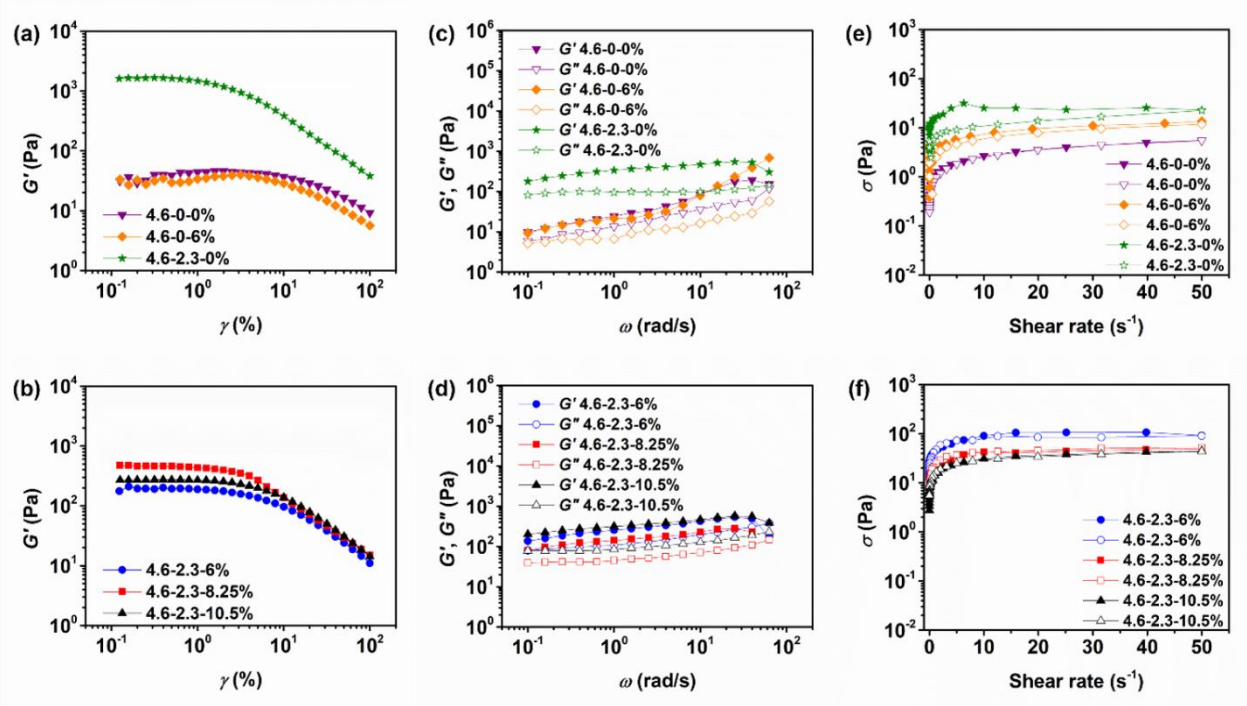

Figure 4.9. Further rheometric characterization of cdECM composite bioinks

(a,b) Oscillatory strain amplitude sweeps performed at 1 Hz (6.28 rad s^{-1}) angular frequency for (a) control and (b) printable formulations. Data between 0.01-0.1% strain has been omitted due to inconsistency and instrument sensitivity issues. All plots are the mean of three experiments. (c,d) Frequency amplitude sweeps from 0.1-100 rad s^{-1} conducted at 1% strain for (c) control and (d) printable formulations. The final data point at 100 rad s^{-1} has been omitted due to wall slippage effects. (e,f) Plots of stress *vs*. shear rate for (e) control and (f) printable formulations. Filled symbols indicate increasing shear rate, while open symbols indicate decreasing shear rate. The shape of the flow curves is characteristic of shear-thinning viscoelastic materials with a measurable yield stress. Herschel-Bulkley curve fitting (not shown) resulted in inconsistent and sometimes invalid estimates of yield stress.

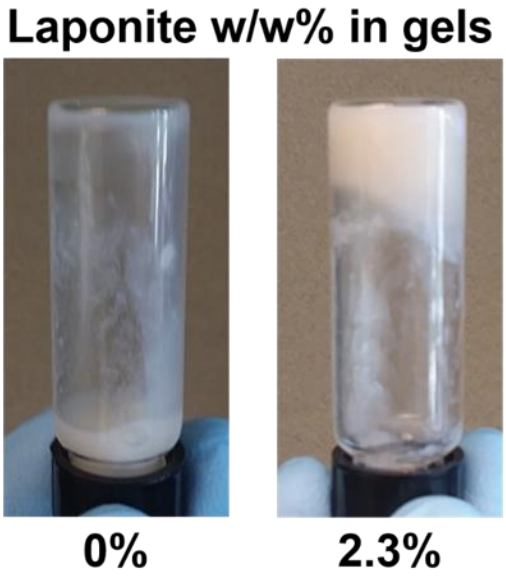

Figure 4.10. Photos of cdECM composite inks with/without Laponite

Composite cdECM gel formulations without (left) and with (right) Laponite-XLG, demonstrating difference in flow behavior when the vial is inverted. The addition of Laponite enhances the apparent viscosity of the gel.

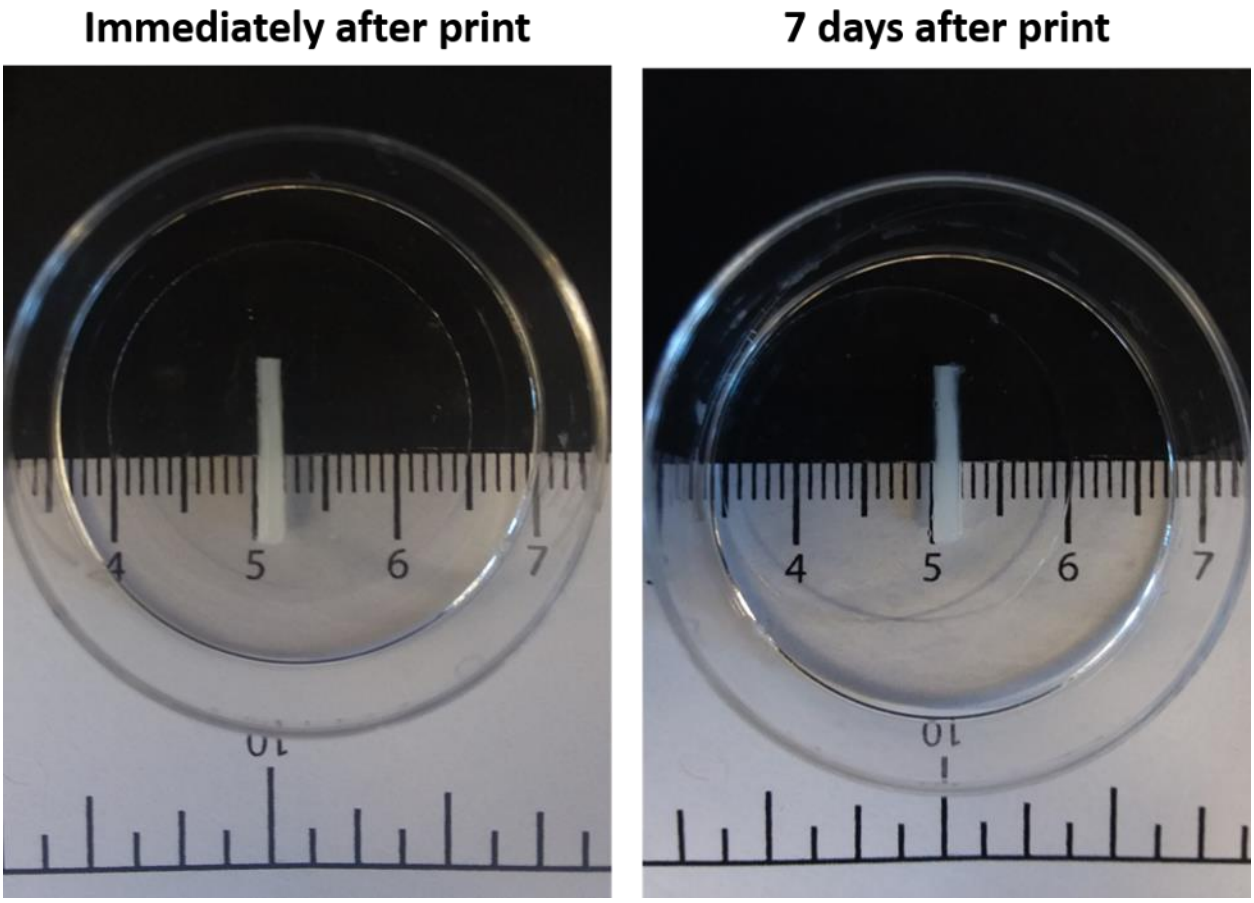

Figure 4.11. Non-swelling of cross-linked cdECM bioink constructs

Cross-linked, printed structures do not swell in aqueous media. Images of line prints immediately after (left) and 7 days after (right) incubation in PBS. The print was conducted using the low-modulus composite bioink (6.0% PEG-DA, 2.3% Laponite). The material did not undergo swelling over a one-week period and maintained its structural integrity.

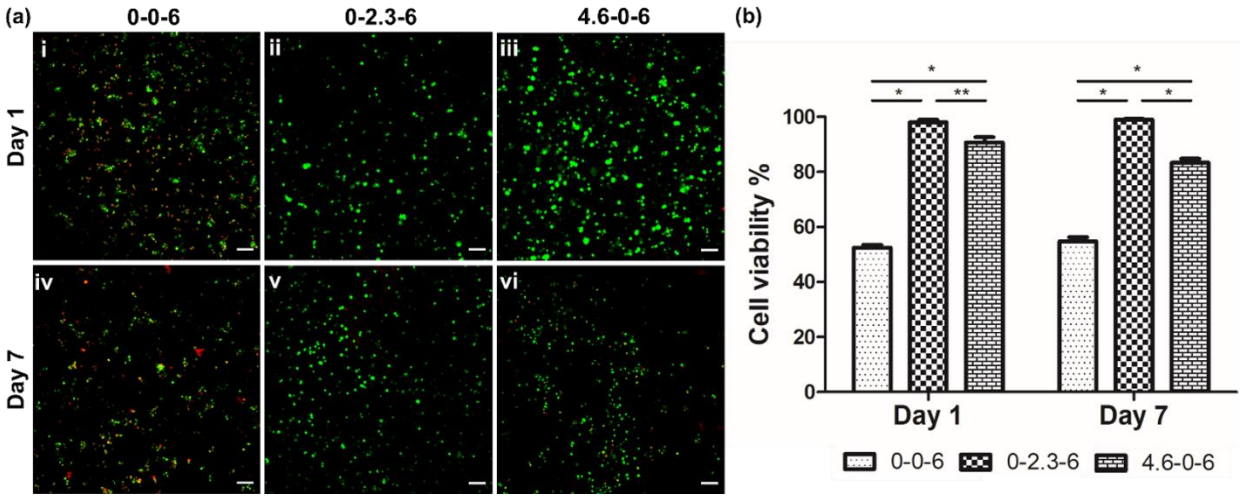

Figure 4.12. Additional viability of HCFs in cdECM bioinks

(a) Images of live/dead staining of human cardiac fibroblasts (HCFs) in the (i,iv) PEG-DA (0-0-6%) gel, (ii,v) Laponite/PEG-DA (0-2.3-6%) gel, and (iii,vi) cdECM/PEG-DA (4.6-0-6%) gel. Scale bars: 100 µm. (b) Quantification of cell viability shows that Laponite/PEG-DA gels support > 95% cell survival, suggesting that Laponite significantly enhances the viability of encapsulated cells.

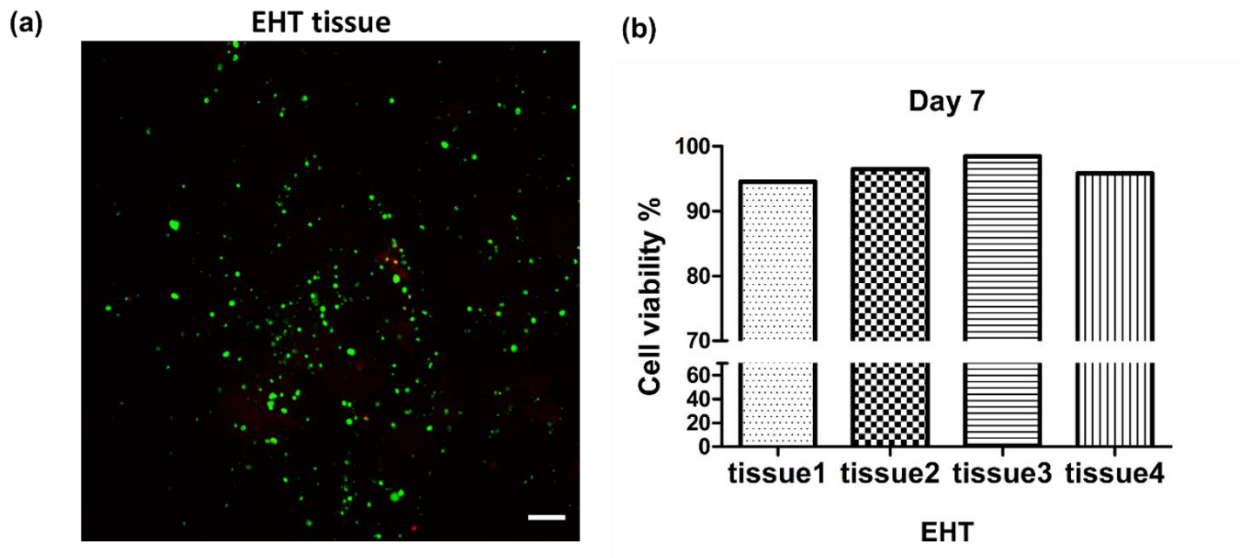

Figure 4.13. Engineered heart tissue fabricated from cdECM bioinks

Engineered heart tissue (EHT) fabricated from cdECM bioinks supports the survival of human induced pluripotent stem cell derived cardiomyocytes (hiPSC-CMs). (a) Live/dead stained images of hiPSC-CMs within engineered heart tissue generated from cdECM composite bioinks. Scale bar: 100 μm. (b) Quantification of percent viability of cells after a 7-day culture shows > 94% of survival in all four tissues.

4.6 ACKNOWLEDGEMENTS

Reprinted (adapted) with permission from Shin, Y.J.; Shafranek, R.T.; Tsui, J.H.; Walcott, J.; Nelson, A.; Kim, D.-H. 3D Bioprinting of Mechanically Tuned Bioinks Derived from Cardiac Decellularized Extracellular Matrix. *Acta Biomaterialia* **2021**, *119*, 75-88.

This work was supported by the National Institutes of Health grants R01HL146436, R01HL94388, R01NS094388, UG3TR003271, and UH3TR003519 (to D.-H.K.), and the University of Washington Royalty Research Fund (to A.N.). This work was also supported by the

Korea Health Technology R&D Project through the Korea Health Industry Development Institute (KHIDI), funded by the Ministry of Health & Welfare, Republic of Korea (HI19C0642).

4.7 REFERENCES

(1) Kang, H. W.; Lee, S. J.; Ko, I. K.; Kengla, C.; Yoo, J. J.; Atala, A. A 3D Bioprinting System to Produce Human-Scale Tissue Constructs with Structural Integrity. *Nat. Biotechnol.* **2016**, *34* (3), 312–319.

(2) Bejleri, D.; Davis, M. E. Decellularized Extracellular Matrix Materials for Cardiac Repair and Regeneration. *Adv. Healthc. Mater.* **2019**, *8* (5), 1801217(1-29).

(3) Choi, Y.-J.; Jun, Y.-J.; Kim, D. Y.; Yi, H.-G.; Chae, S.-H.; Kang, J.; Lee, J.; Gao, G.; Kong, J.-S.; Jang, J.; et al. A 3D Cell Printed Muscle Construct with Tissue-Derived Bioink for the Treatment of Volumetric Muscle Loss. *Biomaterials* **2019**, *206*, 160–169.

(4) Lee, A.; Hudson, A. R.; Shiwarski, D. J.; Tashman, J. W.; Hinton, T. J.; Yerneni, S.; Bliley, J. M.; Campbell, P. G.; Feinberg, A. W. 3D Bioprinting of Collagen to Rebuild Components of the Human Heart. *Science (80-.).* **2019**, *365* (6452), 482–487.

(5) Wang, L. L.; Highley, C. B.; Yeh, Y.-C.; Galarraga, J. H.; Uman, S.; Burdick, J. A. Three-Dimensional Extrusion Bioprinting of Single- and Double-Network Hydrogels Containing Dynamic Covalent Crosslinks. *J. Biomed. Mater. Res. - Part A* **2018**, *106* (4), 865–875.

(6) Song, K. H.; Highley, C. B.; Rouff, A.; Burdick, J. A. Complex 3D-Printed Microchannels within Cell-Degradable Hydrogels. *Adv. Funct. Mater.* **2018**, *28* (31), 1801331(1-10).

(7) Ouyang, L.; Highley, C. B.; Rodell, C. B.; Sun, W.; Burdick, J. A. 3D Printing of Shear-Thinning Hyaluronic Acid Hydrogels with Secondary Cross-Linking. *ACS Biomater. Sci. Eng.* **2016**, *2* (10), 1743–1751.

(8) Farzin, A.; Miri, A. K.; Sharifi, F.; Faramarzi, N.; Jaberi, A.; Mostafavi, A.; Solorzano, R.; Zhang, Y. S.; Annabi, N.; Khademhosseini, A.; et al. 3D-Printed Sugar-Based Stents Facilitating Vascular Anastomosis. *Adv. Healthc. Mater.* **2018**, *7* (24), 1800702(1-9).

(9) Zhu, K.; Shin, S. R.; van Kempen, T.; Li, Y.-C.; Ponraj, V.; Nasajpour, A.; Mandla, S.; Hu, N.; Liu, X.; Leijten, J.; et al. Gold Nanocomposite Bioink for Printing 3D Cardiac Constructs. *Adv. Funct. Mater.* **2017**, *27* (12), 1605352(1-12).

(10) Homan, K. A.; Kolesky, D. B.; Skylar-Scott, M. A.; Herrmann, J.; Obuobi, H.; Moisan, A.; Lewis, J. A. Bioprinting of 3D Convoluted Renal Proximal Tubules on Perfusable Chips. *Sci. Rep.* **2016**, *6*, 34845(1-13).

(11) Highley, C. B.; Song, K. H.; Daly, A. C.; Burdick, J. A. Jammed Microgel Inks for 3D Printing Applications. *Adv. Sci.* **2019**, *6* (1), 1801076(1-6).

(12) Skylar-Scott, M. A.; Uzel, S. G. M.; Nam, L. L.; Ahrens, J. H.; Truby, R. L.; Damaraju, S.; Lewis, J. A. Biomanufacturing of Organ-Specific Tissues with High Cellular Density and Embedded Vascular Channels. *Sci. Adv.* **2019**, *5* (9), eaaw2459(1-13).

(13) Kolesky, D. B.; Homan, K. A.; Skylar-Scott, M. A.; Lewis, J. A. Three-Dimensional Bioprinting of Thick Vascularized Tissues. *Proc. Natl. Acad. Sci. U. S. A.* **2016**, *113* (12), 3179–3184.

(14) Lind, J. U.; Busbee, T. A.; Valentine, A. D.; Pasqualini, F. S.; Yuan, H.; Yadid, M.; Park, S.-J.; Kotikian, A.; Nesmith, A. P.; Campbell, P. H.; et al. Instrumented Cardiac Microphysiological Devices via Multimaterial Three-Dimensional Printing. *Nat. Mater.*

2017, *16* (3), 303–308.
(15) Trachsel, L.; Johnbosco, C.; Lang, T.; Benetti, E. M.; Zenobi-Wong, M. Double-Network Hydrogels Including Enzymatically Crosslinked Poly-(2-Alkyl-2-Oxazoline)s for 3D Bioprinting of Cartilage-Engineering Constructs. *Biomacromolecules* **2019**, *20*, 4502–4511.
(16) Murphy, S. V.; Atala, A. 3D Bioprinting of Tissues and Organs. *Nat. Biotechnol.* **2014**, *32* (8), 773–785.
(17) Lee, M.; Bae, K.; Guillon, P.; Chang, J.; Arlov, Ø.; Zenobi-Wong, M. Exploitation of Cationic Silica Nanoparticles for Bioprinting of Large-Scale Constructs with High Printing Fidelity. *ACS Appl. Mater. Interfaces* **2018**, *10* (44), 37820–37828.
(18) Gauvin, R.; Chen, Y.-C.; Lee, J. W.; Soman, P.; Zorlutuna, P.; Nichol, J. W.; Bae, H.; Chen, S.; Khademhosseini, A. Microfabrication of Complex Porous Tissue Engineering Scaffolds Using 3D Projection Stereolithography. *Biomaterials* **2012**, *33* (15), 3824–3834.
(19) Kolesky, D. B.; Truby, R. L.; Gladman, A. S.; Busbee, T. A.; Homan, K. A.; Lewis, J. A. 3D Bioprinting of Vascularized, Heterogeneous Cell-Laden Tissue Constructs. *Adv. Mater.* **2014**, *26* (19), 3124–3130.
(20) Barry, R. A.; Shepherd, R. F.; Hanson, J. N.; Nuzzo, R. G.; Wiltzius, P.; Lewis, J. A. Direct-Write Assembly of 3D Hydrogel Scaffolds for Guided Cell Growth. *Adv. Mater.* **2009**, *21* (23), 2407–2410.
(21) Shin, M.; Galarraga, J. H.; Kwon, M. Y.; Lee, H.; Burdick, J. A. Gallol-Derived ECM-Mimetic Adhesive Bioinks Exhibiting Temporal Shear-Thinning and Stabilization Behavior. *Acta Biomater.* **2019**, *95*, 165–175.
(22) Jeon, O.; Lee, Y. B.; Hinton, T. J.; Feinberg, A. W.; Alsberg, E. Cryopreserved Cell-Laden Alginate Microgel Bioink for 3D Bioprinting of Living Tissues. *Mater. Today Chem.* **2019**, *12*, 61–70.
(23) Motealleh, A.; Çelebi-Saltik, B.; Ermis, N.; Nowak, S.; Khademhosseini, A.; Kehr, N. S. 3D Printing of Step-Gradient Nanocomposite Hydrogels for Controlled Cell Migration. *Biofabrication* **2019**, *11* (4), 045015(1-10).
(24) Pi, Q.; Maharjan, S.; Yan, X.; Liu, X.; Singh, B.; van Genderen, A. M.; Robledo-Padilla, F.; Parra-Saldivar, R.; Hu, N.; Jia, W.; et al. Digitally Tunable Microfluidic Bioprinting of Multilayered Cannular Tissues. *Adv. Mater.* **2018**, *30* (43), 1706913(1-10).
(25) Yin, J.; Zhao, D.; Liu, J. Trends on Physical Understanding of Bioink Printability. *Bio-Design Manuf.* **2019**, *2* (1), 50–54.
(26) Zhang, Z.; Jin, Y.; Yin, J.; Xu, C.; Xiong, R.; Christensen, K.; Ringeisen, B. R.; Chrisey, D. B.; Huang, Y. Evaluation of Bioink Printability for Bioprinting Applications. *Appl. Phys. Rev.* **2018**, *5* (4), 041304(1-21).
(27) Smith, P. T.; Basu, A.; Saha, A.; Nelson, A. Chemical Modification and Printability of Shear-Thinning Hydrogel Inks for Direct-Write 3D Printing. *Polym. (United Kingdom)* **2018**, *152*, 42–50.
(28) Paxton, N.; Smolan, W.; Böck, T.; Melchels, F.; Groll, J.; Jungst, T. Proposal to Assess Printability of Bioinks for Extrusion-Based Bioprinting and Evaluation of Rheological Properties Governing Bioprintability. *Biofabrication* **2017**, *9* (4), 044107.
(29) Dubbin, K.; Hori, Y.; Lewis, K. K.; Heilshorn, S. C. Dual-Stage Crosslinking of a Gel-Phase Bioink Improves Cell Viability and Homogeneity for 3D Bioprinting. *Adv. Healthc. Mater.* **2016**, *5* (19), 2488–2492.
(30) Dubbin, K.; Tabet, A.; Heilshorn, S. C. Quantitative Criteria to Benchmark New and

Existing Bio-Inks for Cell Compatibility. *Biofabrication* **2017**, *9* (4), 044102(1-11).
(31) Lopez Hernandez, H.; Grosskopf, A. K.; Stapleton, L. M.; Agmon, G.; Appel, E. A. Non-Newtonian Polymer–Nanoparticle Hydrogels Enhance Cell Viability during Injection. *Macromol. Biosci.* **2019**, *19* (1), 1800275(1-7).
(32) Skardal, A.; Devarasetty, M.; Kang, H. W.; Mead, I.; Bishop, C.; Shupe, T.; Lee, S. J.; Jackson, J.; Yoo, J.; Soker, S.; et al. A Hydrogel Bioink Toolkit for Mimicking Native Tissue Biochemical and Mechanical Properties in Bioprinted Tissue Constructs. *Acta Biomater.* **2015**, *25*, 24–34.
(33) Mazzocchi, A.; Devarasetty, M.; Huntwork, R.; Soker, S.; Skardal, A. Optimization of Collagen Type I-Hyaluronan Hybrid Bioink for 3D Bioprinted Liver Microenvironments. *Biofabrication* **2018**, *11* (1), 015003(1-11).
(34) Bertassoni, L. E.; Cardoso, J. C.; Manoharan, V.; Cristino, A. L.; Bhise, N. S.; Araujo, W. A.; Zorlutuna, P.; Vrana, N. E.; Ghaemmaghami, A. M.; Dokmeci, M. R.; et al. Direct-Write Bioprinting of Cell-Laden Methacrylated Gelatin Hydrogels. *Biofabrication* **2014**, *6* (2), 024105(1-11).
(35) Rencsok, M.; Stichler, S.; Böck, T.; Paxton, N.; Bertlein, S.; Levato, R.; Schill, V. Double Printing of Hyaluronic Acid / Poly (Glycidol) Hybrid Hydrogels with Poly (ε-Caprolactone) for MSC Chondrogenesis. *Biofabrication* **2017**, *9*, 044108.
(36) Noh, I.; Kim, N.; Tran, H. N.; Lee, J.; Lee, C. 3D Printable Hyaluronic Acid-Based Hydrogel for Its Potential Application as a Bioink in Tissue Engineering. *Biomater. Res.* **2019**, *23* (3), 1–9.
(37) Freeman, F. E.; Kelly, D. J. Tuning Alginate Bioink Stiffness and Composition for Controlled Growth Factor Delivery and to Spatially Direct MSC Fate within Bioprinted Tissues. *Sci. Rep.* **2017**, *7*, 17042(1-12).
(38) Nguyen, D.; Hägg, D. A.; Forsman, A.; Ekholm, J.; Nimkingratana, P.; Brantsing, C.; Kalogeropoulos, T.; Zaunz, S.; Concaro, S.; Brittberg, M.; et al. Cartilage Tissue Engineering by the 3D Bioprinting of IPS Cells in a Nanocellulose/Alginate Bioink. *Sci. Rep.* **2017**, *7*, 658(1-10).
(39) Wüst, S.; Godla, M. E.; Müller, R.; Hofmann, S. Tunable Hydrogel Composite with Two-Step Processing in Combination with Innovative Hardware Upgrade for Cell-Based Three-Dimensional Bioprinting. *Acta Biomater.* **2014**, *10* (2), 630–640.
(40) Narayanan, L. K.; Huebner, P.; Fisher, M. B.; Spang, J. T.; Starly, B.; Shirwaiker, R. A. 3D-Bioprinting of Polylactic Acid (PLA) Nanofiber–Alginate Hydrogel Bioink Containing Human Adipose-Derived Stem Cells. *ACS Biomater. Sci. Eng.* **2016**, *2* (10), 1732–1742.
(41) Frost, B. A.; Sutliff, B. P.; Thayer, P.; Bortner, M. J.; Foster, E. J. Gradient Poly(Ethylene Glycol) Diacrylate and Cellulose Nanocrystals Tissue Engineering Composite Scaffolds via Extrusion Bioprinting. *Front. Bioeng. Biotechnol.* **2019**, *7*, 280(1-14).
(42) Xin, S.; Chimene, D.; Garza, J. E.; Gaharwar, A. K.; Alge, D. L. Clickable PEG Hydrogel Microspheres as Building Blocks for 3D Bioprinting. *Biomater. Sci.* **2019**, *7* (3), 1179–1187.
(43) Müller, M.; Becher, J.; Schnabelrauch, M.; Zenobi-Wong, M. Nanostructured Pluronic Hydrogels as Bioinks for 3D Bioprinting. *Biofabrication* **2015**, *7* (3), 035006(1-17).
(44) Saha, A.; Johnston, T. G.; Shafranek, R. T.; Goodman, C. J.; Zalatan, J. G.; Storti, D. W.; Ganter, M. A.; Nelson, A. Additive Manufacturing of Catalytically Active Living Materials. *ACS Appl. Mater. Interfaces* **2018**, *10* (16), 13373–13380.

(45) Millik, S. C.; Dostie, A. M.; Karis, D. G.; Smith, P. T.; McKenna, M.; Chan, N.; Curtis, C. D.; Nance, E.; Theberge, A. B.; Nelson, A. 3D Printed Coaxial Nozzles for the Extrusion of Hydrogel Tubes toward Modeling Vascular Endothelium. *Biofabrication* **2019**, *11* (4), 045009(1-11).

(46) Yu, C.; Ma, X.; Zhu, W.; Wang, P.; Miller, K. L.; Stupin, J.; Koroleva-Maharajh, A.; Hairabedian, A.; Chen, S. Scanningless and Continuous 3D Bioprinting of Human Tissues with Decellularized Extracellular Matrix. *Biomaterials* **2019**, *194*, 1–13.

(47) Lee, H.; Han, W.; Kim, H.; Ha, D.-H.; Jang, J.; Kim, B. S.; Cho, D.-W. Development of Liver Decellularized Extracellular Matrix Bioink for Three-Dimensional Cell Printing-Based Liver Tissue Engineering. *Biomacromolecules* **2017**, *18* (4), 1229–1237.

(48) Pati, F.; Jang, J.; Ha, D. H.; Won Kim, S.; Rhie, J. W.; Shim, J. H.; Kim, D. H.; Cho, D. W. Printing Three-Dimensional Tissue Analogues with Decellularized Extracellular Matrix Bioink. *Nat. Commun.* **2014**, *5*, 3935 (1-11).

(49) Ahn, G.; Min, K.-H.; Kim, C.; Lee, J.-S.; Kang, D.; Won, J.-Y.; Cho, D.-W.; Kim, J.-Y.; Jin, S.; Yun, W.-S.; et al. Precise Stacking of Decellularized Extracellular Matrix Based 3D Cell-Laden Constructs by a 3D Cell Printing System Equipped with Heating Modules. *Sci. Rep.* **2017**, *7*, 8624(1-11).

(50) Ali, M.; PR, A. K.; Yoo, J. J.; Zahran, F.; Atala, A.; Lee, S. J. A Photo-Crosslinkable Kidney ECM-Derived Bioink Accelerates Renal Tissue Formation. *Adv. Healthc. Mater.* **2019**, *8* (7), 1800992(1-10).

(51) Kang, H.; Peng, J.; Lu, S.; Liu, S.; Zhang, L.; Huang, J.; Sui, X.; Zhao, B.; Wang, A.; Xu, W.; et al. In Vivo Cartilage Repair Using Adipose-Derived Stem Cell-Loaded Decellularized Cartilage ECM Scaffolds. *J. Tissue Eng. Regen. Med.* **2014**, *8* (6), 442–453.

(52) Jang, J.; Kim, T. G.; Kim, B. S.; Kim, S. W.; Kwon, S. M.; Cho, D. W. Tailoring Mechanical Properties of Decellularized Extracellular Matrix Bioink by Vitamin B2-Induced Photo-Crosslinking. *Acta Biomater.* **2016**, *33*, 88–95.

(53) Toprakhisar, B.; Nadernezhad, A.; Bakirci, E.; Khani, N.; Skvortsov, G. A.; Koc, B. Development of Bioink from Decellularized Tendon Extracellular Matrix for 3D Bioprinting. *Macromol. Biosci.* **2018**, *18* (10), 1800024.

(54) Thum, T.; Gross, C.; Fiedler, J.; Fischer, T.; Kissler, S.; Bussen, M.; Galuppo, P.; Just, S.; Rottbauer, W.; Frantz, S.; et al. MicroRNA-21 Contributes to Myocardial Disease by Stimulating MAP Kinase Signalling in Fibroblasts. *Nature* **2008**, *456* (7224), 980–984.

(55) Dixon, I. M. C.; Cunnington, R. H.; Rattan, S. G.; Wigle, J. T. Cardiac Fibrosis and Heart Failure---Cause or Effect? In *Cardiac Fibrosis and Heart Failure: Cause or Effect?*; Dixon, I. M. C., Wigle, J. T., Eds.; Springer International Publishing, Switzerland: Cham, 2015; pp 1–4.

(56) Hinderer, S.; Schenke-Layland, K. Cardiac Fibrosis – A Short Review of Causes and Therapeutic Strategies. *Adv. Drug Deliv. Rev.* **2019**, *146*, 77–82.

(57) Kim, P.; Chu, N.; Davis, J.; Kim, D. H. Mechanoregulation of Myofibroblast Fate and Cardiac Fibrosis. *Adv. Biosyst.* **2018**, *2*, 1700172(1-11).

(58) Yong, K. W.; Li, Y.; Liu, F.; Bin Gao; Lu, T. J.; Wan Abas, W. A. B.; Wan Safwani, W. K. Z.; Pingguan-Murphy, B.; Ma, Y.; Xu, F.; et al. Paracrine Effects of Adipose-Derived Stem Cells on Matrix Stiffness-Induced Cardiac Myofibroblast Differentiation via Angiotensin II Type 1 Receptor and Smad7. *Sci. Rep.* **2016**, *6*, 33067(1-13).

(59) van Den Borne, S. W. M.; Diez, J.; Blankesteijn, W. M.; Verjans, J.; Hofstra, L.; Narula,

J. Myocardial Remodeling after Infarction: The Role of Myofibroblasts. *Nat. Rev. Cardiol.* **2010**, *7*, 30–37.

(60) Stempien-Otero, A.; Kim, D.-H.; Davis, J. Molecular Networks Underlying Myofibroblast Fate and Fibrosis. *J. Mol. Cell. Cardiol.* **2016**, *97*, 153–161.

(61) Meyer-ter-Vehn, T.; Han, H.; Grehn, F.; Schlunck, G. Extracellular Matrix Elasticity Modulates TGF-β-Induced P38 Activation and Myofibroblast Transdifferentiation in Human Tenon Fibroblasts. *Investig. Ophthalmol. Vis. Sci.* **2011**, *52* (12), 9149–9155.

(62) Huang, X.; Yang, N.; Fiore, V. F.; Barker, T. H.; Sun, Y.; Morris, S. W.; Ding, Q.; Thannickal, V. J.; Zhou, Y. Matrix Stiffness–Induced Myofibroblast Differentiation Is Mediated by Intrinsic Mechanotransduction. *Am. J. Respir. Cell Mol. Biol.* **2012**, *47* (3), 340–348.

(63) Godbout, C.; Castella, L. F.; Smith, E. A.; Talele, N.; Chow, M. L.; Garonna, A.; Hinz, B. The Mechanical Environment Modulates Intracellular Calcium Oscillation Activities of Myofibroblasts. *PLoS One* **2013**, *8* (5), e64560(1-10).

(64) Dávila, J. L.; d'Ávila, M. A. Laponite as a Rheology Modifier of Alginate Solutions: Physical Gelation and Aging Evolution. *Carbohydr. Polym.* **2017**, *157*, 1–8.

(65) Faes, M.; Valkenaers, H.; Vogeler, F.; Vleugels, J.; Ferraris, E. Extrusion-Based 3D Printing of Ceramic Components. *Procedia CIRP* **2015**, *28*, 76–81.

(66) Jin, Y.; Zhao, D.; Huang, Y. Study of Extrudability and Standoff Distance Effect during Nanoclay-Enabled Direct Printing. *Bio-Design Manuf.* **2018**, *1*, 123–134.

(67) Hong, S.; Sycks, D.; Chan, H. F.; Lin, S.; Lopez, G. P.; Guilak, F.; Leong, K. W.; Zhao, X. 3D Printing of Highly Stretchable and Tough Hydrogels into Complex, Cellularized Structures. *Adv. Mater.* **2015**, *27* (27), 4035–4040.

(68) Jin, Y.; Liu, C.; Chai, W.; Compaan, A.; Huang, Y. Self-Supporting Nanoclay as Internal Scaffold Material for Direct Printing of Soft Hydrogel Composite Structures in Air. *ACS Appl. Mater. Interfaces* **2017**, *9* (20), 17456–17465.

(69) Gungor-Ozkerim, P. S.; Inci, I.; Zhang, Y. S.; Khademhosseini, A.; Dokmeci, M. R. Bioinks for 3D Bioprinting: An Overview. *Biomater. Sci.* **2018**, *6* (5), 915–946.

(70) Rathan, S.; Dejob, L.; Schipani, R.; Haffner, B.; Möbius, M. E.; Kelly, D. J. Fiber Reinforced Cartilage ECM Functionalized Bioinks for Functional Cartilage Tissue Engineering. *Adv. Healthc. Mater.* **2019**, *8*, 1801501(1-11).

(71) Gao, G.; Lee, J. H.; Jang, J.; Lee, D. H.; Kong, J.-S.; Kim, B. S.; Choi, Y.-J.; Jang, W. B.; Hong, Y. J.; Kwon, S.-M.; et al. Tissue Engineered Bio-Blood-Vessels Constructed Using a Tissue-Specific Bioink and 3D Coaxial Cell Printing Technique: A Novel Therapy for Ischemic Disease. *Adv. Funct. Mater.* **2017**, *27*, 1700798 (1-12).

(72) Ahlfeld, T.; Cidonio, G.; Kilian, D.; Duin, S.; Akkineni, A. R.; Dawson, J. I.; Yang, S.; Lode, A.; Oreffo, R. O. C.; Gelinsky, M. Development of a Clay Based Bioink for 3D Cell Printing for Skeletal Application. *Biofabrication* **2017**, *9* (3), 034103(1-16).

(73) Kim, W. J.; Kim, G. H. An Intestinal Model with a Finger-like Villus Structure Fabricated Using a Bioprinting Process and Collagen/SIS-Based Cell-Laden Bioink. *Theranostics* **2020**, *10* (6), 2495–2508.

(74) Lee, H.; Yang, G. H.; Kim, M.; Lee, J.; Huh, J.; Kim, G. Fabrication of Micro/Nanoporous Collagen/DECM/Silk-Fibroin Biocomposite Scaffolds Using a Low Temperature 3D Printing Process for Bone Tissue Regeneration. *Mater. Sci. Eng. C* **2018**, *84* (April 2017), 140–147.

(75) Guan, X.; Mack, D. L.; Moreno, C. M.; Strande, J. L.; Mathieu, J.; Shi, Y.; Markert, C.

D.; Wang, Z.; Liu, G.; Lawlor, M. W.; et al. Dystrophin-Deficient Cardiomyocytes Derived from Human Urine: New Biologic Reagents for Drug Discovery. *Stem Cell Res.* **2014**, *12* (2), 467–480.

(76) Lian, X.; Zhang, J.; Azarin, S. M.; Zhu, K.; Hazeltine, L. B.; Bao, X.; Hsiao, C.; Kamp, T. J.; Palecek, S. P. Directed Cardiomyocyte Differentiation from Human Pluripotent Stem Cells by Modulating Wnt/β-Catenin Signaling under Fully Defined Conditions. *Nat. Protoc.* **2013**, *8* (1), 162–175.

(77) Bielawski, K. S.; Leonard, A.; Bhandari, S.; Murry, C. E.; Sniadecki, N. J. Real-Time Force and Frequency Analysis of Engineered Human Heart Tissue Derived from Induced Pluripotent Stem Cells Using Magnetic Sensing. *Tissue Eng. - Part C Methods* **2016**, *22* (10), 932–940.

(78) Tsui, J. H.; Leonard, A.; Camp, N. D.; Long, J. T.; Nawas, Z. Y.; Chavanachat, R.; Choi, J. S.; Wolf-Yadlin, A.; Murry, C. E.; Sniadecki, N. J.; et al. Functional Maturation of Human IPSC-Based Cardiac Microphysiological Systems with Tunable Electroconductive Decellularized Extracellular Matrices. *bioRxiv* **2019**, 786657.

(79) Choudhury, D.; Tun, H. W.; Wang, T.; Naing, M. W. Organ-Derived Decellularized Extracellular Matrix: A Game Changer for Bioink Manufacturing? *Trends Biotechnol.* **2018**, *36* (8), 787–805.

(80) Hodgson, M. J.; Knutson, C. C.; Momtahan, N.; Cook, A. D. Extracellular Matrix from Whole Porcine Heart Decellularization for Cardiac Tissue Engineering. In *Methods in Molecular Biology*; Turksen, K., Ed.; Humana Press, New York, NY, 2017; pp 95–102.

(81) Sydney Gladman, A.; Matsumoto, E. A.; Nuzzo, R. G.; Mahadevan, L.; Lewis, J. A. Biomimetic 4D Printing. *Nat. Mater.* **2016**, *15* (4), 413–418.

(82) Ribeiro, A.; Blokzijl, M. M.; Levato, R.; Visser, C. W.; Castilho, M.; Hennink, W. E.; Vermonden, T.; Malda, J. Assessing Bioink Shape Fidelity to Aid Material Development in 3D Bioprinting. *Biofabrication* **2018**, *10* (1), 014102(1-9).

(83) Mouser, V. H. M.; Melchels, F. P. W.; Visser, J.; Dhert, W. J. A.; Gawlitta, D.; Malda, J. Yield Stress Determines Bioprintability of Hydrogels Based on Gelatin-Methacryloyl and Gellan Gum for Cartilage Bioprinting. *Biofabrication* **2016**, *8* (3), 035003(1-13).

(84) Gao, T.; Gillispie, G. J.; Copus, J. S.; PR, A. K.; Seol, Y.-J.; Atala, A.; Yoo, J. J.; Lee, S. J. Optimization of Gelatin–Alginate Composite Bioink Printability Using Rheological Parameters: A Systematic Approach. *Biofabrication* **2018**, *10* (3), 034106(1-9).

(85) He, Y.; Yang, F.; Zhao, H.; Gao, Q.; Xia, B.; Fu, J. Research on the Printability of Hydrogels in 3D Bioprinting. *Sci. Rep.* **2016**, *6*, 29977(1-13).

(86) Mezger, T. G. *The Rheology Handbook, 4th Edition*; Vincentz Network, Hanover, Germany, 2014.

(87) Dijkstra, M.; Hansen, J. P.; Madden, P. A. Gelation of a Clay Colloid Suspension. *Phys. Rev. Lett.* **1995**, *75* (11), 2236–2239.

(88) Ruzicka, B.; Zaccarelli, E. A Fresh Look at the Laponite Phase Diagram. *Soft Matter* **2011**, *7* (4), 1268–1286.

(89) Shi, J.; Wang, C.; Ngai, T.; Lin, W. Diffusion and Binding of Laponite Clay Nanoparticles into Collagen Fibers for the Formation of Leather Matrix. *Langmuir* **2018**, *34* (25), 7379–7385.

(90) Pawar, N.; Bohidar, H. B. Surface Selective Binding of Nanoclay Particles to Polyampholyte Protein Chains. *J. Chem. Phys.* **2009**, *131* (4).

(91) Li, C.; Mu, C.; Lin, W.; Ngai, T. Gelatin Effects on the Physicochemical and

Hemocompatible Properties of Gelatin/PAAm/Laponite Nanocomposite Hydrogels. *ACS Appl. Mater. Interfaces* **2015**, *7* (33), 18732–18741.

(92) Wu, J.; Zhao, C.; Lin, W.; Hu, R.; Wang, Q.; Chen, H.; Li, L.; Chen, S.; Zheng, J. Binding Characteristics between Polyethylene Glycol (PEG) and Proteins in Aqueous Solution. *J. Mater. Chem. B* **2014**, *2* (20), 2983–2992.

(93) Hinton, T. J.; Jallerat, Q.; Palchesko, R. N.; Park, J. H.; Grodzicki, M. S.; Shue, H.-J.; Ramadan, M. H.; Hudson, A. R.; Feinberg, A. W. Three-Dimensional Printing of Complex Biological Structures by Freeform Reversible Embedding of Suspended Hydrogels. *Sci. Adv.* **2015**, *1* (9), e1500758(1-10).

(94) Beamish, J. A.; Zhu, J.; Kottke-Marchant, K.; Marchant, R. E. The Effects of Monoacrylated Poly(Ethylene Glycol) on the Properties of Poly(Ethylene Glycol) Diacrylate Hydrogels Used for Tissue Engineering. *J. Biomed. Mater. Res. Part A* **2010**, *92A* (2), 441–450.

(95) Buxton, A. N.; Zhu, J.; Marchant, R.; West, J. L.; Yoo, J. U.; Johnstone, B. Design and Characterization of Poly(Ethylene Glycol) Photopolymerizable Semi-Interpenetrating Networks for Chondrogenesis of Human Mesenchymal Stem Cells. *Tissue Eng.* **2007**, *13* (10), 2549–2560.

(96) Fairbanks, B. D.; Schwartz, M. P.; Bowman, C. N.; Anseth, K. S. Photoinitiated Polymerization of PEG-Diacrylate with Lithium Phenyl-2,4,6-Trimethylbenzoylphosphinate: Polymerization Rate and Cytocompatibility. *Biomaterials* **2009**, *30* (35), 6702–6707.

(97) Jimenez-Vergara, A. C.; Lewis, J.; Hahn, M. S.; Munoz-Pinto, D. J. An Improved Correlation to Predict Molecular Weight between Crosslinks Based on Equilibrium Degree of Swelling of Hydrogel Networks. *J. Biomed. Mater. Res. - Part B Appl. Biomater.* **2018**, *106* (3), 1339–1348.

(98) Nguyen, Q. T.; Hwang, Y.; Chen, A. C.; Varghese, S.; Sah, R. L. Cartilage-like Mechanical Properties of Poly (Ethylene Glycol)-Diacrylate Hydrogels. *Biomaterials* **2012**, *33* (28), 6682–6690.

(99) Bryant, S. J.; Anseth, K. S.; Lee, D. A.; Bader, D. L. Crosslinking Density Influences the Morphology of Chondrocytes Photoencapsulated in PEG Hydrogels during the Application of Compressive Strain. *J. Orthop. Res.* **2004**, *22* (5), 1143–1149.

(100) Lee, S.; Tong, X.; Yang, F. The Effects of Varying Poly(Ethylene Glycol) Hydrogel Crosslinking Density and the Crosslinking Mechanism on Protein Accumulation in Three-Dimensional Hydrogels. *Acta Biomater.* **2014**, *10* (10), 4167–4174.

(101) Mazzoccoli, J. P.; Feke, D. L.; Baskaran, H.; Pintauro, P. N. Mechanical and Cell Viability Properties of Crosslinked Low- And High-Molecular Weight Poly(Ethylene Glycol) Diacrylate Blends. *J. Biomed. Mater. Res. - Part A* **2010**, *93A* (2), 558–566.

(102) Herum, K. M.; Lunde, I. G.; McCulloch, A. D.; Christensen, G. The Soft- and Hard-Heartedness of Cardiac Fibroblasts: Mechanotransduction Signaling Pathways in Fibrosis of the Heart. *J. Clin. Med.* **2017**, *6* (5), 53.

(103) Kim, W.; Cho, Y. S.; Wang, X.; Park, O.; Ma, X.; Kim, H.; Gan, W.; Jho, E.; Cha, B.; Jeung, Y.; et al. Hippo Signaling Is Intrinsically Regulated during Cell Cycle Progression by APC/CCdh1. *Proc. Natl. Acad. Sci.* **2019**, *116* (19), 9423–9432.

(104) Peak, C. W.; Stein, J.; Gold, K. A.; Gaharwar, A. K. Nanoengineered Colloidal Inks for 3D Bioprinting. *Langmuir* **2018**, *34* (3), 917–925.

(105) Zhang, Y.; Fan, W.; Wang, K.; Wei, H.; Zhang, R.; Wu, Y. Novel Preparation of Au

Nanoparticles Loaded Laponite Nanoparticles/ECM Injectable Hydrogel on Cardiac Differentiation of Resident Cardiac Stem Cells to Cardiomyocytes. *J. Photochem. Photobiol. B Biol.* **2019**, *192* (1), 49–54.